A TUNABLE CARBON NANOTUBE RESONATOR

A Dissertation

Presented to the Faculty of the Graduate School

of Cornell University

in Partial Fulfillment of the Requirements for the Degree of

Doctor of Philosophy

by

Vera A. Sazonova

August 2006

A TUNABLE CARBON NANOTUBE RESONATOR

Vera A. Sazonova, Ph.D.

Cornell University 2006

Nanoelectromechanical systems (NEMS) have recently been the subject of much exciting research. They have been proposed for use in various applications such as mass and force detection, RF processing, and investigating quantum effects in the mechanical motion of resonators. Attempts to increase sensitivity for these applications has led to further and further miniaturization of the mechanical devices. When their size reaches the range of hundreds of nanometers, these devices have active masses in the hundreds of the femtograms and operational frequencies in the GHz. An ultimate limit to this miniaturization is a mechanical resonator based on a single molecule. Such a resonator should not only be able to push the limits of the measurements sensitivities, but can also probe decrease of the quality factor values with size that has so far been attributed to the increase of the surface-to-volume ratios in these resonators. Carbon nanotubes (CNTs), thin tubes of graphene, are light, stiff, strong, and electrically active, which makes them a perfect candidate for a such a NEMS structure.

By employing a capacitive actuation and detection technique, we investigate the performance of a resonator based on a doubly-clamped, suspended CNT in a transistor geometry. We excite vibrations by applying an AC driving voltage to the gate electrode, and we detect them by measuring the current through the CNT device. Controlling the CNT's tension, by applying a downward DC force with

a DC voltage on the gate electrodes, enables us to tune the resonant frequency, resulting in the first tunable and self-detecting carbon nanotube resonator.

This setup also allows us to probe the loss mechanisms in these small structures. We systematically study correlation of the quality factor with each of the device characteristics, including electrical resistance, fabrication geometry, and resonant mode harmonic number. We also study dependence of the quality factor on the experimental knobs, such as pressure, temperature, DC gate voltage, and AC driving voltage. We find that the quality factors in CNTs continue the trend previously established by NEMS, and that several dissipation mechanisms must be responsible for losses in this system. We identify coupling to the environment, the thermoelastic effect, and surface-related losses as the three key mechanisms.

BIOGRAPHICAL SKETCH

Vera Sazonova was born 1979 in Moscow, Russia. In 1996, after graduating from a math specialized high school in Moscow, she moved to Oxford, Mississippi, to attend the University of Mississippi, also known as Olemiss. There she worked towards here B.S. degrees in physics and computer science, moving from debugging compilers for hand-held devices to flying weather balloons into thunderstorm clouds. She graduated with honors from the University of Mississippi in 2000 and joined graduate school at Cornell University. In January 2001 she joined the group of Paul McEuen, where she worked on her Ph.D. research, while learning to tango and play soccer. Continuing her move to the north, she will be pursuing a postdoc at McGill University in Québec, Canada.

ACKNOWLEDGEMENTS

Neither these past six years in Ithaca, nor me, nor this thesis would be the same without the help and company of many people.

First, my advisor, Paul McEuen, whose intuitive insights always turned out to be correct, despite my endless efforts to contradict. I have never met a more observant, intelligent, and knowledgable, yet diverse and open-minded person than Paul. Among many others, I have enjoyed your company in a social setting just as much as your scientific input in the lab. Thank you for teaching me, listening to me, and letting me argue with you. I couldn't ask for better guidance.

I was very fortunate to get help from a lot of people on this project. Special thanks to Hande and David, who developed all of the theoretical work, to Yuval, with whom we started this project five years ago, and to Arend, who is taking the experiment to the next level and whose eternal happiness helped him survive through my ceaseless teasings. Thanks to Mick Thomas for letting me abuse his SEM, thanks to Mike Skvarla, for teaching me how to love the g-line stepper, and thanks to all of the CNF crew for helping me run big machines on tiny devices.

Several other people in the dark corridors of Clark Hall's basement are responsible for a great part of this work and for the preservation of my sanity. First, Lisa, Markus, Scott, and Patrycja, thank you for undertaking the challenge of proofreading this thesis and reading more than I could ever hope for. Special thanks to Alex and Slava for teaching me what the word is all about and helping me rediscover my Russian side. Lisa, Patrycja and Ferdinand, thanks for introducing me to climbing and sharing the pain of learning conjugations in German. Markus, Jun, Sami and Ethan, thanks for being such good friends and being there for me, when I needed it. And to all basement inhabitants, particularly Ethan, Alex, Sami, Markus, Jun,

Patrycja, Lisa, Arend, Ferdinand, Slava, Alex, Kiril, Shahal, Ji-Young, Jiwoong, Ken, Luke, Nathan, Xinjian, Zhaohui, and Sam, thanks for sharing the ups and downs of research, the ups and downs of Ithaca's weather, and the ups and downs of life. I will miss you all.

For that last two years I had the pleasure to be a part of the science co-op and to live with some wonderful people: Markus, Ben, Faisal, Jahan, Damian, Larissa, Thua, Fatima, Kevin, Lalo, Jef, Karin, Ruby, Johan, Sylvie, Sarah, Stephanie, Sash, and Greg. Living with people from almost ten different countries has definitely expanded my world view. I have enjoyed so much cooking together, our crazy dinner conversations, watching "House" and "Colbert Report" together, painting away the rooms, and bickering about the disappearance of oranges. Thank you all for the smiles, the warmth, and making the house feel like a big family.

During my life at Cornell, dancing has become an important part of my life. Thanks to Cindy Overstreet, my first dance teacher, I got into swing, only to switch to argentine tango shortly after. The Ithaca Tangueros, our local tango-dancing group, has welcomed me, taught me, and advanced with me for the last two years. Many thanks to you all for the dances, beautiful music, and support. Particularly, I would like to thank my dancing partner, Joaquin, who has taught me everything I know about dancing, always compensated for my mistakes, and would not let me fall even in the craziest of lifts.

And finally, most importantly, I want to thank my family for always quietly watching out for me, patiently loving me, and sparing advice, when I needed it most. Mom, dad, and grandma, your energy, love of live, spontaneity, and cleverness are an inspiration. I wouldn't be who I am if it wasn't for you.

TABLE OF CONTENTS

LIST OF TABLES

LIST OF FIGURES

CHAPTER 1

INTRODUCTION

1.1 Introduction

Micro- and nanoelectromechanical devices have been the subject of extensive research for a number of years and have generated much excitement as their use in commercial applications has increased. An electromechanical device is basically a mechanical element (a beam, a cantilever, etc.) that is controlled by a microelectronic circuit. Microelectromechanical systems (MEMS) are currently used to make such diverse systems as electric current or light flow regulators (Ekinci and Roukes, 2005), microscale mirrors arrays (Craighead, 2000), accelerometers in crash airbags systems, RF electronic components, and sensors.

Nanoelectromechanical systems (NEMS) are the natural successor to MEMS as the size of the devices is scaled down to the submicron domain. They also hold promise for a number of scientific and technological applications. In particular, NEMS have been proposed for use in ultrasensitive mass detection (Sidles et al., 1995, Roukes, 2001), RF signal processing (Nguyen, 1999, Nguyen et al., 1999), and as a model system for exploring quantum phenomena in macroscopic systems (Cho, 2003, LaHaye et al., 2004). Improving sensitivity for these applications requires decreasing the size, or, more importantly, the active mass of the resonator, increasing its vibration frequency, and decreasing the line-width of the resonance. Perhaps the ultimate material for these applications is a carbon nanotube (CNT). CNTs are the stiffest material known, have low density and ultrasmall cross sections, and can be defect-free. In this thesis we will describe the fabrication and operation of the first NEMS device based on a carbon nanotube.

Due to their remarkable electrical, mechanical, and electro-mechanical properties, CNTs have been a subject of intensive research since their discovery in 1991 (Ijima, 1991). In this chapter we give a brief introduction to CNTs' structure (section 1.2) and their electrical (section 1.3) and mechanical (section 1.4) properties. We conclude the chapter with a section on the previous work done using CNTs as mechanical resonators (section 1.5).

1.2 Carbon nanotube structure

Carbon nanotubes are thin, hollow cylinders of covalently bonded carbon atoms. They can come in two different flavors: single-walled carbon nanotubes (SWNTs) and multiwalled carbon nanotubes (MWNTs), which consist of concentric SWNTs (or shells) stacked together. SWNTs are typically $1-2$nm in diameter and several μm in length, but SWNTs up to mm long have been grown (Huang et al., 2003a). MWNTs typically have diameters in the range of $5-50$nm and are typically several tens of μm in length. CNTs are created by either catalytical (Kong et al., 1998), arc-discharge (Ijima, 1991) or laser-ablation (Guo et al., 1995) methods. The work in this thesis was done on only individual single- or few-walled CNTs created by catalytic methods.

The carbon atoms in the walls of a nanotube (NT) are arranged in a honeycomb lattice just as in a single sheet of graphene. In fact, a CNT can be thought of as a single rolled graphene sheet (See Fig. 1.1a). The properties of a CNT then derive from the properties of graphene. Depending on the "rolling" angle with respect to the lattice, the relative arrangement of the atoms in the walls of the CNT with respect to the CNT axis is different. The angle between the orientation of the lattice and the NT's axis is known as the "chirality" of the CNT. Fig.

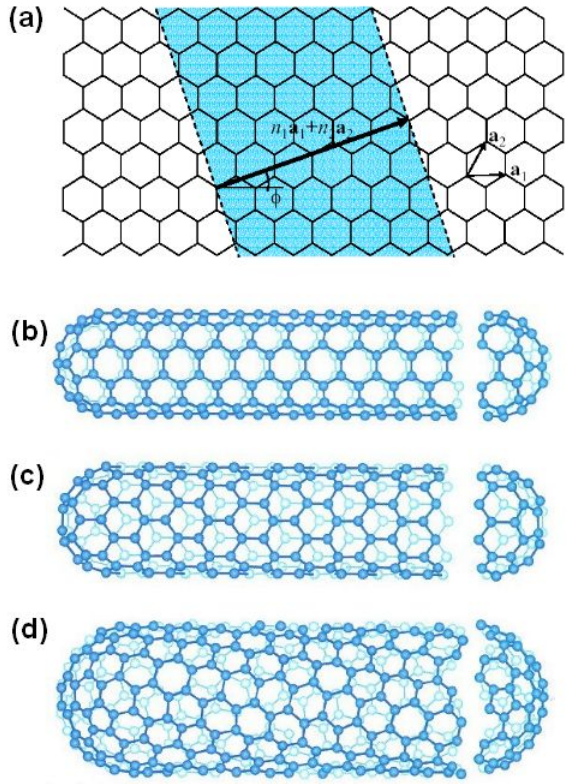

Figure 1.1: Structure of CNTs. Adopted from Minot (2004). **(a)** Forming a CNT by wrapping a graphene sheet. The shaded area shows the part of the sheet to be wrapped and the black arrow identifies the direction of wrapping. The angle ϕ between the direction of wrapping and the lattice is called the "chiral" angle. **(b)** An "armchair" CNT ($\phi = 30°$). **(c)** A "zigzag" CNT ($\phi = 0°$). **(d)** A "chiral" CNT (ϕ is arbitrary).

1.1b,c,d show examples of CNTs with different chiralities.

1.3 Electrical properties of carbon nanotubes

Carbon nanotubes inherit their remarkable electrical properties from the unique electronic band structure of graphene (Fig. 1.2a). Depending on its chirality, the nanotube can be either a metal, a semiconductor (Tans et al., 1998), or a small-band gap semiconductor (Zhou et al., 2000).

The cylindrical structure of a CNT imposes periodic boundary conditions on the electron wave function around the NT's waist, and transport in a SWNT occurs only along the axis of the tube, making a CNT a 1D conductor. The conductance G of a 1D channel is given by the Landauer-Buttiker model (for review see Datta (1995)),

$$G = \left(\frac{e^2}{h}\right) \sum_i T_i \tag{1.1}$$

where T_i denotes the transmission probability through the i-th channel, and e^2/h is the so-called quantum of conductance. In nanotubes there are four degenerate 1D channels: two due to spin degeneracy, and two due to the degeneracy arising from clockwise/counter-clockwise "handedness" of the electron wave function (see Fig. 1.2d). Thus, the theoretical low-bias conductance of a CNT with perfect transmission is

$$G = 4\left(\frac{e^2}{h}\right) \tag{1.2}$$

Conductances approaching this value have been measured experimentally in high-quality metallic tubes with lengths of 200nm (Kong et al., 2001, Liang et al., 2001) and in semiconducting tubes in the "on" state (Javey et al., 2003, Yaish et al., 2004). For such tubes, the conductance through the tube is essentially ballistic. For longer tubes, the main origin of resistivity at low biases is believed to

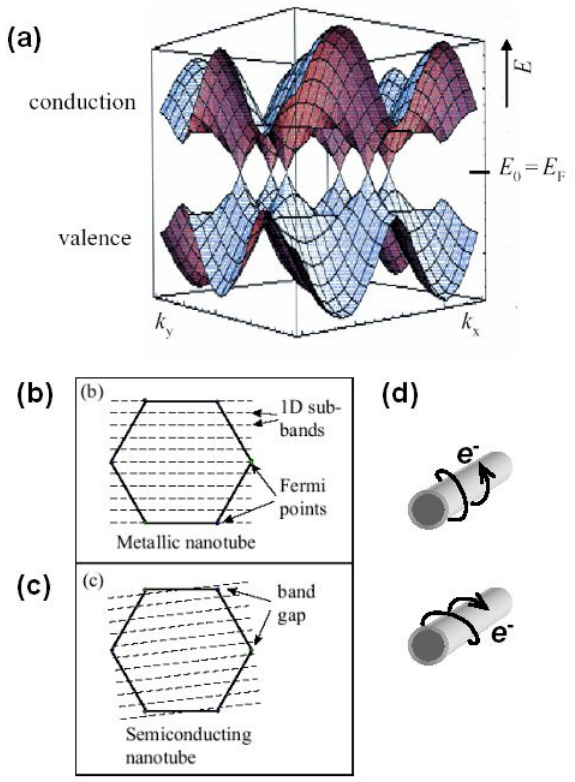

Figure 1.2: Electronic structure of CNTs. Adopted from Minot (2004). **(a)** The band structure of graphene. **(b), (c)** Imposing the boundary conditions of the band structure leads to allowed states on the equidistant lines in k-space. For a metallic CNT **(b)** the lines cross the points of zero band gap (the Fermi points). For a semiconducting CNT **(c)** the lines miss the Fermi points. **(d)** 4-fold degeneracy of a NT: two states due to spin and two states due to the "handedness" of the wavefunction.

be due to scattering by acoustic phonons (Kane et al., 1998) with experimentally measured mean free paths at room temperature of around a μm.

Semiconducting tubes have a band gap $E_g = 0.7\text{eV/D[nm]}$, where D is the CNT diameter (Dresselhaus et al., 2001), separating the valence and conduction bands. Small-band semiconducting tubes have gaps on the order $\leq 100\text{meV}$ that originate due to perturbations such as twist, curvature, or local strain in an otherwise metallic tube (Heyd et al., 1997, Yang et al., 1999, Zhou et al., 2000).

An electrostatic field can couple to the potential of the tube and shift its Fermi energy from the valence band, into the gap, and further into the conduction band, modifying the CNT conductance (Tans et al., 1998). This field-effect transistor (FET) behavior is useful for circuit-type applications and for sensors. An example of a CNT in the transistor geometry is illustrated in Fig. 1.3a. There are three different regimes of operation. For gate voltages less than 0V the Fermi energy is in the valence band and the transport is due to the holes ("p-regime"). When there are $0-5\text{V}$ on the gate, the Fermi energy is in the band gap and the transport through the nanotube is "off". For gate voltages larger than 4V the Fermi energy is in the conduction band and the transport is due to electrons ("n-regime"). The metal contacts screen the effect of the gate for the contacted part of the nanotube. As a result the ends of the CNT are "pinned" at a certain doping defined by the difference between the work functions of the CNT and the contacting metal(Javey et al., 2003). The gate voltage then modifies the Fermi energy for the middle section of the tube. The underlying oxide and various adsorbates can also affect the doping of a CNT. Due to these effects, at zero gate voltage the nanotube is in the "p-regime" for a typical device.

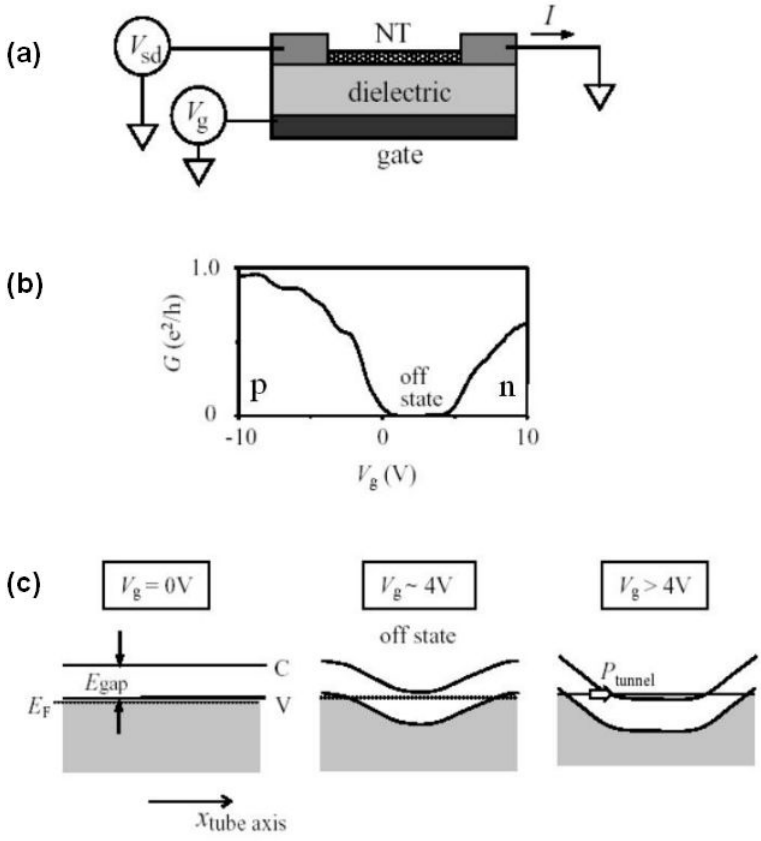

Figure 1.3: Carbon Nanotube FET. Adopted from Minot (2004). **(a)** A schematic of a CNT FET. **(b)** Conductance through the transistor as a function of the gate voltage. For negative voltages the CNT is in the "p" regime, for gate voltages between 0 and 5V the CNT is in the "off" state, and for larger gate voltages the CNT is in the "n" regime. **(c)** Band diagram of "p", "off", and "n" regimes of operation.

1.4 Mechanical properties of carbon nanotubes

CNTs owe their mechanical properties to the strength of the sp^2 hybridized C-C bond. The two most important parameters characterizing the mechanical properties of a material are the elastic modulus E

$$\sigma = \epsilon E \tag{1.3}$$

that describes the slope of the stress (σ) vs. strain (ϵ) curve, and the tensile strength (σ_s) which describes the maximum stress that the material can endure. If further stress is applied the material either fractures or undergoes irreversible plastic deformation.

Theoretical calculations for the elastic modulus and the tensile strength of a CNT predicted values ranging from 0.5TPa to 5TPa for the elastic modulus (Overney et al., 1993, Yakobson et al., 1996, Lu, 1997, Yao and Lordi, 1999, Hernandez et al., 1999, Zhou et al., 2000) and 10GPa to 40GPa for the tensile strength (Yakobson, 1997).

Experimentally, neither parameter is easy to measure due to the small size of CNTs. Two techniques, however, have proved useful in measuring these properties: Atomic Force Microscopy (AFM) and Electron Microscopy. Early work concentrated mostly on the properties of MWNT and CNT bundles. Treacy et al. (1996) used Transmission Electron Microscopy (TEM) to image thermal vibrations of MWNTs at high temperature and then extracted the elastic modulus by fitting the shape of the resonance (Fig. 1.4a). They found values ranging from 0.4 to 4.15TPa. This work was later continued by several other groups using TEM with MWNTs (Krishnan et al., 1998), with reported values around 1.4TPa, and Scanning Electron Microscopy (SEM) with individual SWNTs at room temperature

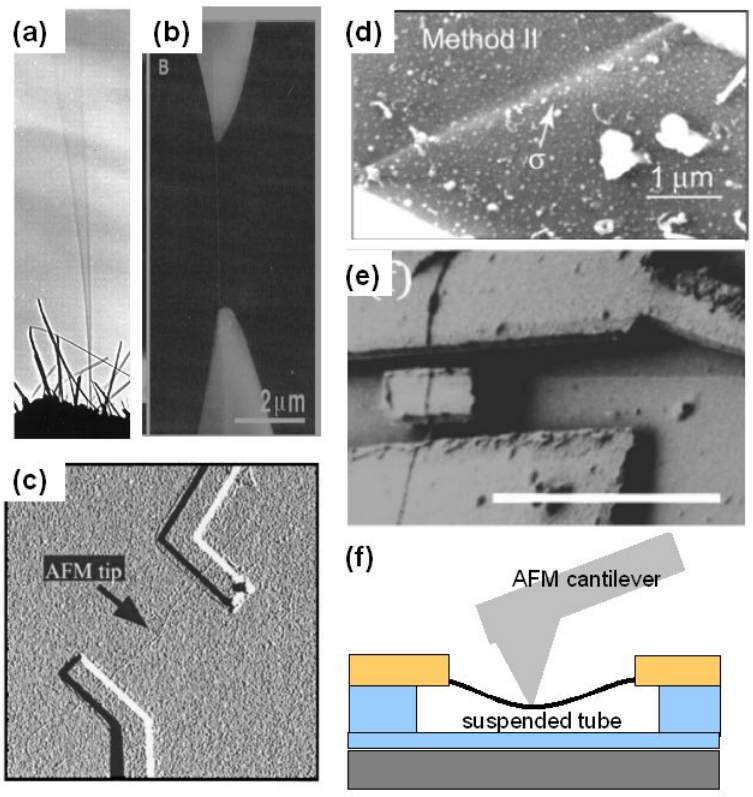

Figure 1.4: Measuring mechanical properties of CNTs. **(a)** Thermal vibrations of MWNT in a TEM (Treacy et al., 1996). **(b)** A CNT pulled by two AFM tips inside an SEM (Yu et al., 2000). **(c)** A contacted CNT stretched laterally by an AFM tip (Kim et al., 2002). **(d)** Thermal vibrations of a SWNT in an SEM (Babic et al., 2003). **(e)** A metallic paddle defined on top of a CNT to measure its shear modulus (Williams et al., 2003). **(f)** A schematic of a suspended CNT stretched by an AFM tip (Minot et al., 2003).

(Babic et al., 2003)(Fig. 1.4d), with reported range of values of 18GPa to 2.5TPa. Electrically excited CNT vibrations have also been used to measure elastic modulus (Poncharal et al., 1999, Gao et al., 2000), with extracted elastic modulus values of approximately 1TPa. This work will be discussed in detail in the next section.

Wong et al. (1997) used an AFM cantilever to bend singly clamped MWNTs and directly measure their elasticity and strength. They found values of elastic modulus of around 1.3TPa. Salvetat et al. (1999) and later Walters et al. (1999), Kim et al. (2002), and Minot et al. (2003) have used similar methods to study the elastic properties of doubly clamped ropes of SWNT and individual doubly clamped SWNTs (see Fig.1.4c,f). Salvetat et al. (1999) reported values for the elastic modulus around 1TPa for arc-discharge grown tubes, and values an order of magnitude or more lower for tubes grown by catalytic methods. Later measurements produced similar results for the elastic modulus of around 1TPa and in some cases also determined an upper bound on the tensile strength (Walters et al., 1999) of around 40GPa. Yu et al. (2000) studied the elastic properties of SWNT ropes by attaching them to two AFM cantilevers inside of an SEM system (Fig 1.4b). The measurements yielded elastic modulus values around 1TPa and tensile strength of $\sim$ 40GPa.

Williams et al. (2003) have measured the shear modulus of MWNTs by fabricating a metallic paddle on top of the nanotube to which a twisting force could be applied using an AFM cantilever (see Fig. 1.4e). The measured values of 400GPa were in rough agreement with theory.

As the electronic properties of CNTs are highly sensitive to the geometric configuration of the atoms, it is also possible to study the effect of mechanical modifications on the electronic properties of the CNT. Theoretically it has been predicted

(Heyd et al., 1997, Yang et al., 1999, 2000) that it is possible to modify the band gap of a semiconducting CNT and induce a band gap in certain metallic tubes by applying strain to NTs. Indeed, it has been experimentally shown that the band gap E_{g} of a semiconducting nanotube can be tuned by applying a small mechanical strain σ (Minot et al., 2003) as

$$\frac{dE_{\mathrm{g}}}{d\sigma} \approx \pm 100 \frac{\mathrm{meV}}{\%} \cos 3\phi \tag{1.4}$$

where ϕ is the chiral angle and the sign up front depends on the exact wrapping vectors.

1.5 Previous work on CNT resonators

Early work on CNT resonators was done on MWNTs in an electron microscopy system for the purpose of measuring the elastic modulus of CNTs. Poncharal et al. (1999), soon followed by Gao et al. (2000), have grown MWNTs on a holder by either pyrolysis (typically 6μm long and 10nm in diameter) (Poncharal et al., 1999) or arc-discharge (Gao et al., 2000) (typically $30-60\mu$m long and $13-20$nm in diameter), and placed them in an oscillating electric field created by applying an AC voltage to a nearby electrode (Fig. 1.5a). A DC voltage difference was also applied to induce charge on the CNT. In an AC electric field, a charged nanotube experiences an oscillating electric force which sets it into motion when the frequency of the AC field matches the resonance frequency of the nanotube. Detection is implemented using a transmission electron microscope (TEM) (Poncharal et al., 1999) or a scanning electron microscope (SEM) (Gao et al., 2000) and directly imaging the nanotube's movement (Figs.1.5b,c). For a singly-clamped cantilever

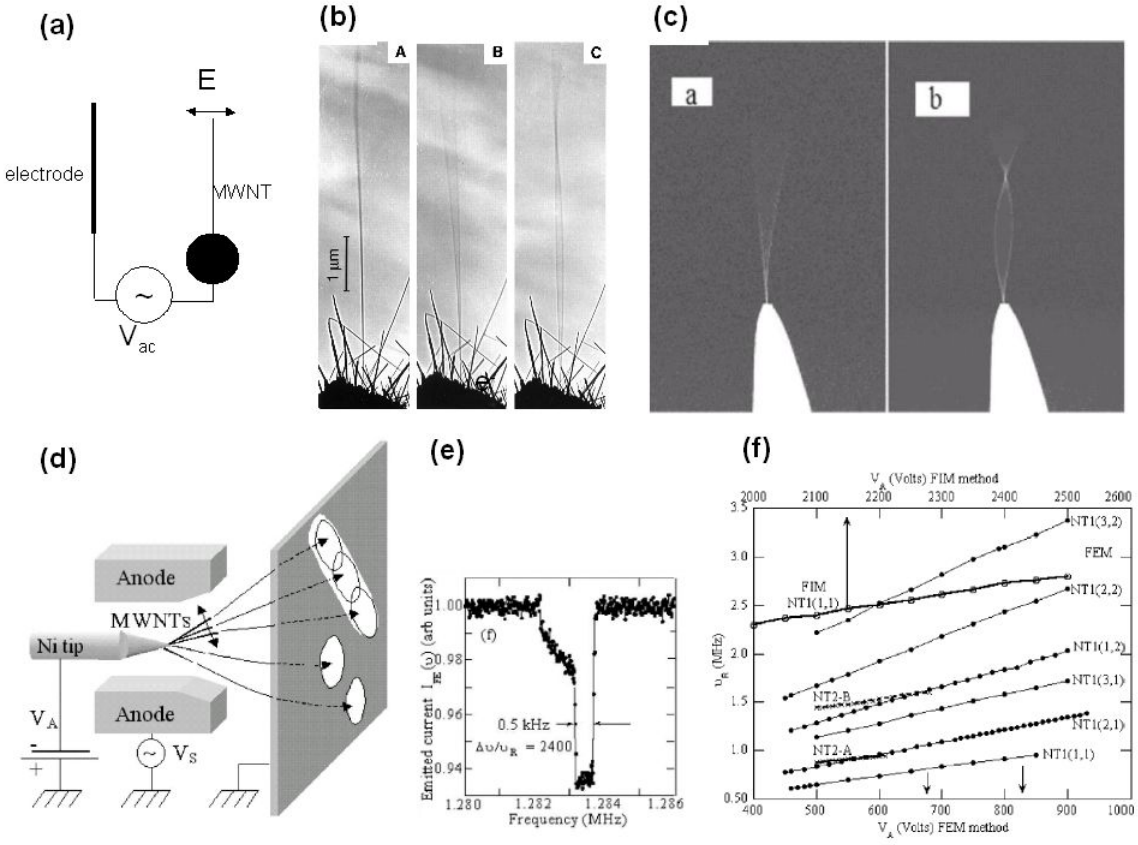

Figure 1.5: Previous work on CNT Resonators. **(a)** Experimental schematic for experiments by Poncharal and Gao. **(b)**,**(c)** Images of first and second harmonics of vibrating CNT cantilevers. **(d)** Experimental schematic for experiment by Purcell et al. **(e)** Emitted CNT current as a function of driving frequency. A drop in current on resonance can be observed. The peak is non-Lorentzian due to nonlinear detection. **(f)** Resonance frequency as a function of applied DC voltage V_A. The resonance frequency tunes linearly with the applied gate voltage.

the resonance frequency is given by (for derivation see Chapter 2)

$$\nu_n = \frac{\beta_n}{8\pi}\frac{1}{L^2}\sqrt{D^2 + D_i^2}\sqrt{\frac{E}{\rho}} \tag{1.5}$$

where L is the length of the CNT, ρ is the CNT mass density and D, D_i are the outer and inner diameters, respectively. From the measured resonance frequencies of 1MHz, the elastic modulus E could be extracted and was found to be in the range of $0.2 - 2$TPa. In both experiments, the extracted quality factors were on the order of 100 to 200, which was attributed mainly to the abundance of defects in pyrolysis and arc-discharge grown tubes.

Later, Purcell et al. (2002) grew MWNTs (typically $10 - 25$nm in radius and $10 - 40\mu$m long) by chemical vapor deposition (CVD) (Kong et al., 1998), which typically produces close to defect-free tubes. Actuation was done electrostatically. A nanotube, grown on a metallic tip (Fig. 1.5d), was placed between two electrodes. A DC voltage applied to the holder created a DC electric field along the CNT, which both doped the CNT with charge and applied a DC electric force on it. An AC voltage applied to the two electrodes created an AC electric field used for actuation of the resonance. The detection of the resonance was performed using the CNT as a field emitter. The DC voltage, V_A, applied to the CNT's holder was adjusted until the nanotube started emitting electrons, which were then accelerated to the detection screen. If a particular nanotube was moving, the pattern on the screen changed and the emission current dropped. Increasing the DC voltage beyond the amount necessary for detection increased the electric force along the CNT, thus increasing its tension. From simple arguments, it can be shown that the tension in the CNT T is given by

$$T = \gamma^2 V_A^2 \tag{1.6}$$

where γ is a constant defined by the geometrical factors and the electrostatic

environment. Being able to change a NT's tension allowed researchers to study the dependence of the resonance frequency on tension. For a tensed string it is expected that the frequency changes as the square root of tension. Thus, the resonance frequencies in this system were expected to follow (Purcell et al., 2002):

$$\nu_n = \frac{n}{2L^2}\sqrt{\frac{E}{\rho}} + \frac{n\gamma}{2L}\sqrt{\frac{1}{\mu}}V_A \tag{1.7}$$

and thus to change linearly with applied gate voltage. Such linear dependence was observed for all the measured resonances (see Fig. 1.5 f). The measured frequencies were on the order of 1MHz, similar to the previous experiments. Since the detection scheme of measuring the emission current was highly non-linear in the amplitude of vibration, the shape of the resonance (Fig. 1.5d) did not look Lorentzian as expected (see Section 2.2). Nonetheless, the effective quality factor (the line-width divided by the center frequency) for the resonances was measured, and was found to be roughly 2400.

Despite of the success of the detection methods described above, they still have several disadvantages. Firstly, using a TEM or SEM, or applying several hundred volts to detect the resonance is unrealistic for any industrial application. Secondly, as will be discussed in Appendix B, the electron beam used for imaging in TEM and SEM interacts with the CNT and even damages it both structurally and electrically. The detection scheme using the microscopes relies on visually determining the amplitude of vibration and is thus not very convenient and useful for any in-depth study of resonance properties, as the measurement is not automated. The field-emitter detection scheme has the disadvantage of being extremely non-linear and thus losing all of the information about the linear properties of the resonance. Lastly, all of these techniques are limited in their sensitivities to tens of nm vibration amplitudes by the resolution of the imaging beam. Such poor sensitivity may

push the operation of these resonators into the non-linear regime.

A fully electrically controlled detection/actuation method is highly advantageous for any possible future applications and/or research. In order to implement this method, we have decided to use the nanotube itself as a detector, thus requiring it to have at least two electrical contacts. This requirement restricts the mechanical structure to the doubly clamped geometry.

1.6 Summary and outline of thesis

Carbon nanotubes are a novel material that exhibits exciting electronic and mechanical properties. Their small size, high stiffness, great flexibility, and transistor properties make them ideal for use as a nano-electro-mechanical system (NEMS). In this thesis we will describe the first measurement of a NEMS device based on an individual SWNT. Chapter 2 gives an introduction to NEMS and to the theory of vibrating systems. Chapter 3 describes the process of making devices and the measurement setup used in this thesis. Chapter 4 describes the first measurements of a CNT resonator and presents a model for the frequency dependence on the parameters of the setup. Chapter 5 describes a quantitative analysis of the measured signals and discusses the sensitivities of the measurements and possible sources of noise. Lastly, chapter 6 discuses the possible sources of dissipation in the CNT resonator system and presents its dependence on temperature.

CHAPTER 2

OVERVIEW OF NANOELECTROMECHANICAL SYSTEMS

2.1 Introduction

In this chapter we will present a basic introduction to micro- and nanoelectromechanical systems (MEMS and NEMS). In this short review we will follow closely two main review articles: Ekinci and Roukes (2005) and Roukes (2000).

A typical electromechanical device can be described as a system where electrically controlled signals provide mechanical stimuli to a resonator, whose mechanical motion (typically the the displacement of the element) is then transduced back into electrical signals. Additional control electrical signals can be applied to change the two main parameters of the resonator: its resonant frequency $\omega_0/2\pi$ and quality factor Q. There are various types of geometries that are used in NEMS. Figure 2.1 shows some of the representative systems. In general, the two types of mechanical motions that are mostly used are flexural and torsional vibrations. An example of a flexural resonator is a doubly clamped beam, and an example of a torsional oscillator is a paddle. In this thesis we only consider flexural resonators, mainly doubly clamped beam and cantilever geometries.

In the linear regime of operation (when the displacement of the vibrating element is small) the mechanical structure can be approximated by a simple harmonic oscillator (section 2.2) and the resonant frequencies of these mechanical structures can be calculated using the methods of continuum mechanics. It has been shown by molecular dynamics simulation (Broughton et al., 1997, Phillips, 2001) that such calculations continue to be valid as the sizes of the structures shrink down to several tens of lattice constants in cross section. In section 2.3 we present a clas-

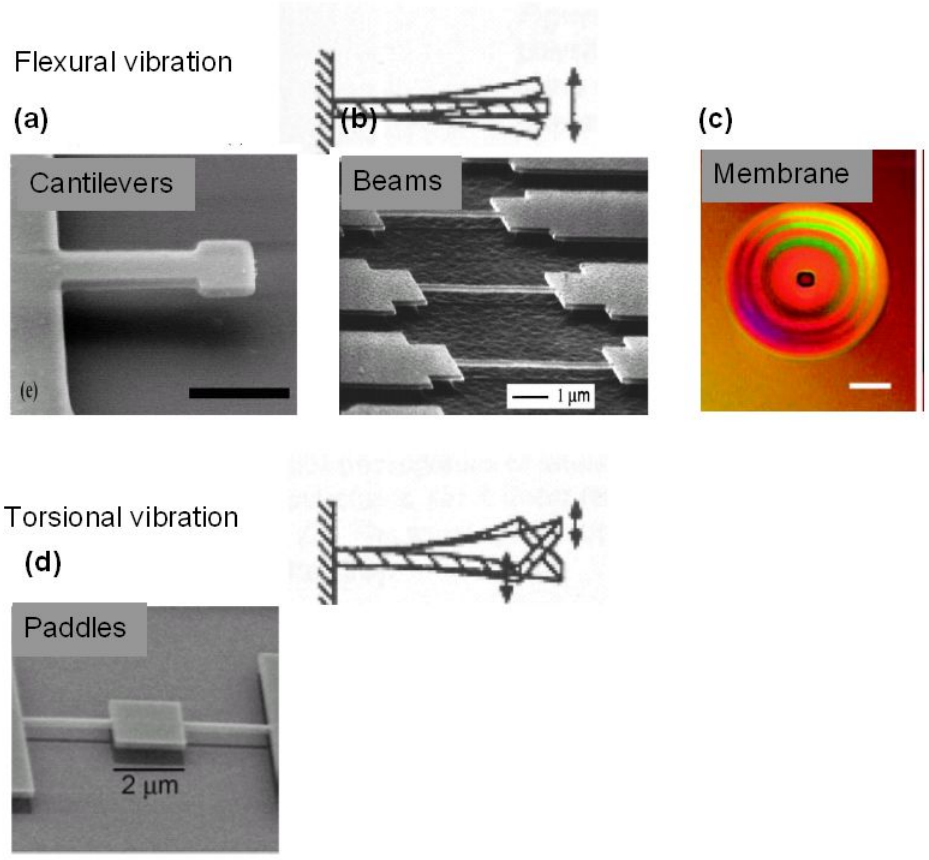

Figure 2.1: Examples of NEMS. **(a)**, **(b)**, **(c)** Examples of NEMS devices utilizing flexural vibration. **(a)** A cantilever (Ilic et al., 2004). **(b)** Doubly clamped beams (Cleland et al., 2001). **(c)** Suspended membrane (Zalalutdinov et al., 2003). **(d)** NEMS utilizing torsional vibration, a paddle (Sekaric et al., 2002).

sical calculation of the resonant frequency for a cantilever and a doubly clamped beam. Above the critical displacement of the mechanical structure various types of non-linearities in the restoring force of the system become increasingly important. These non-linearities can be caused by the elongation of the beam, imperfect clamping, or some kind of force gradient present in the system. This behavior of mechanical resonators is very useful for certain applications (Greywall et al., 1994, Turner et al., 1998, Carr et al., 2000, Erbe et al., 2000), such as memory and signal processing. We will present a short introduction to a typical behavior of a nonlinear oscillator whose restoring force contains a cubic term in section 2.4.

Experimentally, NEMS can operate at frequencies as large as 1GHz. Due to their small sizes, inducing and detecting the motion of the vibrating element at such high resonant frequencies becomes a challenge. A typical displacement sensitivity required for NEMS technology is on the order of $3\text{pm}/\sqrt{\text{Hz}}$ (Cleland et al., 2002) with the the onset of non-linearities at displacements on the order of nm. Standard optical approaches used in micro electromechanical systems (MEMS) such as optical interferometry (Wagner, 1990) and optical beam deflection (Bifano et al., 1999) are not easily scalable to the nano-sized resonators as they are limited by the diffraction of light. Electronic methods such as magnetic, magnetomotive, electrostatic, capacitive, piezoelectric, and piezoresistive techniques are also very hard to scale down as the effects of parasitic capacitance becomes increasingly important. In section 2.5 we describe several different detection methods that have been successfully used with NEMS.

Typical NEMS operate with quality factors in the range of $10^3 - 10^5$. These are values that are much higher than those typically available with electronic oscillators, but still inferior to MEMS. Ultrahigh quality factors are desirable as

they decrease the minimum operating power of the device, increase its sensitivity to external driving, and increase the device selectivity in the spectral domain. Such qualities are extremely useful in many applications such as filtering and signal processing. There are several factors that create losses in NEMS: air friction, clamping losses, surface effects, internal electronic losses and electronic losses due to external circuitry. The effect of these will be discussed in section 2.6.

High operating frequencies and high quality factors have made NEMS promising for a variety of different applications. We will present a short discussion of such applications in section 2.7.

2.2 Simple harmonic oscillator

The simplest one-degree-of-freedom oscillating system is a massless spring with a spring constant k and a mass m attached to it. If z is the variable that describes the position of the mass, the equation of motion for such a system is given by

$$m\ddot{z}(t) + kz(t) = 0 \tag{2.1}$$

The solution to this equation is

$$z(t) = z_0 \cos(\omega_0 t + \phi) \tag{2.2}$$

where $\omega_0 = \sqrt{k/m}$ is the resonant frequency of the oscillator, and z_0 and ϕ are the amplitude and the phase of the motion, respectively, which are defined by the initial conditions of the oscillator.

In a more realistic situation, a damping term and a driving force term are present. The damping term in general should not depend on the displacement (Marion and Thornton, 1995) but rather on the velocity of the mass. For simplicity

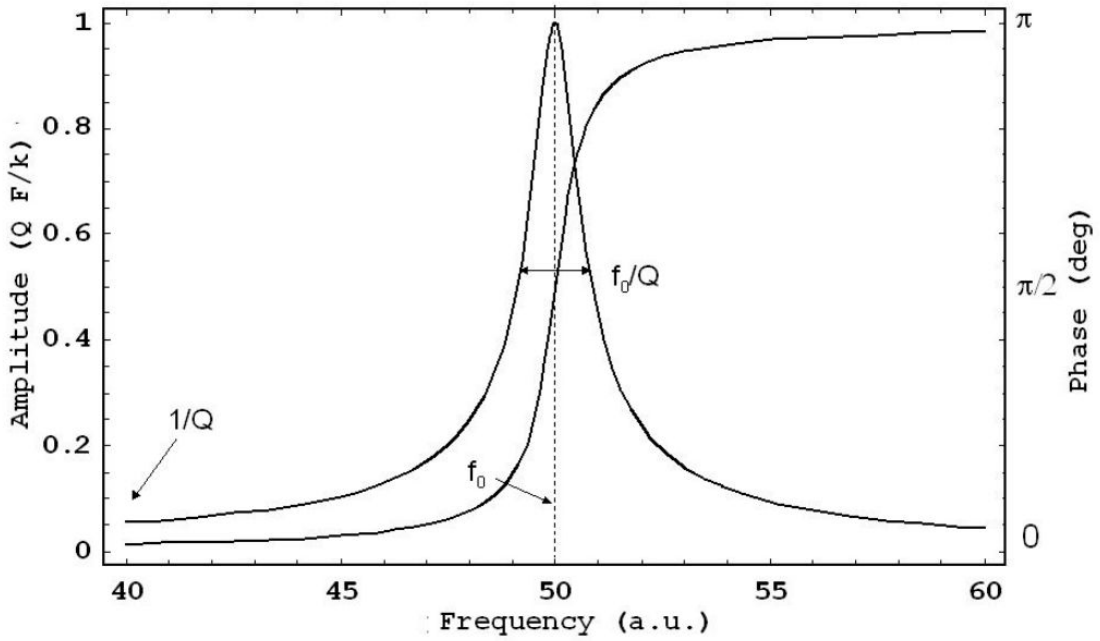

Figure 2.2: An amplitude and the phase of the SHO response as a function of the driving frequency. The amplitude of the response reaches the maximum at the resonance frequency $f_0 = 50$, while the off-resonance response is Q times smaller. At the same time the phase of the response goes through a 180° shift.

we assume sinusoidal driving. We thus modify Eq. 2.1 as follows:

$$m\ddot{z}(t) + b\dot{z}(t) + kz(t) = F_0 \cos(\omega t) \tag{2.3}$$

Solving for steady solution of the form presented in Eq. 2.2 we get that

$$z(t) = \frac{F_0/m}{\sqrt{(\omega_0^2 - \omega^2)^2 + 4\omega^2\beta^2}} \cos(\omega t - \phi) \tag{2.4}$$

$$\phi = \arctan(\frac{\omega_0^2 - \omega^2}{2\omega\beta}) \tag{2.5}$$

where

$$\beta = b/2m \tag{2.6}$$

$$\omega_0 = \sqrt{k/m} \tag{2.7}$$

To describe the degree of damping in the system we can define the quality factor in terms of the the energy loss in the system:

$$Q = 2\pi \left(\frac{\text{Total Energy}}{\text{Energy lost during one period}} \right) \tag{2.8}$$

We can show that for small damping the quality factor is given by $Q = \omega_0/2\beta$ or alternatively by $Q = \omega_0/\Delta\omega$, where $\Delta\omega$ is the full width at half maximum.

Figure 2.2 shows the frequency dependence of the amplitude and the phase of the response. We see that the amplitude is maximum at the free oscillator resonant frequency, reaching the value which is Q times higher than the non-resonant response. The frequency dependence is in the form of a Lorentzian and the width at half maximum is given by the product of the quality factor and the center frequency as described above. The phase of the signal goes through a 180° phase shift, with the response being $\pi/2$ out of phase with the drive at the center frequency.

2.3 Beam mechanics

We can now extend the theory above to the case of a more realistic resonant structure, such as a doubly clamped beam or a cantilever. First, we solve the equation of equilibrium for a beam subjected to a constant downwards force, and then we proceed to solving the dynamical properties of the vibrating beam.

There are two standard way to set up a beam's equation of equilibrium. The first is the technique of balancing all the forces and torques acting on a beam's subsection (Landau and Lifschitz, 1987, Shabana, 1997). Appendix A contains the detailed derivation of the equilibrium equation using this method. Alternatively we can find the configuration of a beam by energy considerations.

Consider a doubly clamped beam represented schematically in Figure 2.3. Let the coordinate system be set such that x is along the beam, and y, z are perpendicular to it. For simplicity we can assume that the cross-section of the beam is symmetric and all the forces are applied in the x-z plane. The problem then reduces to two dimensions. If E is the elastic modulus of the material and T is the tension in the beam, the elastic potential energy of the beam is given by (Landau and Lifschitz, 1987)

$$U = \frac{1}{2}\int_0^L \left(EIz''^2 + \left(T_0 + \frac{EA}{2L}\int_0^L z'^2 dx \right) z'^2 \right) dx \tag{2.9}$$

where T_0 is the residual tension in the beam, A is the beam's cross-sectional area, I is its moment of inertia, and the prime denotes differentiation with respect to x. We associate the first term with the flexural energy of the beam and the second term with the elastic energy in the beam due to the built-up tension. For small displacements, we can approximate the curvature of the beam, κ, with z'' and the strain in the beam, ϵ, with $\frac{1}{2}z'^2$. The product EI, referred to as *flexural rigidity*,

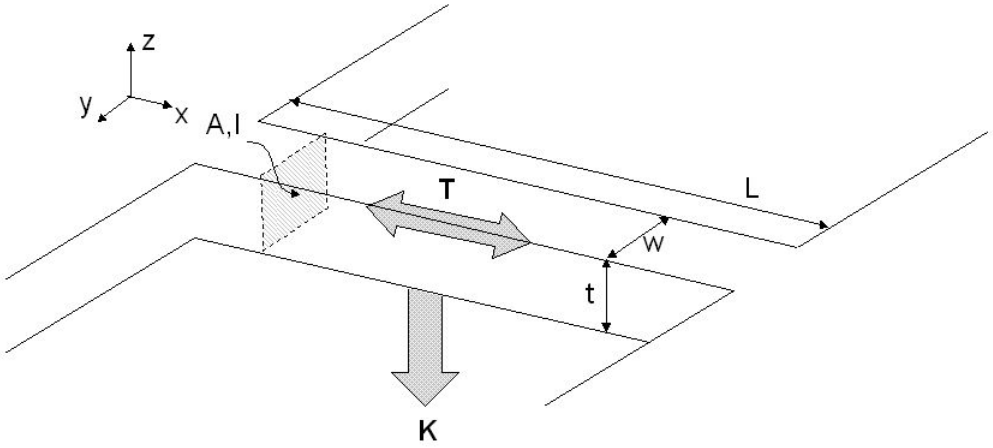

Figure 2.3: A schematic of a doubly clamped beam made out of material with elastic modulus E. The beam, with dimensions $t \times w \times L$, has a cross-sectional area A, and a moment of inertia I with respect to the z-axis. The beam is subject to a load $\vec{K}$, and tension $\vec{T}$.

denotes the force necessary to bend a beam by a unit of curvature, whereas the product EA, referred to as *extensional rigidity*, denotes the stress necessary to produce a unit strain. In the presence of a uniform downward force K, the total energy of the beam including the work done by the downward force simplifies to

$$U = \frac{1}{2}\int_0^L \left(EI\ \kappa^2 + T_0 + EA\ \epsilon^2 + Kz\right) dx \tag{2.10}$$

Minimizing this energy leads to the following equilibrium equation

$$EI\ \kappa'' - T_0 z'' - EA\ (\epsilon z)'' - K = 0 \tag{2.11}$$

or in terms of the total tension $T = T_0 + \frac{EA}{2L}\int_0^L z'^2$ and displacements

$$EIz'''' - Tz'' - K = 0 \tag{2.12}$$

We will now solve this equation in two different limits.

2.3.1 Bending limit

In the bending limit the tension is much smaller than the flexural rigidity $T \ll EI/L^2$ so that the second term of the equations can be neglected.

In order to calculate the resonant frequency of the system, we replace the external force K with $\mu\ddot{z}$. Here μ is the linear mass density of the beam. This leads to a wave equation

$$\mu\ddot{z} = EIz'''' \tag{2.13}$$

To solve this differential equation, we plug in a standard solution $z = z_0(x)\cos(\omega t + \phi)$. Equation 2.13 then reduces to

$$z_0'''' = k^4 z_0 \tag{2.14}$$

$$k^4 = \omega^2 \frac{\mu}{EI} \tag{2.15}$$

A general solution to this equation is:

$$z_0 = A\cos(kx) + B\sin(kx) + C\cosh(kx) + D\sinh(kx) \tag{2.16}$$

where we determine the constants A, B, C and D from the boundary conditions.

We consider two cases: first, a cantilever geometry, in which one end of the beam is free and the other is firmly clamped; and second, the doubly clamped beam geometry in which both ends of the beam are firmly clamped.

In the first case the cantilever geometry requires that at $x = 0$, we have $z = 0$ and $z' = 0$ and at $x = L$, we have $z'' = 0$ and $z''' = 0$. From that, we determine that

$$\begin{aligned} z_0 &= A\{[\cos(kL) + \cosh(kL)][\cos(kx) - \cosh(kx)] - \\ &\quad [\sin(kL) - \sinh(kL)][\sin(kx) + \sinh(kx)]\} \end{aligned} \tag{2.17}$$

The resonant frequencies are given by

$$\omega_n = \left(\frac{\beta_n}{L}\right)^2 \sqrt{\frac{EI}{\mu}} \tag{2.18}$$

where β_n are given by $\beta_n = k_n L$ and are determined by the equation

$$\cos(k_n L)\cosh(k_n L) = -1 \tag{2.19}$$

For the lowest mode of oscillation $\beta_0 = 1.88$.

In the second case, the doubly clamped condition requires that at $x = 0$ and at $x = L$ we have that both $z = 0$ and $z' = 0$. Consequently, we determine that

$$\begin{aligned} z_0 &= A\{[\sin(kL) - \sinh(kL)][\cos(kx) - \cosh(kx)]) - \\ &\quad [\cos(kL) - \cosh(kL)][\sin(kx) - \sinh(kx)]\} \end{aligned} \tag{2.20}$$

and that the resonant frequency is

$$\omega = \left(\frac{\beta_n}{L}\right)^2 \sqrt{\frac{EI}{\mu}} \tag{2.21}$$

where β_n are again given by $\beta_n = k_n L$ but now are determined by the equation

$$\cos(k_n L)\cosh(k_n L) = 1 \tag{2.22}$$

For the lowest mode of oscillation, $\beta_0 = 4.75$.

2.3.2 Tension limit

In the tension limit the tension is large compared to the flexural rigidity $T \gg EI/L^2$. In this case, Eq. 2.12 reduces to

$$Tz'' + K = 0 \tag{2.23}$$

Replacing K with $\mu\ddot{z}$, as in the previous section, leads to a wave equation

$$\mu\ddot{z} = Tz'' \tag{2.24}$$

the solution to this equation in a case of a doubly clamped beam is a standard wave defined by:

$$z = z_0 \cos(kx)\cos(\omega t + \phi) \tag{2.25}$$

where the resonant frequency ω is given by

$$\omega = \frac{\pi}{L}\sqrt{\frac{T}{\mu}} \tag{2.26}$$

As expected, we recover the simple "guitar string" vibrational modes.

2.3.3 Joining the two limits

In a realistic case, Eq. 2.12 has to be solved self-consistently accounting for both the flexural rigidity, EI, and the tension, T, which is found from the relation

$$T = T_0 + \frac{EA}{2L}\int_0^L z'^2 dx \tag{2.27}$$

where T_0 is the residual tension. Performing the calculation (Sapmaz et al., 2003) leads to second order corrections to the solutions found above for the two limits

$$\begin{aligned} \omega &= \tfrac{22.4}{L^2}\sqrt{\tfrac{EI}{\mu}} + 0.28T\sqrt{\tfrac{1}{\mu EI}}, \qquad && EI/L^2 \gg T \\ \omega &= \tfrac{\pi}{L}\sqrt{\tfrac{T}{\mu}} + \tfrac{2\pi}{L^2}\sqrt{\tfrac{EI}{\mu}}, && EI/L^2 \ll T \end{aligned} \tag{2.28}$$

2.4 Duffing oscillator

The discussion in the previous section was limited to the case of a linear system. However, in a realistic system various type of nonlinearities are present. In the case of doubly clamped beams, a nonlinear restoration force comes from the elongation of the beam as it vibrates. Accounting for the tension in the beam due to strain, we get the following equation of motion, also known as a Duffing oscillator (Nayfeh and Mook, 1979):

$$\ddot{z}(t) + \frac{\omega_0}{Q}\dot{z}(t) + \omega_0^2 z(t) + \varepsilon z^3 = \frac{F_0}{m}\cos(\omega t) \tag{2.29}$$

where for the case of doubly clamped beam $\omega_0 = \frac{22.4}{L^2}\sqrt{\frac{EI}{\mu}}$ as defined in the previous section, and $\varepsilon = \frac{E}{18\rho}\left(\frac{2\pi}{L}\right)^4$ (Postma et al., 2005)

Figure 2.4 shows a typical response of a Duffing oscillator as the amplitude of vibration is increased. For small amplitudes, the response is Lorentzian, but above the critical amplitude a_c the peak is pulled over toward higher frequencies. At this point, there are three solutions to Eq. 2.29: two stable solutions and one unstable. The response then develops a hysteretic switching as the frequency is swept up and down (Figure 2.4b) The onset of nonlinearity due to elongation of the beam is expected at (Nayfeh and Mook, 1979)

$$a_c = \omega_0\sqrt{\frac{8}{3\sqrt{3}\varepsilon Q}} \tag{2.30}$$

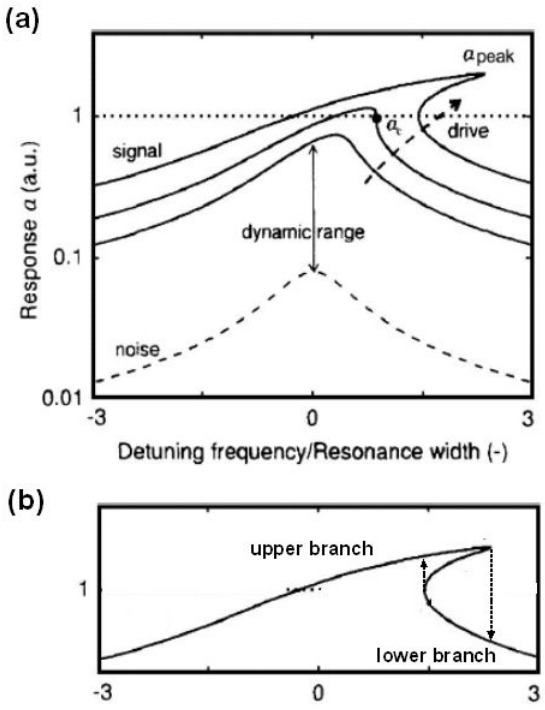

Figure 2.4: Nonlinear resonator response. **(a)** Resonator response vs driving frequency for increasing vibration amplitude. **(b)** Example of hysteresis for nonlinear resonator.

which for the case of the nonlinearity presented above reduces to (Postma et al., 2005)

$$a_c = \omega_0 \frac{L^2}{\pi^2} \sqrt{\frac{\rho\sqrt{3}}{EQ}} \tag{2.31}$$

For a circular beam with diameter d, moment of inertia $I = \pi d^4/64$, and cross-sectional area $A = \pi d^2/4$, this converts to

$$a_c = \frac{2}{\sqrt[4]{3}} \sqrt{\frac{d^2}{4Q}} \tag{2.32}$$

2.5 NEMS actuation and detection techniques

To study realistic resonating systems we need a way to induce and detect their mechanical motion. Below we describe several different methods of actuating and detecting the vibrations.

2.5.1 Actuation

Piezo

In the simplest scenario, the mechanical structure can be placed on a vibrating substrate to induce oscillations. A commercially available piezo is typically used for this purpose (Li and Evoy, 2005). This is a very simple and readily available technique; however, there are several complications that arise with it. The frequency response of the piezo is very non-uniform even in the region of interest for MEMS and attenuates fast at higher frequencies (100MHz) making it very hard to quantify the force applied to the resonator. The voltages required to drive the piezo are on the order of volts, making electrical detection difficult, as the capacitive leakage currents interfere with the detection signal.

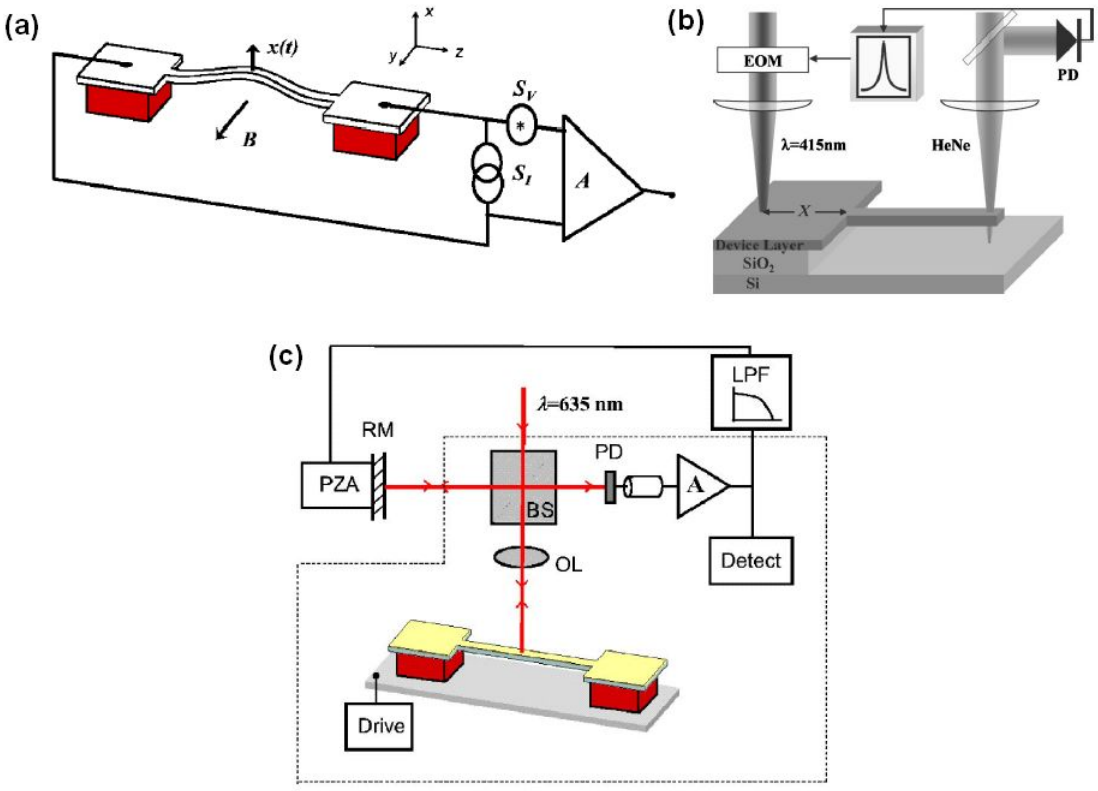

Figure 2.5: **(a)** Magnetomotive setup (Ekinci and Roukes, 2005). **(b)** Optical actuation setup (Ilic et al., 2005). **(c)** Optical interferometric setup (Ekinci and Roukes, 2005).

Magnetic - Lorentz force

In the magnetic actuation scheme, a conducting mechanical structure (typically a doubly clamped beam in a conducting loop) is placed in the presence of a static magnetic field, B, perpendicular to the plane of vibration (see Fig. 2.5a) (Cleland and Roukes, 1996). Passing an AC current, I, through the beam induced an AC Lorentz force, F_{Lorentz}, that drives the beam.

$$F_{\text{Lorentz}} = IBL \tag{2.33}$$

where L is the length of the beam.

Electrostatic

In the electrostatic actuation technique, a conducting mechanical structure is placed in a presence of an AC electric field created by applying an AC voltage, V, to a nearby electrode (Carr and Craighead, 1997). The electrostatic force on the mechanical structure is then given by

$$F_{\text{electrostatic}} = \frac{1}{2}V^2C' \tag{2.34}$$

where C' is the spatial derivative of the beam-electrode capacitance.

Optical

Recently (Ilic et al., 2005) an optical actuation scheme was realized with NEMS. In such a scheme, an AC-modulated laser is focused near the resonating structure (see Fig. 2.5b). The AC laser power is converted into heat, producing an oscillatory stress field in the material and causing the resonant structure to vibrate. The advantage of such an excitation scheme is that it doesn't require any electrical

contacts to the resonating structure, while the disadvantage is that the effectiveness of the drive depends directly on the proximity of the laser spot to the structure and the thermal conductivity of the material. As the sizes of resonators shrink down, such an excitation scheme is harder and harder to realize.

2.5.2 Detection

Imaging

The simplest qualitative detection scheme can be achieved by placing a vibrating structure into a microscope, for example a scanning electron microscope (SEM) or a transmission electron microscope (TEM), and directly observing the vibrations of the structure. Despite the simplicity of this technique, it is hard to extract quantitative information about the vibrations of the resonator as the detector should be capable of taking images faster then the resonance frequency of the studied structure, which for NEMS is in the MHz range. Moreover, this is a very invasive measurement, as will be discussed in Appendix B. And finally, this measurement technique does not allow one to vary any parameters in the environment of the resonator such as air pressure, presence of adsorbates, or temperature.

Optical

In the optical interferometry detection scheme (see Fig. 2.5c) a tightly focused laser beam reflects off the structure and interferes with a reference beam, typically the part of the beam that goes through the vibrating structure and reflects off the substrate. However, extending these techniques into the domain of nanoscale resonators proves to be challenging, due to their small cross section, but was realized in the past (Carr et al., 1999). This technique is typically used in conjunction with

electrostatic actuation.

Magnetomotive

The magnetomotive detection technique is normally used with the magnetic actuation technique, for doubly clamped beam structures. As the beam vibrates, the flux enclosed by the conducting loop varies, creating an electromotive force (EMF) across the beam. This EMF can be detected by an amplifier connected to the circuit (Cleland and Roukes, 1996). Even though this is currently the most widely used technique for NEMS, it has significant drawbacks for small resonators, whose resistances are typically much higher than the impedance of the measuring circuit, making it difficult to detect high frequency signals. Even if the impedance of the resonator is matched to the external circuit, the the dissipative force created due to this detection technique dominates the drive for small resonators (Schwab, 2002), as the loss is inversely proportional to the mass of the resonator (see section 2.6).

Capacitive

In the capacitive detection scheme, changes in the capacitance between a vibrating mechanical structure and a nearby electrode are measured (Nguyen, 1998). Since in nanoscale-sized resonators these capacitances are usually on the order of 10^{-18}F, the detection is complicated by the presence of parasitic capacitances that are several orders of magnitude larger. This challenge is usually overcome by the use of balanced bridge techniques or by placing an amplifier, such as, for example, a single electron transistor (LaHaye et al., 2004), in close proximity to the resonator.

Piezoelectric and piezoresistive

In a piezoelectric detection scheme, a mechanical structure covered with the piezoelectric medium creates AC polarization electric fields at the points of maximum strain. These electric fields can be detected by placing a gate of a field effect transistor (Beck et al., 1998) or a single electron transistor (Knobel and Cleland, 2003) on top of the piezoelectric medium at these points.

The piezoresistive detection scheme was realized only recently for NEMS (Bargatin et al., 2005). In such a detection scheme, the strain-dependent resistance of a mechanical element made out of a piezoresistive material such as doped Si or AlGaAs, is measured.

The large resistances of these small structures complicate these methods. This complication is inherent to all of the detection methods that measure charge through small structures. At high resonance frequencies, such high resistances lead to a frequency-dependent signal attenuation due to a high RC time constant. There are two different methods to work around this problem. One is to transform the impedance of the measured device to 50Ω at the frequency of interest (Hagen, 1996, Schoelkopf et al., 1998). A drawback is that the measurement circuit has to be rebuilt for each individual device. Another method is to use some nonlinear component in the circuit (such as the piezoresistor or an SET) to perform downmixing at a much lower frequency, where the signal attenuation is not large (Hagen, 1996, Knobel and Cleland, 2003, Bargatin et al., 2005).

2.6 Losses

The degree of loss in a resonator is characterized by the quality factor Q given by Eq. 2.8. The inverse of the quality factor describes the relative energy loss per

cycle and is additive for different processes. The energy losses in NEMS can be divided into two categories. The first are intrinsic losses that come due to some imperfections or interactions within the structure or from fundamental processes within the lattice such as defects, phonon-phonon interactions, electron-phonon interactions, etc. They are sometimes referred to as the "internal friction". The second are the extrinsic losses that arise due to interactions with the surrounding media such as air friction, clamping, measurement scheme, etc. In this section we describe some of these loss mechanisms in greater detail; a summary of the dissipation mechanisms is provided in table 2.1.

2.6.1 Intrinsic losses

The intrinsic losses can be divided into two categories: dissipation due to fundamental processes in the lattice that occur even in a perfect crystal, and dissipation from imperfections of the lattice, such as defects and impurities. The main fundamental processes are phonon-phonon interactions and electron-phonon interactions. These dissipation mechanisms set the absolute limit to the performance of a mechanical resonator. Additional dissipation comes from imperfections of the material both in bulk (impurities, dopants, and electron traps) and on the surface (dangling bonds, adsorbates, etc). Below we describe in detail some of these processes. For a more thorough review see Nowick and Berry (1972) and Braginsky et al. (1985).

Many of these processes can be treated in the framework of a standard anelastic solid (Nowick and Berry, 1972). The basic idea behind this model is that mechanical vibration of a solid takes the system out of equilibrium. For an anelastic solid, such a configuration is not stable, and the system relaxes to equilibrium through

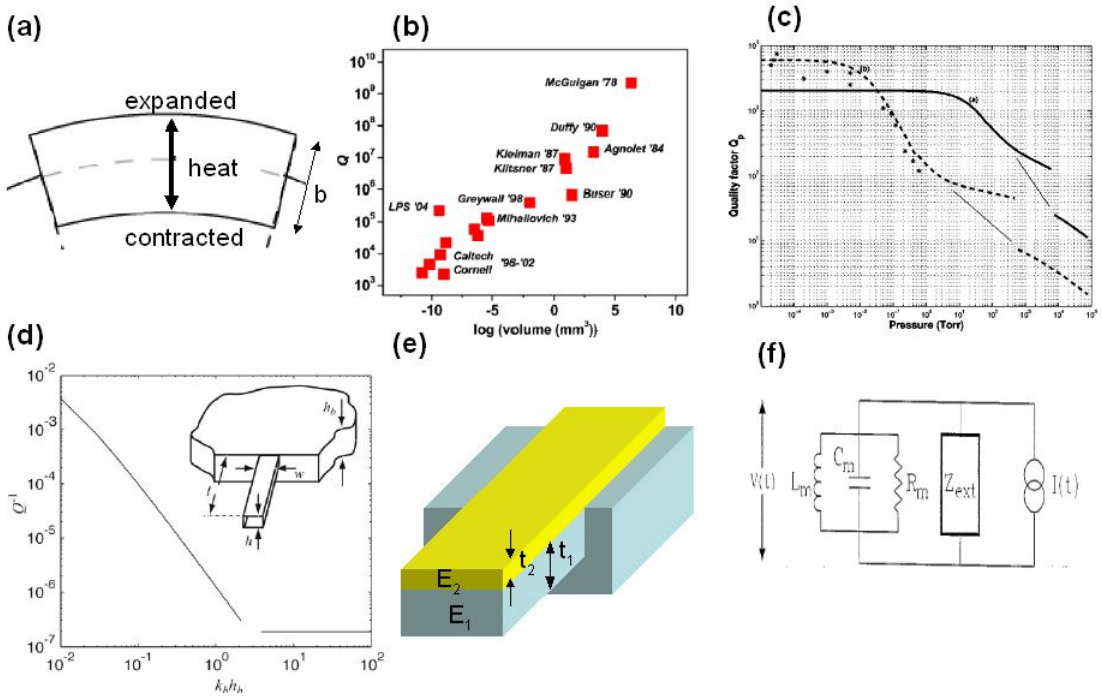

Figure 2.6: Various dissipation mechanisms. **(a)** Thermoelastic effect. **(b)** Quality factor dependence on the size of the resonator illustrating the importance of surface effects (Ekinci and Roukes, 2005). **(c)** Calculated quality factor for NEMS as a function of gas pressure (Bhiladvala and Wang, 2004). **(d)** Dissipation due to clamping. Dependence of the losses on the thickness of the supporting base (Photiadis and Judge, 2005). **(e)** A double layer cantilever structure. **(f)** The equivalent electronic circuit for a resonator (Cleland and Roukes, 1999).

various mechanisms with a finite relaxation time τ. We can modify the Hooke's stress-strain relation to include the mechanical relaxation as (Cleland et al., 2002)

$$\sigma + \tau_\epsilon \frac{d\sigma}{dt} = E_{\mathrm{R}} \left(\epsilon + \tau_\sigma \frac{d\epsilon}{dt} \right) \tag{2.35}$$

Here E_{R} is the relaxed elastic modulus. The relaxation mechanisms include everything from interaction with point-defects to thermal relaxation. Such relaxation leads to dissipation of energy from the mechanical mode whose functional form is given by

$$Q^{-1} = \Delta \left(\frac{\omega\tau}{1 + (\omega\tau)^2} \right) \tag{2.36}$$

where ω is the mechanical vibration frequency and Δ is the mechanism-dependent dissipation strength defined by the relaxed elastic modulus and the relaxation times in the following fashion (Cleland et al., 2002)

$$\Delta = \frac{E_{\mathrm{U}} - E_{\mathrm{R}}}{\sqrt{E_{\mathrm{R}} E_{\mathrm{U}}}} \tag{2.37}$$

where $E_{\mathrm{U}} = E_{\mathrm{R}}\tau_\sigma/\tau_\epsilon$ is the unrelaxed elastic modulus. The relaxation time, τ, is also mechanism dependent and is defined by the relaxation times of the stress and strain as

$$\tau = \sqrt{\tau_\sigma \tau_\epsilon} \tag{2.38}$$

Such dissipation has the form of a Lorentzian in frequency domain, and is often referred to as a "Debye peak".

In the case of the temperature activated process, the relaxation time is given by the *Arrhenius* equation

$$\tau = \nu_0^{-1} e^{E_0/k_{\mathrm{B}}T} \tag{2.39}$$

where ν_0 is the attempt frequency, and E_0 is the activation energy. In this case as the temperature is changed, τ changes accordingly, producing the maximum

dissipation at the temperature, $T_{\rm p}$, where $\tau \approx \omega^{-1}$. Since at that temperature

$$\ln(\omega\tau) + \frac{E_0}{k_{\rm B}}\frac{1}{T_{\rm p}} = 0 \tag{2.40}$$

by measuring $T_{\rm p}$ for the several different frequencies, the activation energy can be measured. The activation temperature $T_0 = E_0/k_{\rm B}$ is then given by the slope of $\ln(\omega)$ vs. $1/T_{\rm p}$.

Phonon-phonon interactions

A realistic crystal lattice is always slightly anharmonic. The degree of anharmonicity in the lattice is typically described by the Gruneisen constant, γ, that is essentially the first nonlinear coefficient between the stress and strain in a solid. This nonlinearity allows for the possibility of energy transfer between the normal vibrational modes of the crystal or phonon-phonon scattering. For a mechanical resonator, this means that an acoustical vibrational mode can dissipate energy into the higher energy thermally populated vibrational modes. Calculating losses for such a mechanism has been approached for two different limits of the phonon mean free path compared to the wavelength of the acoustic mode.

The first case, the ballistic limit, occurs when the phonon mean free path, l_T, is comparable to the the acoustic wavelength or the dimension of the resonator, $l_T \sim L$; the thermal phonons then can be regarded as individual particles in a kinematic picture. The driven resonant mode can be viewed as an acoustical phonon of wavelength L. The losses to the resonator are due to individual scattering events between the acoustical and thermal phonons (the so-called *Landau-Rumer effect*). The losses in such a case are typically calculated numerically.

The second case, the diffusive limit, occurs when $l_T \ll L$. Here the acoustic mode can be treated as perturbing the local distribution of the phonons, and losses

come from thermal phonons relaxing to equilibrium, the so-called *Akhizer effect*. The phonons are regarded as a viscous "thermal gas" for the acoustic mode. For the theoretical and experimental discussion of this process see Braginsky et al. (1985) and Nowick and Berry (1972).

In the extreme diffusive limit, however, the phonons thermalize so quickly that they can be considered as just creating a temperature field. In this limit, we can approach the problem classically using thermodynamical arguments. The interactions between the mechanical degree of freedom and the phonons are captured in the thermal expansion coefficient, α, which can be related to the Gruneisen constant (Lifshitz, 2002). This limit of phonon-phonon dissipation due is called *thermoelastic effect*, we discuss it below in more detail.

Thermoelastic effect

The thermoelastic effect is one of the main sources of dissipation in small mechanical systems (Roszhart, 1990, Yasumura et al., 2000). The theory was first developed by Zener (Zener, 1948) and further developed for thin vibrating beams by Lifshitz and Roukes (Lifshitz and Roukes, 2000). The idea behind thermoelastic dissipation (TED) is that the local volume changes induced by mechanical vibration lead to a temperature gradient across the resonator, and to the heat flow from the hot to the cold regions. The problem can be solved in the framework of a standard model for an anelastic solid described above.

To derive the strength of the dissipation due to the thermoelastic effect we go back to Eq. 2.37. We can identify the relaxed and unrelaxed elastic moduli with the isothermal and adiabatic elastic moduli, respectively. Thus for a stress, σ, and

a strain, ϵ, the moduli are given by:

$$\begin{aligned} E_{\mathrm{R}} &= \left(\tfrac{\partial\sigma}{\partial\epsilon}\right)_T \\ E_{\mathrm{U}} &= \left(\tfrac{\partial\sigma}{\partial\epsilon}\right)_s \end{aligned} \tag{2.41}$$

where T and s are temperature and entropy, respectively.

Before calculating Δ, we note that $E_{\mathrm{R}} - E_{\mathrm{U}}$ is small and that we can replace the product of the moduli in the denominator by E_{R}^2. Eq. 2.37 then reduces to

$$\Delta = \frac{E_{\mathrm{U}} - E_{\mathrm{R}}}{E_{\mathrm{R}}} = \frac{J_{\mathrm{R}} - J_{\mathrm{U}}}{J_{\mathrm{U}}} = \frac{J_{\mathrm{R}} - J_{\mathrm{U}}}{J_{\mathrm{R}}} \tag{2.42}$$

where $J_{\mathrm{U,R}} = 1/E_{\mathrm{U,R}}$ is the compliance. We then proceed by calculating the relaxed and unrelaxed compliances from thermodynamical principles.

Writing down the free energy equation in its differential form

$$dg = -sdT - \epsilon d\sigma \tag{2.43}$$

we arrive at

$$\left(\frac{\partial s}{\partial \sigma}\right)_T = \left(\frac{\partial \epsilon}{\partial T}\right)_\sigma \equiv \alpha \tag{2.44}$$

We also know that by definition

$$\left(\frac{\partial s}{\partial T}\right)_\sigma = \frac{C_\sigma}{T} \tag{2.45}$$

Using a property of partial derivatives and the equations above, we can derive that

$$\left(\frac{\partial T}{\partial \sigma}\right)_s = -\left(\frac{\partial T}{\partial s}\right)_\sigma \left(\frac{\partial s}{\partial \sigma}\right)_T = -\frac{\alpha T}{C_\sigma} \tag{2.46}$$

And using Eq. 2.41, we arrive at

$$J_{\mathrm{U}} = \left(\frac{\partial \epsilon}{\partial \sigma}\right)_s \tag{2.47}$$

$$= \left(\frac{\partial \epsilon}{\partial \sigma}\right)_T + \left(\frac{\partial T}{\partial \sigma}\right)_s \left(\frac{\partial \epsilon}{\partial T}\right)_\sigma \tag{2.48}$$

$$= J_{\mathrm{R}} + \frac{-\alpha T}{C_\sigma}\alpha \tag{2.49}$$

The dissipation strength is then given by

$$\Delta = \frac{\alpha^2 T E}{C} \tag{2.50}$$

where we have replaced the heat capacity at constant stress, C_σ, by the heat capacity at constant pressure, C. The overall value of loss is given by

$$Q^{-1} = \frac{\alpha^2 T E}{C}\left(\frac{\omega\tau}{1+(\omega\tau)^2}\right) \tag{2.51}$$

The elastic modulus relaxation time, τ, is given by the time it takes for heat to travel from the expanded to the contracted regions of the beam. In case of a transverse acoustic wave (flexural vibration) it is given by

$$\tau = \frac{t^2 C}{\pi^2 \kappa} \tag{2.52}$$

Here t is the thickness of the beam, and κ is the heat conductance. For a longitudinal wave, the relaxation time is defined by the wavelength of the wave, λ, rather than the thickness of the beam, and is given by

$$\tau = \frac{\lambda^2 C}{(2\pi)^2 \kappa} \tag{2.53}$$

Since only mechanical modes that produce volume changes are subject to TED, the other modes such as pure torsional modes are lossless.

Electron-phonon interactions

For metallic resonators, the mechanical motion of the resonator results in ion oscillation and creation of an oscillatory electrical field. The free electrons can be viewed as a viscous gas that moves in this field and dissipates energy. The dissipation of longitudinal sound waves in this case were theoretically calculated to be (Braginsky et al., 1985)

$$Q^{-1} = \frac{8}{15}\frac{E_F m_e \sigma \omega}{\rho v^2 e^2} \tag{2.54}$$

where E_F is the fermi energy, and e and m_e are the electron charge and mass, σ is the electric conductivity, ρ is the density, and v is the velocity of longitudinal sound wave.

Two-level systems

Internal defects such as contamination, impurities, and dangling bonds can also contribute to losses in a mechanical oscillator. Such dissipation is often caused by phonon capture by the defect and involves transition between two energy minima (Mohanty et al., 2002). This mechanism can be effectively described using the formalism of two-level systems (TLS). Mohanty et al. (2002) have calculated that for a TLS with energy E the additional dissipation for two limiting cases of E is given by

$$Q^{-1} = 2a\frac{\omega\gamma_0}{(\omega_0^2 + \gamma_0^2)}\frac{e^{-2E/k_BT}}{kT} \tag{2.55}$$

for $E \gg k_BT$. And

$$Q^{-1} = \frac{d}{T^2} \tag{2.56}$$

for $E \ll k_BT$. Here a, d, and γ_0 are constants defined by the coupling of the TLS to the local strain.

Surface effects

Recent experiments (Ekinci and Roukes, 2005) show that the measured quality factor in many devices decreases in a linear fashion as the surface-to-volume ratio is increased (Fig. 2.6b). This suggests that surface losses play a significant role in determining the quality factor. The losses associated with the surface can come from many different factors such as residue, poorly terminated bonds in the surface states, and a water layer. It has been shown that various surface treatments such as

annealing (Yasumura et al., 2000), oxygen removal from the surfaces (Yang et al., 2000, 2001), and surface passivation using methyl monolayers (Wang et al., 2004) can decrease the dissipation in mechanical resonators by as much as an order of magnitude.

2.6.2 Extrinsic losses

Air friction

Depending on the pressure in the measuring chamber, the losses due to mechanical structure interacting with air can be divided into two categories. At very low pressures the interaction is in the "molecular" regime where the mean free path of a single molecule is much larger than the length scale of the device. Here the losses are due to the individual collisions with the molecules. The energy loss in a cycle Q_{gas}^{-1} has been calculated for MEMS (Blom et al., 1992) and for NEMS (Bhiladvala and Wang, 2004) to be

$$Q_{\text{gas}}^{-1} = \frac{pA}{m_{\text{eff}}\omega_0 v} \tag{2.57}$$

where p is the pressure in the chamber, A is the surface area of the resonator, m_{eff} is the effective mass of the oscillator, ω_0 is its resonant frequency, and v is the thermal velocity of the gas molecules. See Fig. 2.6c.

At higher pressures, air can be considered as a viscous fluid. In this regime the losses from air drag are given by $Q_{\text{gas}}^{-1} \sim \sqrt{p}$ (Landau, 1982).

Clamping

A resonator can lose energy to the support structure by acoustic coupling. This is especially important in the doubly-clamped beam geometry. Experiments with

identical nanoscale beams with different clamping geometries showed that an improvement of ~ 2.5 can be achieved in free-free beams over doubly-clamped beams (Huang et al., 2003b).

Several different groups attempted to calculate the dissipation due to clamping. Jimbo and Itao (1968) were the first to give an estimate for the case of a thin, infinitely wide cantilever attached to an infinite base:

$$Q^{-1} \approx \left(\frac{t}{L}\right)^3 \tag{2.58}$$

where t, L are the thickness and the length of the cantilever, respectively. Cross and Lifshitz (2001) performed calculations for the opposite limit where the base is the same thickness as the cantilever and arrived at an approximation of the quality factor of:

$$Q^{-1} \sim \left(\frac{t}{L}\right) \tag{2.59}$$

Recently, (Photiadis and Judge, 2005) performed a calculation in a more general case of a narrow (compared to wavelength) cantilever attached to a finite thickness base (Fig. 2.6d). Their estimation for loss was:

$$Q^{-1} \approx \frac{w}{L}\left(\frac{t}{L}\right)^4 \tag{2.60}$$

for the fundamental vibrational mode, where w is the width of the cantilever.

Double-layer structures

For metallized devices, or for other double-layered structures, the additional layer can also contribute to dissipation. This was observed experimentally for metallized doubly-clamped beams (Sekaric et al., 2002) and metallized paddles (Olkhovets et al., 2000). White and Pohl (1995) calculated the contribution of a layer with

internal friction Q_2, thickness t_2, and elastic modulus E_2, to a system with internal friction Q_1, thickness t_1 and elastic modulus E_1 (Fig. 2.6e). Defining $\beta = t_2 E_2 / t_1 E_1$, leads to

$$Q^{-1} = \frac{1}{1+\beta}(Q_1^{-1} + \beta Q_2^{-1}) \tag{2.61}$$

Dissipation due to the measuring scheme

The resonance actuation and detection techniques often require that additional currents (or voltages) are passed through (or created across) the resonator. Depending on the parameters of the resonator, these may lead to dissipative forces. We can describe this effect with a magnetomotive actuation/detection technique (see section 2.5) following Cleland and Roukes (1999).

In a magnetomotive detection scheme, a driving current, I_d, is passed through a resonator in the presence of magnetic field B. The motion of the resonator in the magnetic field induces an EMF across the resonator given by

$$V_{\mathrm{EMF}} = \alpha L B \frac{dz(t)}{dt} \tag{2.62}$$

where α, and L are the mode's shape factor and the resonator length, and $z(t)$ is the midpoint displacement of the resonator. For an infinite external impedance, the voltage is given by

$$V_{\mathrm{EMF}} = i \frac{\frac{\alpha L^2 B^2}{m\omega}}{\left(\frac{\omega_0}{\omega}\right)^2 - 1 + i\frac{\omega_0}{\omega Q_0}} I_d \tag{2.63}$$

where Q_0 is the mechanical quality factor of the resonator. This is equivalent to an electrical circuit (see Fig. 2.6e) with a parallel combination of a resistor R_m,

inductor L_m, and a capacitor C_m given by (Cleland and Roukes, 1999)

$$\begin{aligned} C_m &= \tfrac{m}{\alpha L^2 B^2} \\ L_m &= \tfrac{\alpha L^2 B^2}{\omega_0^2 m} \\ R_m &= \tfrac{\alpha L^2 B^2}{\omega_0^2 m} Q_0 \end{aligned} \tag{2.64}$$

which leads to a characteristic impedance $Z_c = \sqrt{L_m/C_m}$. For a finite external impedance Z_{ext}, the additional dissipation is given by

$$Q^{-1} = \frac{Z_c R_{\text{ext}}}{|Z_{\text{ext}}|^2} \tag{2.65}$$

Approximating the impedance of an external circuit by resistance R, the expression above simplifies to

$$Q^{-1} = \frac{L^2 B^2 \alpha}{Rm\omega_0^2} \tag{2.66}$$

Similar analysis has been done for the case of magnetic driving and capacitive detection (Schwab, 2002).

Ohmic losses

Another type of loss associated with external circuits are ohmic losses from the electrons moving on and off the resonator due to capacitive coupling to a nearby gate. This is another example of a loss that we can describe in the "Debye peak" framework.

We first estimate the dissipation strength for this effect. The system can be represented as a variable capacitor in series with a resistor to which a voltage V is applied. The change in the capacitance is determined by the amplitude of oscillation, z, as $\Delta C = C'z$, where C' is the spatial derivative of the capacitance. The capacitively induced charge is given by $\Delta q = \Delta C V = C' z V$.

If the time scales for the electrons to flow on the resonator and the time for one oscillation are matched perfectly, all of the charge flows through a resistor, dissipating energy through Joule heating. The time scale for this charge to flow is given by the RC constant of the circuit, $t = 2\pi RC$. The energy dissipated on the resistor for this change in the capacitance is then

$$\phi = I^2 Rt = \frac{(\Delta q)^2 R}{t} = \frac{(C'Vz)^2 R}{2\pi RC} \tag{2.67}$$

The energy stored in a resonator is given by $E = 1/2kz^2$, where k is the resonator spring constant. The dissipation strength is then

$$\Delta = \frac{(C'V)^2}{\pi kC} \tag{2.68}$$

The actual loss is given by the product of the maximum loss and the Lorentzian defining the relative time scales for capacitance change, $1/\omega$ and the electron flow time $\tau = RC$. The loss is then given by

$$Q^{-1} = \frac{(C'V)^2}{\pi kC}\left(\frac{\omega\tau}{1+(\omega\tau)^2}\right) \tag{2.69}$$

2.7 Applications

Their small sizes and high frequency of operation make NEMS useful for a variety of different of applications such as signal processing (Nguyen, 1999), mass detection (Ekinci et al., 2004, Ilic et al., 2004), force sensing (Stowe et al., 1997, Rugar et al., 2004), and fundamental studies of quantum mechanics in a mechanical system (LaHaye et al., 2004). In this section we will outline the principles behind two of these application and give the limits of their performance.

Table 2.1: Various dissipation processes and the losses associated with them. The expressions are given for a doubly clamped beam (or a cantilever for the case of clamping) with the following parameters. The resonator is of dimension $t \times w \times L$, and has cross-sectional area A and resonance frequency ω_0. m is its effective mass and E, c, κ, α are the material's elastic modulus, specific heat, heat conductivity and linear expansion coefficient, respectively. The resonator is in the presence of magnetic field B and air pressure p, and it has capacitance C to an electrode with voltage V. The resonator's electrical resistance is R.

Dissipation process	Q^{-1}	**References**
Air friction	$\frac{pA}{m\omega_0 v}$	Bhiladvala and Wang (2004)
Clamping	$\approx \frac{w}{L}\left(\frac{t}{L}\right)^4$	Photiadis and Judge (2005)
Metallic layer	$\frac{1}{1+\beta}(Q_1^{-1} + \beta Q_2^{-1})$	White and Pohl (1995)
Ohmic	$\frac{(C'V)^2}{\pi k C}\left(\frac{\omega_0\tau}{1+(\omega_0\tau)^2}\right)$	
Magnetomotive	$\frac{L^2B^2\alpha}{m\omega_0^2 R}$	Cleland and Roukes (1999)
Thermoelastic effect	$\frac{\alpha^2 TE}{C}\left(\frac{\omega_0\tau}{1+(\omega_0\tau)^2}\right)$	Lifshitz and Roukes (2000)
Electron-phonon interactions	$\frac{8}{15}\frac{E_F m_e \sigma \omega_0}{\rho v^2 e^2}$	Braginsky et al. (1985)

Mass sensing

Mass sensors operate by measuring the frequency shift of the resonance as additional mass is adsorbed on the oscillator. Recalling Eq. 2.7 for the resonant frequency of a simple harmonic oscillator, we determine that the mass sensitivity δm is given by

$$\delta m = \frac{\partial m_{\text{eff}}}{\partial \omega_0} \delta\omega_0 = 2m_{\text{eff}} \frac{\delta\omega_0}{\omega_0} \tag{2.70}$$

Thus we see that the mass sensitivity is effectively determined by the effective mass of the oscillator and the frequency resolution. The frequency resolution is given roughly by the quality factor, even though typically the sensitivity is much better. The smallest detectable mass is then

$$\delta m = \frac{2m_{\text{eff}}}{Q} \tag{2.71}$$

In recent experiments (Ilic et al., 2004, Ekinci et al., 2004), mass sensitivities on the order of attograms (10^{-18}g) have been demonstrated.

Force sensing

Force sensing is used in several different techniques such as Magnetic Resonant Force Microscopy (MRFM), Electric Force Microscopy (EFM), and others. These applications use NEMS, typically in cantilever geometries as scanning probes sensitive to some kind of interaction (i.e. magnetic or electric forces), to obtain spatial information about the interaction in question. Recently, an ultrasoft cantilever was used to measure the force from a single spin(Rugar et al., 2004).

There are many sources of noise that limit the sensitivity of the measurement. For a complete survey of various noise mechanisms and their respective sensitivities see Cleland et al. (2002). The ultimate limit to force sensing is given by the thermal

vibrations of the cantilever. The spectral thermal density is given by

$$S_{\text{thermal}} = \sqrt{\frac{4k_{\text{B}}kT}{\omega_0 Q}} \tag{2.72}$$

where k is the spring constant of the cantilever, k_{B} is the Boltzman constant, T is the temperature, ω_0 is the resonant frequency, and Q is the quality factor.

2.8 Conclusions

In this chapter we have described the various aspects of nano-electro-mechanical systems. We have discussed the theory of linear and nonlinear oscillators, and have applied it to to calculate the resonant frequency of a cantilever beam and a double clamped beam system. We gave a discussion of the possible losses in NEMS that lead to the relatively low (compared with MEMS) quality factor. We also described the various actuation and detection techniques that are used to study NEMS and described two possible application for NEMS. We see that the sensitivities for both of the applications increase with decreasing effective mass, increasing vibrational frequency, and decreasing spring constant of the resonator. The combination of both high frequency and a soft resonator is, however, hard to realize. Two pathways have been taken to achieve this goal. The first is to measure higher harmonics of the fundamental vibrational modes, and the second is to build lighter resonators.

An ultimate solution to this is a carbon nanotube: it is an extremely light material with a high elastic modulus, promising light, but high frequency, mechanical resonators. Since CNTs have very few structural defects and have nicely terminated surfaces, we can expect from the arguments in section 2.6 that CNT resonators may have very high quality factors. Such reasoning motivates us to build a mechanical resonator based on carbon nanotube.

CHAPTER 3

DEVICE FABRICATION AND MEASUREMENT SETUP

3.1 Introduction

Because nanotubes are extremely small in cross section, it is difficult to realize a nanotube-based resonator with conventional actuation and detection methods (section 2.5) such as optical and magneto-motive techniques. Despite these challenges, a nanotube-based resonator in a cantilever geometry has been realized by several groups (Poncharal et al., 1999, Gao et al., 2000, Purcell et al., 2002). In this chapter we describe our method for electrically actuating and detecting the mechanical motion of a doubly clamped nanotube resonator (Sazonova et al., 2004). We discuss in detail the device fabrication (Section 3.2), actuation and detection techniques (Sections 3.3,and 3.4), and the details of the measurement setup (3.5, and 3.6).

3.2 Device fabrication

The samples studied in the thesis consist of suspended carbon nanotubes in a transistor geometry (Fig. 3.1). We contact the CNT with two metal electrodes and use the Si substrate separated from the CNT by an oxide layer as a gate electrode. The CNT is either partially or fully suspended across a trench in silicon dioxide. There are three major parts in fabrication: 1) growing tubes, 2) making electrical contacts and 3) suspending the CNT. We outline the fabrication steps below (see Fig. 3.2).

First, alumina supported FeO_3/MoO_2 catalyst pads are patterned using photolithography onto a degenerately-doped Si wafer with 500nm of surface oxide. The

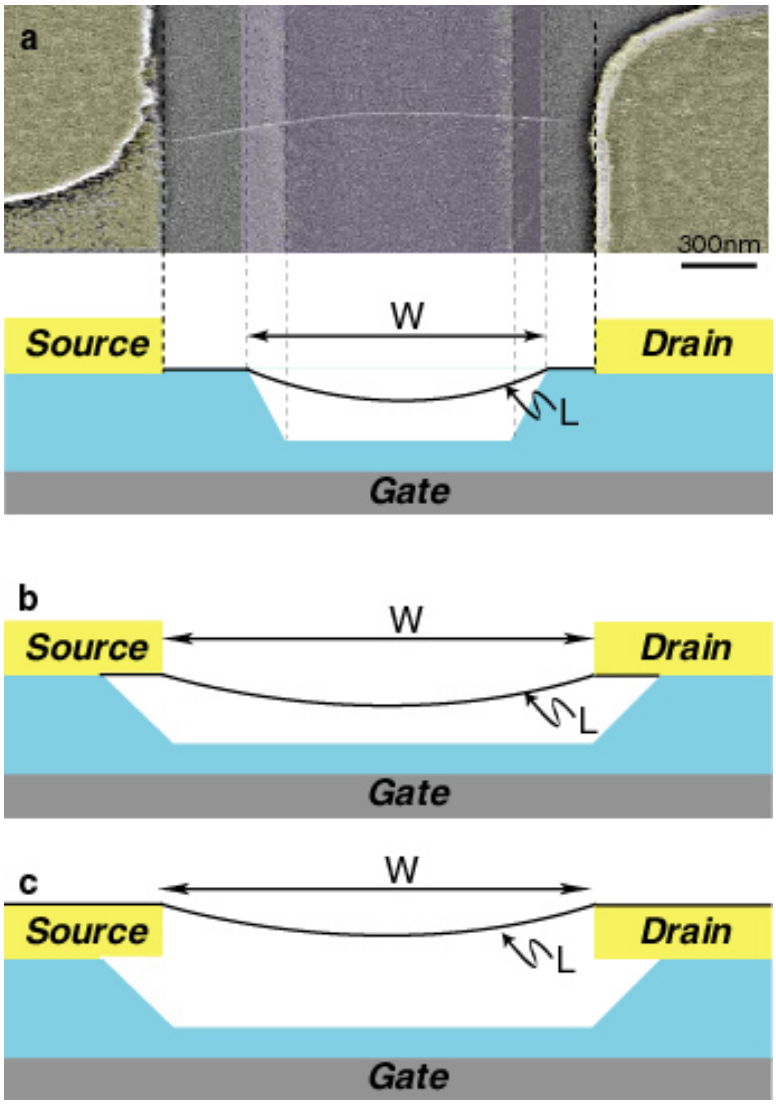

Figure 3.1: Device geometry schematic. **(a)** A false-colored SEM image of a suspended device taken at a 45° angle. Scale bar is 300nm. Metal electrodes (Au/Cr) are shown in yellow, and the silicon oxide surface in grey. A schematic of a device created with method #1. The sides of the trench, typically 1.2μm wide and 400nm deep, are marked with the dashed lines in the SEM images. A suspended nanotube can be seen bridging the trench. **(b)** A schematic of a device created with method #2. Typical gaps are 2μm. **(c)** A schematic of a device created with method #3. Typical gaps are $2-3\mu$m.

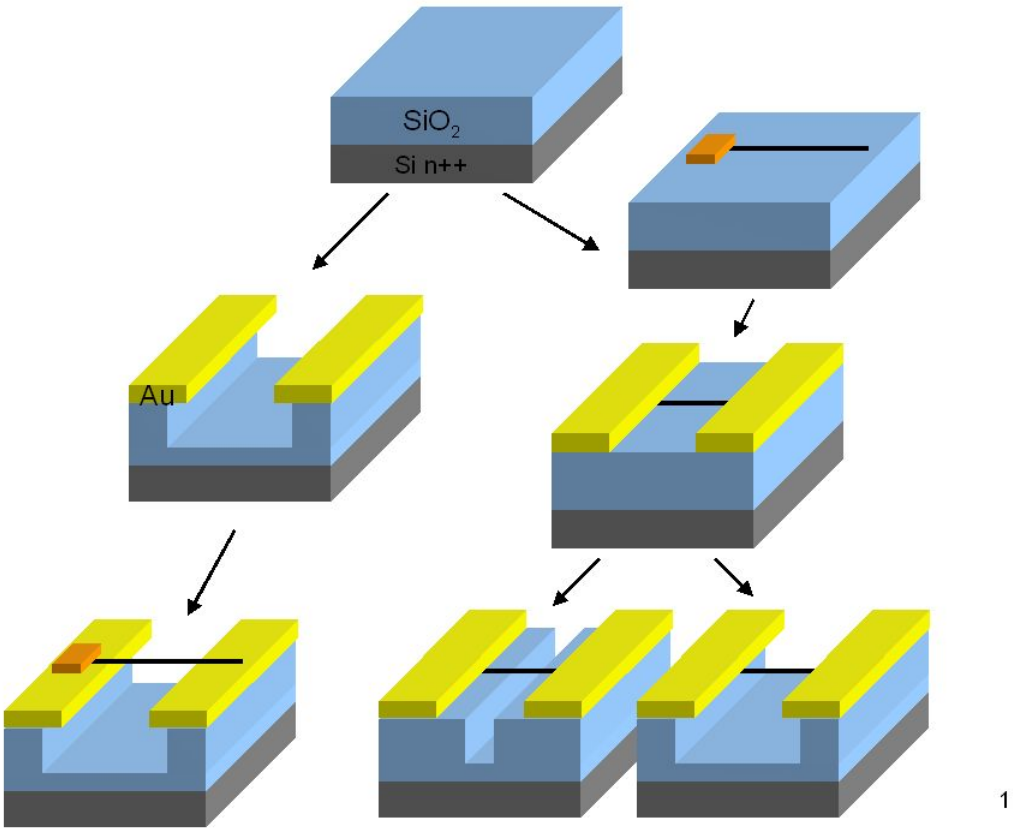

Figure 3.2: Fabrication steps. Catalyst pads are patterned onto a Si/SiO_2 wafer. CNTs are grown using CVD methods. After growth, electrodes are defined on top of the catalyst pads, and a Au/Cr layer is evaporated. A wet-etch step in buffered oxide followed by a critical point drying step is then performed to suspend the CNT. The etched portion of oxide is defined by either using the contacts as a mask or by lithographically defining a thin trench in between the contacts. Alternatively, a CNT can be grown last, on top of the deposited Pt contacts over a predefined trench in the oxide.

wafer is then placed into a chemical vapor deposition (CVD) (Kong et al., 1998) furnace at 900°C with a constant flow of methane to grow the tubes. After growth, electrodes with typical gaps of $2-3\mu$m are defined photolithographically (Rosenblatt et al., 2002) along with the electron beam lithography alignment marks on top of the catalyst pad. A metal layer is then evaporated, typically $50-80$nm of Au with a 5nm Cr adhesion layer, to contact the NTs. To suspend the CNT we perform a wet etching step in buffered oxide etch (BOE 6:1, nominal etch rate 80nm/min) (Walters et al., 1999, Nygard and Cobden, 2001). There are two different ways to define the etched portion of the oxide. In method #1 we use PMMA resist as a mask and define a thin ($100-300$nm wide) line between the electrodes by e-beam lithography to be etched. In method #2 we use the electrodes as an etching mask. After etching, a critical point drying step is performed to prevent the CNT from sticking to the substrate. A final step is annealing in the furnace at $400°\text{C}-600°\text{C}$ with Ar gas flow. Alternatively, in method #3, we can reverse the order of the steps. We first define the trenches in silicon oxide by either of the two techniques describes above, then define Pt electrodes, typically 50nm, then define a catalyst pad on top of the electrodes, and grow nanotubes across the trench (Cao et al., 2005).

With these methods we typically obtain devices that contain one or a few nanotubes. The diameters are $1-4$nm, which is typical for CVD growth (Kong et al., 1998). Typical resistances of our samples range between 30kΩ and 1MΩ. Similar devices with better conductances have been reported in the literature (Javey et al., 2003). However, these devices are typically made without an adhesion Cr layer, which for our suspended-nanotube devices is essential. Without the adhesion layer, the Au lifts off from the substrate during the etching step. In order to improve

the conductances in our devices we resort to an annealing step. This process is essentially an "ashing" procedure that improves the contact resistance and cleans the surface from the residues of processing (Rosenblatt et al., 2002).

A false-colored SEM picture of a typical final device suspended with method #1 and its schematic can be seen in Fig. 3.1a. We see a nanotube suspended over a trench bridging source and drain electrodes. The apparent buckling of the CNT is a real effect. It is due to CNT curvature prior to suspension which results in the CNT being longer than the width of the trench. The downward direction of the buckling is set by the electric field from the gate electrode. In principle, in the absence of an electric field this direction is arbitrary, as the gravitation force of the nanotube is negligible.

The dimensions of the trench are $\sim 1.2\mu$m wide by 400nm deep. Note that the resulting trench is much wider than defined by e-beam lithography. This increase of the width of the trench is due to the isotropic etching of BOE. After etching the trench increases by twice its depth. Since the width of the trench is still smaller than the distance between the electrodes, a small section of the tube resides on the oxide. CNTs are known to adhere well to silicon oxide (Hertel et al., 1998) and so we assume that this adhesion ensures good clamping. This existence of the non-suspended portion of the CNT enables us to take atomic force microscopy (AFM) images of the tube and determine its diameter. An example of an AFM image can be seen in Fig. 3.3b. The suspended part of the tube appears fuzzy on the image as it is free to move around and thus interacts with the AFM tip at different positions; the non-suspended part of the tube appears as a line of constant height on the image.

Figure 3.1b shows a schematic of a device in which the nanotube was suspended

with method #2. In this geometry all of the oxide between the electrodes is removed, and since the etch is isotropic, the electrodes develop an overhang as wide as the depth of the trench. The clamping in this case is provided by the tube-metal adhesion. It was found, in experiments on modifying the CNT band-structure by strain with similar devices, that the NT-metal clamping could withstand forces up to 20nN before the the tube was ripped out from the contacts (Minot et al., 2003).

Figure 3.1c shows a schematic of a device in which the nanotube was suspended with method #3. In this geometry all of the oxide between the electrodes is removed by either the a wet etch or a dry etch. The nanotube is grown on top of the contacts and the clamping in this case is provided by the tube-metal adhesion (Cao et al., 2005).

Unfortunately, imaging devices with SEM and AFM can be destructive to the sample. We found that SEM causes a substantial decrease in the conductance of a device. We do not understand the origins of this effect. Some brief discussion is provided in Appendix B. Taking AFM images of suspended device may also be destructive to the sample. Since the CNT sticks briefly to the AFM tip during the scan, imaging perpendicularly to the direction of growth can break the nanotube. Even when imaging parallel to the CNT one must exercise caution in choosing the speed and overall area of the scan. We found that scan areas of 3μm squares taken at rates of 1Hz or less work fairly well. When moving from one area to another one needs to ensure that in this translational move the AFM tip does not go over a suspended nanotube. So even though AFM imaging is possible, it must be used with caution. Because of these concerns we did not image any of the studied devices.

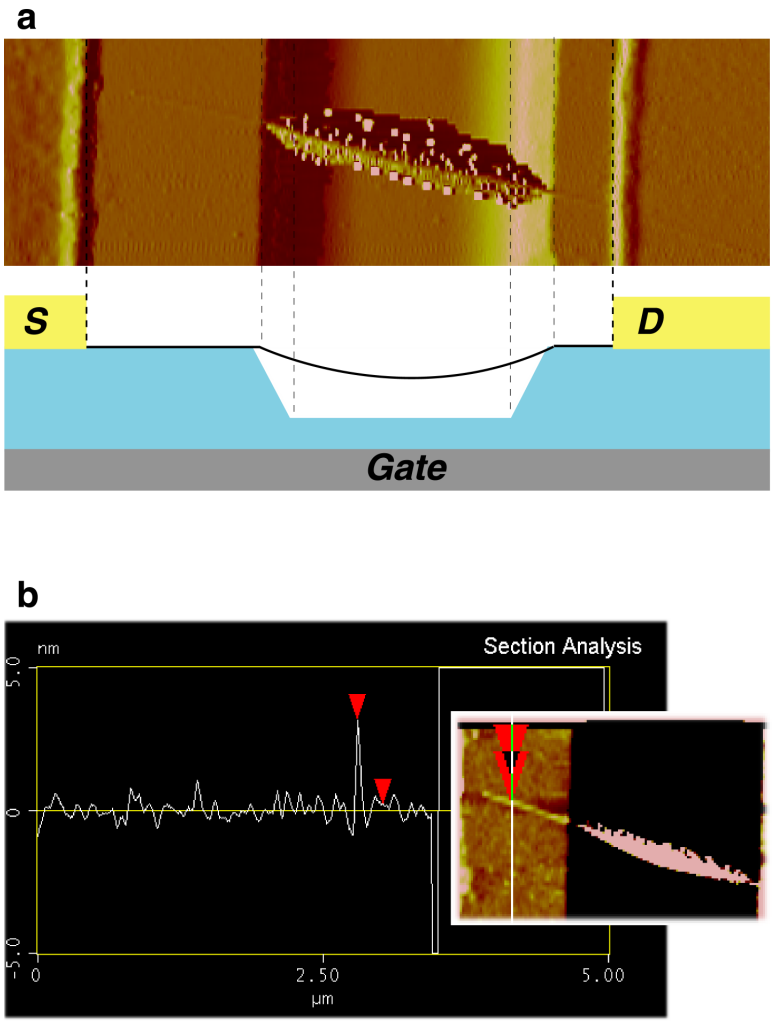

Figure 3.3: **(a)** AFM image of suspended nanotube device. The sides of the trench are marked with the dashed lines. **(b)** An AFM tip height trace across a non-suspended portion of the nanotube. The red triangular markers indicated the position of the CNT and the oxide along the trace. The height difference between the markers is 2.9nm - the diameter of the tube.

3.3 Actuation Technique

We actuate the nanotube motion using the electrostatic interaction with the gate electrode underneath the tube (see Fig. 3.4a). A gate voltage $V_{\rm g}$ induces an additional charge on the CNT given by $q = C_{\rm g}V_{\rm g}$, where $C_{\rm g}$ is the capacitance to the gate. The attraction between the charge q and its opposite charge $-q$ on the gate causes an electrostatic force downward on the CNT. If $C'_{\rm g} = dC_{\rm g}/dz$ is the derivative of the gate capacitance with respect to the distance between the tube and the gate, the total electrostatic force on the tube is

$$F_{\rm el} = \frac{1}{2}C'_{\rm g}V_{\rm g}^2 \tag{3.1}$$

If the gate voltage is modulated at some driving frequency ω,

$$V_{\rm g} = V_{\rm g}^{\rm DC} + \underbrace{\tilde{V}_{\rm g}\cos(\omega t)}_{\tilde{V}_{\rm g}^{\omega}} \tag{3.2}$$

The total electrostatic force on the tube is

$$F_{\rm el} \cong \frac{1}{2}C'_{\rm g}V_{\rm g}^{DC}(V_{\rm g}^{DC} + 2\tilde{V}_{\rm g}^{\omega}) \tag{3.3}$$

where we have neglected the term proportional to ${\tilde{V}_{\rm g}^{\omega}}^2$.

We see that $F_{\rm el}$ has two parts: the DC term controlled by the DC voltage $V_{\rm g}^{\rm DC}$ and the AC term produces by the AC component of the gate voltage $\tilde{V}_{\rm g}^{\omega}$.

$$\begin{aligned} F_{\rm el}^{\rm DC} &= \tfrac{1}{2}C'_{\rm g}\,{V_{\rm g}^{DC}}^2 \\ \tilde{F}_{\rm el} &\cong C'_{\rm g}V_{\rm g}^{DC}\tilde{V}_{\rm g}^{\omega} \end{aligned} \tag{3.4}$$

The DC term is used to control NT's tension, and the AC term sets the CNT into motion. As the driving frequency ω approaches the resonance frequency ω_0 the displacements become large (see section 2.2).

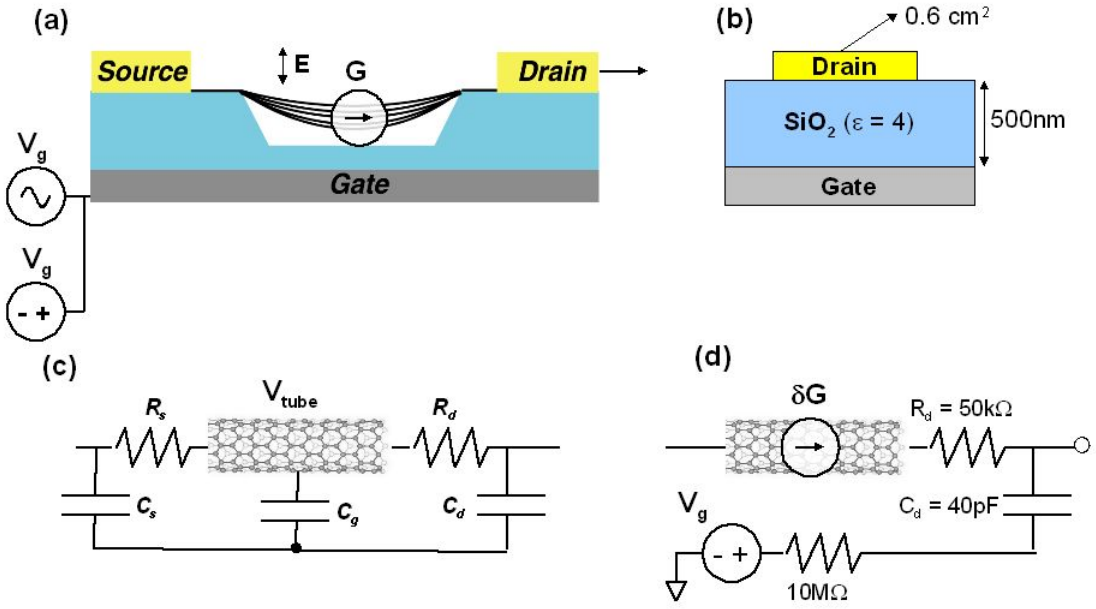

Figure 3.4: An equivalent circuit diagram for a CNT device. **(a)** A schematic of the actuation and detection methods. DC and AC voltages are applied to the gate electrode to excite the vibration. On resonance the CNT is a source of the AC conductance modulation. **(b)** A schematic of the contact pad - gate capacitor. **(c)** An equivalent circuit for a CNT device. The CNT is approximated as a ballistic conductor in series with two contact resistors. **(d)** The equivalent circuit for calculating the output bandwidth of a NT.

3.4 Detection technique

To detect the motion of the nanotube on resonance we rely on the NTs transistor properties. For semiconducting (Tans et al., 1998) and small band-gap semiconducting carbon nanotubes (Zhou et al., 2000, Minot et al., 2004) the conductance depends on the induced charge on the tube. A modulation in the charge, $\tilde{q}$, then leads to a modulation in the CNT's conductance $\tilde{G} = \frac{dG}{dq}\tilde{q}$. The conductance can be modulated by changing either the applied gate voltage or capacitance to the gate.

$$\tilde{q} = \tilde{C}_{\mathrm{g}}(\omega)V_{\mathrm{g}}^{\mathrm{DC}} + C_{\mathrm{g}}\,\tilde{V}_{\mathrm{g}}^{\omega} \tag{3.5}$$

where we have again assumed that the modulation is small and neglected the cross term.

If Z is the distance between the tube and the gate, Z_0 is the initial distance, and $z(\omega)$ is the NT's amplitude of motion defined by Eq. 2.4, then in general:

$$Z(\omega) = Z_0 - z(\omega)\cos(\omega t) \tag{3.6}$$

Due to this motion the tube-gate capacitance is modulated at the frequency ω with the amplitude of

$$\tilde{C}_{\mathrm{g}}(\omega) = C'_{\mathrm{g}} z(\omega) \tag{3.7}$$

As described above, capacitance modulation leads to modulation of the induced charge

$$\tilde{q} = \tilde{C}_{\mathrm{g}}(\omega)V_{\mathrm{g}} = C'_{\mathrm{g}} z(\omega)V_{\mathrm{g}}^{\mathrm{DC}} \tag{3.8}$$

and to the conductance modulation given by

$$\tilde{G} = \frac{dG}{dq}\tilde{q} = \frac{dG}{dq}C'_{\mathrm{g}} z(\omega)V_{\mathrm{g}}^{\mathrm{DC}} \tag{3.9}$$

From Eq. 3.9 we see that conductance is modulated at the driving frequency, and is proportional to the NT's amplitude of motion. The maximum conductance modulation then occurs as the driving frequency approaches the resonance frequency (see Eq. 2.4). For our geometry that corresponds to frequencies in the tens of MHz range. Thus, to measure the conductance modulation directly (in real time), we would have to detect a small electrical signal at a high frequency out of a highly resistive device.

We can calculate the bandwidth of a CNT by approximating it as a ballistic conductor in series with two contact resistors and assuming that stray capacitances come mostly from the contact pad - gate leakage (see Fig. 3.4c). A typical device has resistance on the order of $R_{\text{tube}} = 100\text{k}\Omega$. Assuming symmetric contacts, each contact resistance is $R_{\text{s}} = R_{\text{d}} = 50\text{k}\Omega$. To calculate the contribution to stray capacitance from each contact pad, C_{s} and C_{d}, we use a parallel plate capacitor model (see Fig. 3.4b).

$$C = \frac{\epsilon_0 \epsilon A}{d} \tag{3.10}$$

where ϵ is the dielectric constant of SiO_2, A is the area of the contact pad, and d is the thickness of the oxide layer. For the contact pad dimensions in our devices (illustrated for drain electrode in Fig. 3.4b) we estimate $C_{\text{s}} = 6\text{pF}$, and $C_{\text{d}} = 40\text{pF}$. The equivalent circuit for detecting high frequency signals out of the CNT is shown in Fig. 3.4d. Approximating the circuit by a low-pass filter, we calculate that the corner frequency for this setup is given by

$$f_{\text{corner}} = \frac{1}{2\pi R_{\text{d}} C_{\text{d}}} \approx 100\text{kHz} \tag{3.11}$$

Such low readout bandwidth of the device prevents us from a direct (real time) measurement of the conductance modulation on resonance.

3.5 Mixing circuit

Two different methods have been previously employed to solve this problem in case of small electronic devices (Schoelkopf et al., 1998, Knobel and Cleland, 2003). If the desired detection frequency (CNT resonance frequency in our case) is known, a matching circuit that transforms the impedance of the device to 50Ω at the desired frequency can be built (Hagen, 1996, Schoelkopf et al., 1998). Alternatively the signal can be mixed down to frequencies below the cutoff of the device (Hagen, 1996, Knobel and Cleland, 2003, Bargatin et al., 2005). Both approaches have been successfully used with NEMS. As the resonance frequency in our case is not known a priori, we have chosen the second approach.

We employ the nonlinearity in the current-gate voltage dependence in our devices (the non-zero transconductance dG/dV_{g}) to use the CNT as a mixer. The detailed theory of mixing with transistors in general, and CNTs in particular is given in Rosenblatt (2005). Here we give a simplified introduction to theory of mixing with NTs.

In general if the CNT conductance, G, is modulated at a some frequency ω as

$$G = G^{\mathrm{DC}} + \underbrace{\tilde{G}\cos(\omega t)}_{\tilde{G}^{\omega}} \tag{3.12}$$

and we apply a local oscillator (LO) signal to the source electrode at a slightly offset frequency $\omega + \Delta\omega$

$$\tilde{V}_{\mathrm{sd}}^{\omega+\Delta\omega} = \underbrace{\tilde{V}_{\mathrm{sd}}\cos((\omega+\Delta\omega)t)}_{\tilde{V}_{\mathrm{sd}}^{\omega+\Delta\omega}} \tag{3.13}$$

The current, I, through the nanotube will have both frequency components, since it depends on the source-drain voltage and the conductance of the CNT. Using

equations 3.12,and 3.13 we get that

$$\begin{aligned} I &= GV_{\rm sd} = (G^{\rm DC} + \tilde{G}^{\omega})(\tilde{V}_{\rm sd}^{\omega+\Delta\omega}) \\ &= G^{\rm DC}\tilde{V}_{\rm sd}^{\omega+\Delta\omega} + \tilde{G}^{\omega}\tilde{V}_{\rm sd}^{\omega+\Delta\omega} \end{aligned} \tag{3.14}$$

The first term describes the current at the LO frequency. The second term, though, is more interesting – it consists of the the product of two AC signals and is the term that is responsible for the mixing. If we expand the last term using Eqs. 3.12 and 3.13, we get

$$\begin{aligned} \tilde{G}^{\omega}\tilde{V}_{\rm sd}^{\omega+\Delta\omega} &= \tilde{G}\cos(\omega t)\tilde{V}_{\rm sd}\cos((\omega+\Delta\omega)t) \\ &= \tilde{G}\tilde{V}_{\rm sd}\frac{1}{2}\left(\cos(2\omega t) + \cos(\Delta\omega t)\right) \end{aligned} \tag{3.15}$$

which means that the amplitude of the current through the nanotube, $I^{\Delta\omega}$, at the intermediate frequency $\Delta\omega$, is equal to

$$I^{\Delta\omega} = \frac{1}{2}\tilde{G}\tilde{V}_{\rm sd} \tag{3.16}$$

and is proportional to the conductance change of the nanotube. Using Eqs. 3.5 and 3.9 we finally derive that the total current is

$$I^{\Delta\omega} = \frac{1}{2}\frac{dG}{dq}\left(C_{\rm g}' z(\omega) V_{\rm g}^{\rm DC} + C_{\rm g}\,\tilde{V}_{\rm g}\right)\tilde{V}_{\rm sd} \tag{3.17}$$

Since we can make the intermediate frequency $\Delta\omega$ arbitrary small, this technique enables us to measure the amplitude of high frequency conductance modulations of the nanotube by measuring the current through it at frequencies that are within the readout bandwidth.

3.6 Measurement setup

The measurements were performed inside a Desert Cryogenics variable temperature vacuum probe station at pressures of 10^{-5} torr or less. The sample is placed onto

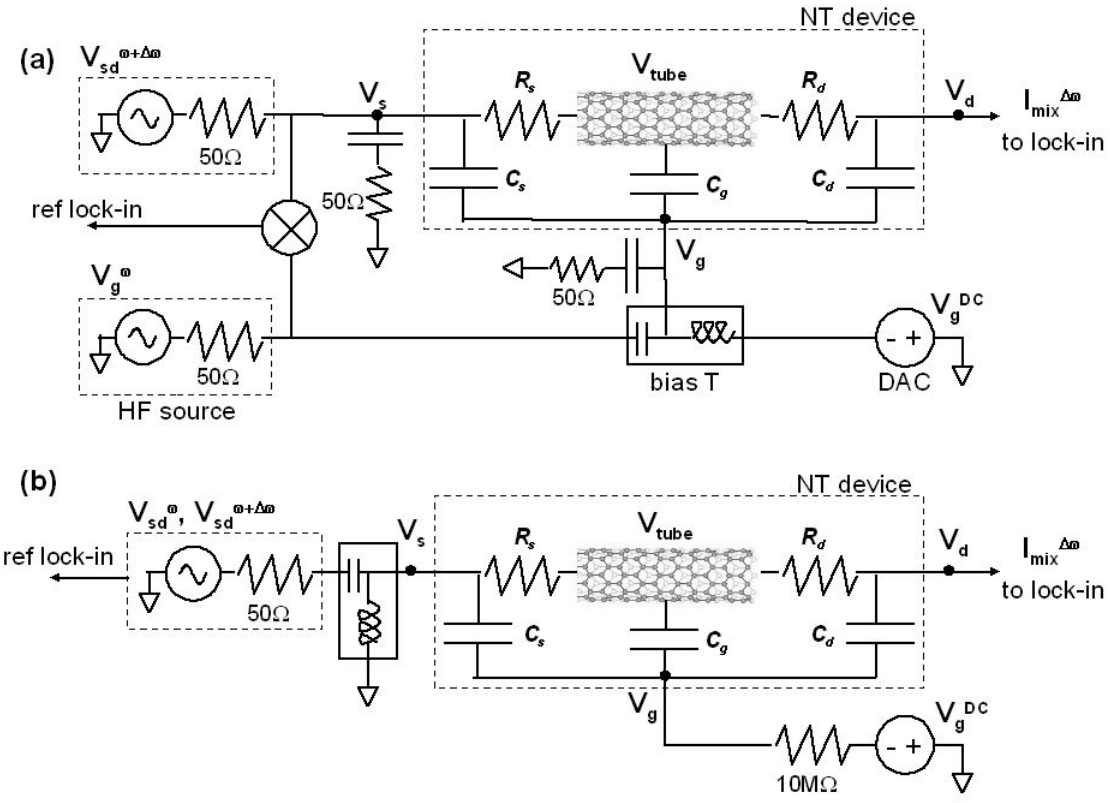

Figure 3.5: Schematics of the experimental setups. **(a)** Two-source setup. A local oscillator voltage $\tilde{V}_{\rm sd}^{\omega+\Delta\omega}$ (usually around 7mV) is applied to the source electrode at a frequency offset from the gate voltage signal $\tilde{V}_{\rm g}^{\omega}$ by an intermediate frequency $\Delta\omega$ of 10kHz. The current from the nanotube is detected by a lock-in amplifier, at $\Delta\omega$. **(b)** One-source setup. An AM modulated high frequency voltage $\tilde{V}_{\rm sd}^{\omega}$ (usually between $3-10$mV) is applied to the source electrode in the presence of a static electric field provided by the DC gate voltage $V_{\rm g}^{\rm DC}$. The current from the nanotube is detected by a lock-in amplifier, at $\Delta\omega$ – the AM modulation frequency (1kHz or 400Hz).

a sample stage which is thermally coupled to the reservoir through which the liquid ^{4}He can be pumped. The temperature is controlled by monitoring resistive thermometers at the sample stage, and by use of the resistive heaters on the stage. For electrical measurements the sample is contacted with metallic probes capable of delivering signals at frequencies up to 2GHz. 50Ω resistors in series with 10nF capacitors were soldered into the probes to minimize circuit resonance by matching the impedance of a line near the sample. The capacitors were introduced to allow for DC measurements as well, and were chosen such that their presence would not affect the impedance in the frequency range of interest.

Two different electrical setups were used; the first we label the "two sources" setup, and the second is called the "one source" setup. The complete circuit diagram for both of the setups can be seen in Fig. 3.5. Both of the setups employ the capacitive detection method with the mixing technique described in the previous section, differing only in how the modulation of the gate voltage is achieved.

Two sources setup

In the "two sources" setup the high frequency signals on the gate electrode (for driving the resonator) and on the source electrode (for mixing) are applied from two different high frequency sources: HP87332A (10MHz − 40GHz), and HP8657A (0.1MHz − 1040MHz). The DC voltage on the gate is provided by a computer controlled digital-to-analog card, which is connected to the gate electrode through a bias-T. The current through the nanotube is detected by a DC-coupled Stanford lock-in amplifier(SR830) in the current mode. The reference signal to the lock-in amplifier is provided by separately mixing the two high frequency signals used for gate and source electrode with an external mixer (Minicircuits ZLW-1SH).

The reference input lock-in amplifier serves as the low-pass filter with the corner frequency of 100kHz so no additional low-pass filter is necessary to eliminate the high-frequency components from mixer.

In this setup the voltages on the gate, source and drain electrodes are:

$$\begin{aligned} V_{\mathrm{g}} &= V_{\mathrm{g}}^{\mathrm{DC}} + \tilde{V}_{\mathrm{g}} \cos(\omega t) \\ V_{\mathrm{s}} &= \tilde{V}_{\mathrm{sd}} \cos((\omega + \Delta\omega)t + \phi) \\ V_{\mathrm{d}} &= 0 \end{aligned} \tag{3.18}$$

where ω, $\Delta\omega$, and ϕ are the current driving frequency, lock-in readout frequency and the gate-source phase difference, respectively.

By looking at the circuit diagram (Fig. 3.5a) we see that the potential of the tube, V_{tube}, is given by

$$V_{\mathrm{tube}} = (V_{\mathrm{s}} - V_{\mathrm{d}}) \frac{R_{\mathrm{d}}}{R_{\mathrm{s}} + R_{\mathrm{d}}} \tag{3.19}$$

which for the contacts of equal resistance reduces to $\frac{1}{2}V_{\mathrm{s}}$. For the "two sources" setup the potential of the tube is then

$$V_{\mathrm{tube}} = \frac{1}{2}\tilde{V}_{\mathrm{sd}} \cos((\omega + \Delta\omega)t + \phi) \tag{3.20}$$

The effective gate voltage, $V_{\mathrm{g}}^{\mathrm{eff}}$, that the tube feels is given by the voltage on the gate with respect to the potential of the tube, $V_{\mathrm{g}} - V_{\mathrm{tube}}$. Using the above equations we find that the effective gate voltage is

$$V_{\mathrm{g}}^{\mathrm{eff}} = V_{\mathrm{g}}^{\mathrm{DC}} + \tilde{V}_{\mathrm{g}} \cos(\omega t) - \frac{1}{2}\tilde{V}_{\mathrm{sd}} \cos((\omega + \Delta\omega)t + \phi) \tag{3.21}$$

Even though the effective gate voltage and thus the induced charge and CNT conductance contain an additional component at $\omega + \Delta\omega$, the amplitude of mixing current detected at $\Delta\omega$ given in Eq. 3.17 is not affected.

Amplitude modulation

Before we explain the configuration for the second setup let us note that the effect of the source-drain voltage on the potential of the tube described above provides an alternative way to achieve modulation of the gate. Even in the absence of any AC signal applied to the gate, by preceding arguments the effective gate is modulated as

$$V_{\rm g}^{\rm eff} = V_{\rm g}^{\rm DC} - \frac{1}{2}\tilde{V}_{\rm sd}^{\omega} \tag{3.22}$$

Then in principle both of the signals, the driving excitation $\tilde{V}_{\rm sd}^{\omega}$ and the mixing excitation $\tilde{V}_{\rm sd}^{\omega+\Delta\omega}$, can be applied to the source electrode. This greatly simplifies the circuit because we can produce both of them with one high frequency source, using the source's amplitude modulation (AM) capabilities.

AM modulation at frequency $\Delta\omega$ with strength m for an arbitrary signal $A\cos(\omega t)$ is defined as

$$\begin{aligned} V_{\rm AM} &= (1 + m\cos(\Delta\omega t))A\cos(\omega t) \\ &= A\cos(\omega t) + \frac{Am}{2}\left(\cos((\omega+\Delta\omega)t) + \cos((\omega-\Delta\omega)t)\right) \end{aligned} \tag{3.23}$$

So an AM modulated signal is equivalent to three high frequency signals offset by the modulation frequency. In the language of the "two source" setup the driving excitation and the mixing excitation are then equal to

$$\tilde{V}_{\rm g}^{\omega} = \tilde{V}_{\rm sd}\cos(\omega t) \tag{3.24}$$

$$\tilde{V}_{\rm sd}^{\omega+\Delta\omega} = \tilde{V}_{\rm sd}\frac{m}{2}\cos((\omega+\Delta\omega)t) \tag{3.25}$$

$$\tilde{V}_{\rm sd}^{\omega-\Delta\omega} = \tilde{V}_{\rm sd}\frac{m}{2}\cos((\omega-\Delta\omega)t) \tag{3.26}$$

Both $\tilde{V}_{\rm sd}^{\omega+\Delta\omega}$ and $\tilde{V}_{\rm sd}^{\omega-\Delta\omega}$ will mix with $\tilde{V}_{\rm g}^{\omega}$, producing a signal of the same phase and magnitude. Thus for the purposes of mixing this situation is equivalent to

having the following

$$\tilde{V}_{\mathrm{g}}^{\omega} = \tilde{V}_{\mathrm{sd}} \cos(\omega t) \tag{3.27}$$

$$\tilde{V}_{\mathrm{sd}}^{\omega+\Delta\omega} = \tilde{V}_{\mathrm{sd}} m \cos((\omega + \Delta\omega)t) \tag{3.28}$$

One source setup

The setup for the "one source" technique is then as follows. One AM-enabled high frequency source (HP8657A) is connected to the source electrode of the device and provides the two signals necessary for both driving the resonator and mixing down the response. The DC gate voltage is supplied by the computer-enabled digital to analog card just as in the previous setup, which in this case is connected directly to the gate electrode. The current through the device is still measured by the dc-coupled Stanford lock-in amplifier in the current mode, with the reference signal provided by the reference to the AM modulation. The typical modulation strengths used throughout this thesis are $m = 99\%$.

In this setup the voltages on the gate, source, and drain electrodes are:

$$\begin{aligned} V_{\mathrm{g}} &= V_{\mathrm{g}}^{\mathrm{DC}} \\ V_{\mathrm{s}} &= \tilde{V}_{\mathrm{sd}}(\cos(\omega t) + \tfrac{0.99}{2}(\cos((\omega + \Delta\omega)t + \phi) + \cos((\omega - \Delta\omega)t + \phi))) \\ V_{\mathrm{d}} &= 0 \end{aligned} \tag{3.29}$$

In principle this technique can be used with the intermediate frequency set to zero, $\Delta\omega = 0$, which eliminates the need for the lock-in amplifier, the two HF sources, or the AM modulation, as the same signal can be used for both, driving and mixing (Rosenblatt et al., 2005). However there are a few complications in using this DC method. First and most noticeable is the fact the any current amplifier used to detect the current will always produce a back DC voltage that needs to be zeroed out in order to distinguish the mixed signal from the "normal" current

due to this amplifier voltage. This voltage changes any time the circuit is modified so that the current amplifier has to be constantly readjusted. The second, more concerning problem is that the noise level with a DC readout technique is much higher than at 1kHz due to $1/f$ noise. Thus for the purpose of this experiment we have decided to use the non-zero intermediate frequency method, with a frequency of 1kHz.

3.7 Mixing from a nonsuspended device

Before performing any measurement on a nanotube resonator, we would like to test and calibrate the setup. Using a non-suspended device for this purpose turns out to be extremely useful. We start by discussing what signals we expect from such a device.

Let us go back to Eq. 3.17 which describes the expected mixing current through a CNT. For convenience we reproduce it here.

$$I^{\Delta\omega} = \frac{1}{2}\frac{dG}{dq}\left(C_{\rm g}' z(\omega) V_{\rm g}^{\rm DC} + C_{\rm g}\tilde{V}_{\rm g}\right)\tilde{V}_{\rm sd} \tag{3.30}$$

The first term is described in section 3.4 and for a case of a non-suspended device is zero, as $z(\omega) = 0$ at all ω. The second term is due to the second term in Eq. 3.5, the gate voltage modulation. This term is frequency independent, of purely electrical origin, and is present whether the device is suspended or not. The mixing current through a non-suspended device is then just due to the second term.

We expect the mixing current to be proportional to the transconductance $\frac{dG}{dq}$ of the nanotube. We can independently measure the transconductance of the nanotube by measuring its DC conductance and using the fact that in the non-vibrating state, $\tilde{q} = C_{\rm g}\tilde{V}_{\rm g}$. Thus, the transconductance can be extracted from the

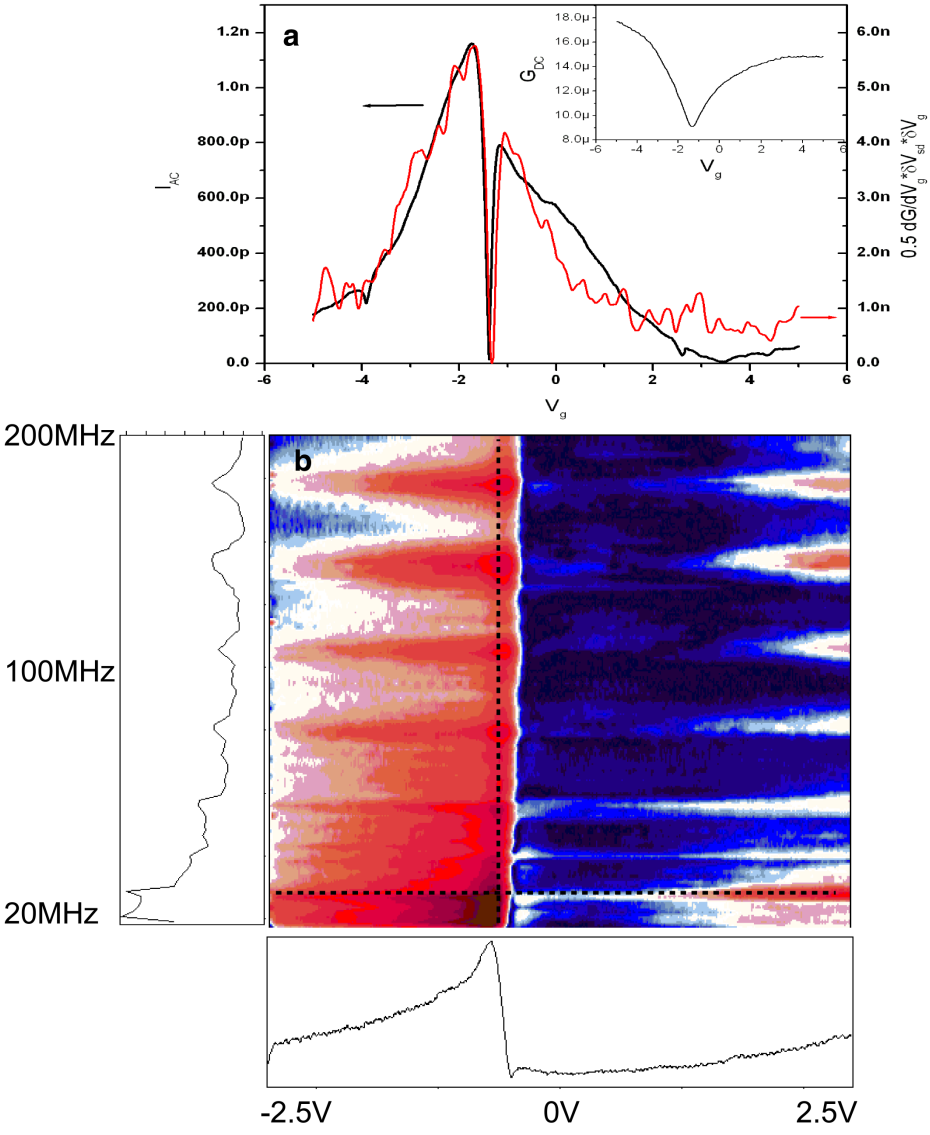

Figure 3.6: **(a)** Mixing signal and the predicted signal from the transconductance of the device. **(b)** Mixing current (in color) as a function of the gate voltage and driving frequency. Cuts through the data set at $V_g = -0.5$V and $f = 25$MHz are marked with dash lines.

DC current as

$$\frac{dG}{dq} = \frac{dG^{\mathrm{DC}}}{dV_{\mathrm{g}}}\frac{1}{C_{\mathrm{g}}} \tag{3.31}$$

The amplitude of the total expected current through a non-suspended device is then given by

$$I^{\Delta\omega} = \frac{1}{2}\frac{dG^{\mathrm{DC}}}{dV_{\mathrm{g}}}\tilde{V}_{\mathrm{g}}\tilde{V}_{\mathrm{sd}} \tag{3.32}$$

Fig 3.6a shows a comparison of measured mixing current and the predicted current from a numerical derivative of the NTs conductance (inset) for a non-suspended device. The shape of the signal agrees well, but the amplitude of the signal only reaches about 50% of the predicted value. We will return to possible sources of dissipation later in this section.

In order to explore this further we can measure the mixing current through the nanotube as a function of driving frequency. Fig 3.6b shows the mixing current in color as a function of both gate voltage and driving frequency. Figs 3.6c and d are cuts through b at constant gate voltage and frequency, respectively. There two things that we notice about this graph. First, there is an overall decay of the signal with increasing frequency, with the signal becoming unmeasurable at around 600MHz; and second, there are periodic oscillations superimposed on top of the signal with a periodicity of about 35MHz.

The overall decay of the signal can be attributed to capacitive leakage to the gate. The stray contact pad to gate capacitances provide an alternative route to ground at high frequencies. The circuit (Fig. 3.5) becomes equivalent to a low-pass filter with a resistance given by the source output impedance (50Ω) and a capacitance given by the equivalent capacitance of both pads in series. The corner

frequency for the voltage on the tube $V_{\rm s}$ is then given by

$$f = \frac{1}{2\pi(50\Omega)\frac{C_{\rm s}C_{\rm d}}{C_{\rm s}+C_{\rm d}}} \approx 650\text{MHz} \tag{3.33}$$

This agrees well with the observed decay of the signal. In other experiments on non-suspended CNT this problem has been resolved by introducing a local gate which increased the corner frequency to 50GHz (Rosenblatt et al., 2005).

Even though the input lines were 50Ω-terminated, as we see in Fig 3.6b, some circuit resonances are still present. We could not determine the origin of these remaining resonances, although the periodicity of the peaks in Fig. 3.6 suggests that the quarter wavelength of the circuit resonance is on the order of 2m which roughly corresponds to the length scale of the cables in the circuit. The exact pattern of this resonance varies from sample to sample and the strength can greatly increase if a bad contact is made with the probe.

3.8 Conclusions

In this chapter we discussed the fabrication of the suspended CNT devices and measurement setup for actuating and detecting the mechanical motion of a nanotube resonator. CNT devices in transistor geometry were fabricated using standard fabrication methods, and then suspended by wet etching. The motion of the resulting suspended CNT was actuated using capacitive forces between the CNT and the underlying gate electrode. The motion was detected by measuring changes in the CNT conductance due to modulations in tube-gate capacitance. As the output bandwidth of a CNT is too low to measure the conductance changes directly, a mixing scheme was devised. Two different measuring setups were devised to drive and detect the motion of the CNT. The setups were tested using a non-suspended

CNT device, which produces signals consistent with theoretical predictions. The mixing signal was found to decay due to electrode - gate capacitive coupling, and exhibited periodic resonance that we attributed to resonances in the circuit cables.

CHAPTER 4

TUNING THE FREQUENCY

4.1 Introduction

In this chapter we describe the first measurements of the nano-mechanical nanotube resonator (Sazonova et al., 2004) introduced in Chapter 3. In section 4.2 we describe the first observation of the mechanical resonance phenomena and the effect of the static gate voltage on this resonance. In section 4.3 we introduce a qualitative model for the nanotube resonator, which we develop further into a more quantitative analysis in section 4.4. We conclude this chapter by comparing the behavior of the observed resonances with the model (section 4.5) and discussing some of the behavior not described by the model (section 4.6).

4.2 Observing the resonance

Using the measurement procedure described in section 3.6, we can plot the drain mixing current measured by the lock-in as a function of the driving frequency. Figure 4.1 shows results for several different devices. We notice that each plot shows a distinct feature in the current on top of a slowly-changing background. Remembering the expression for the drain current (Eq. 3.17) from section 3.7, we attribute the slowly changing background to the mixing current due to the modulation of the gate voltage (similar to the the nonsuspended case). The sharp feature is due to to nanotube's mechanical motion on resonance, modulating the gate capacitance and thus producing an additional signal in the mixing current. We will discuss the details of the lineshape of this resonance and extract the important mechanical parameters for this resonator in the next chapter. We see a lot of

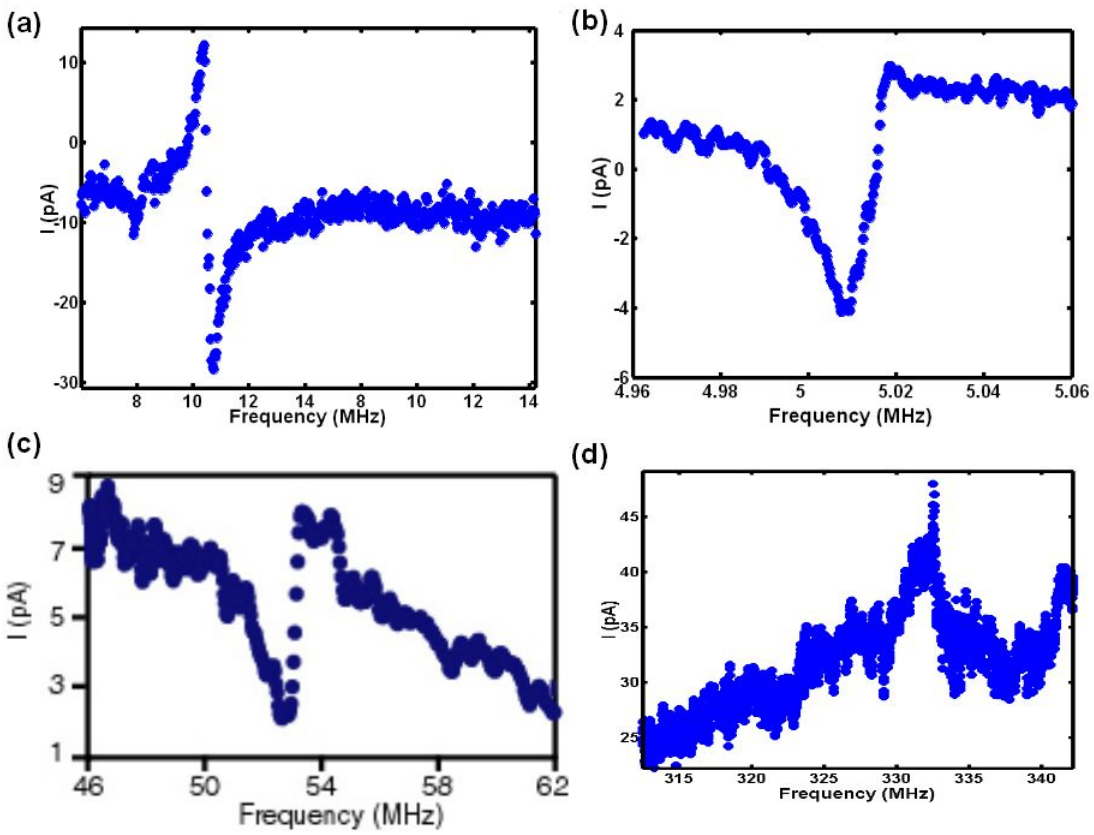

Figure 4.1: Observed resonances. Detected current as a function of driving frequency for four different devices. A sharp feature on top of a slowly changing background, present in all four graphs, is due to gate capacitance change from the CNT moving on resonance.

variation in the resonant frequencies of the measured resonances. In total we observed resonant frequencies in the $5\text{MHz} - 400\text{MHz}$ range among the 30 devices that exhibited resonance.

Before going into the quantitative analysis of this resonance we will study its behavior as the downwards DC force on the nanotube is changed. From Eq. 3.4 we know that the DC gate voltage controls the overall DC force on the nanotube and defines the tension in the nanotube. Thus, by varying the DC gate voltage we will effectively be changing the tension in the nanotube.

Figure 4.2 shows the traces of mixing current vs. frequency for several different gate voltages, for the same device as shown in Fig. 4.1a. For clarity, the curves are vertically offset. The position of the resonance changes as the gate voltage is adjusted. We can also fix the driving frequency, scan the DC gate voltage, and observe the resonance appear and disappear (Fig. 4.2b).

In order to determine the position of the resonance as a function of gate voltage we take a 3D scan of the mixing current as a function of both driving frequency and DC gate voltage, as shown in Figure 4.3. The measured current is presented in color-scale as a function of the driving frequency (y-axis) and the static gate voltage (x-axis). Overall the plot looks similar to the non-suspended case (Fig. 3.6); however, on top of the smoothly varying background we see several sharp lines indicated by arrows in Fig. 4.3. The lines indicate the occurrence of a sudden change in the drain mixing current, associated with the mechanical resonance in the nanotube. By extracting the position of these lines we can monitor the position of the NT's mechanical resonance in the gate voltage – frequency domain. We refer to the position of the resonance as a function of the gate voltage $f_0(V_g)$ as the "dispersion relation". For the rest of this chapter we will only be concerned with

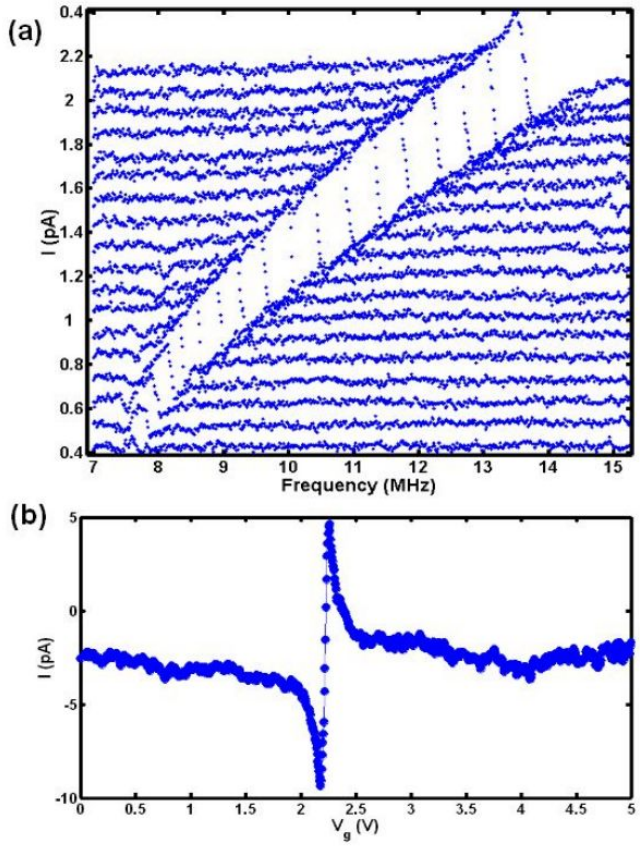

Figure 4.2: Resonance frequency shifts with increasing gate voltage. **(a)** Evolution of the resonance from Fig. 4.1a as the gate is changed from 2V to 3.5V. The traces are offset for clarity. **(b)**. The resonance can also be observed by fixing the driving frequency at 9MHz and sweeping the gate voltage.

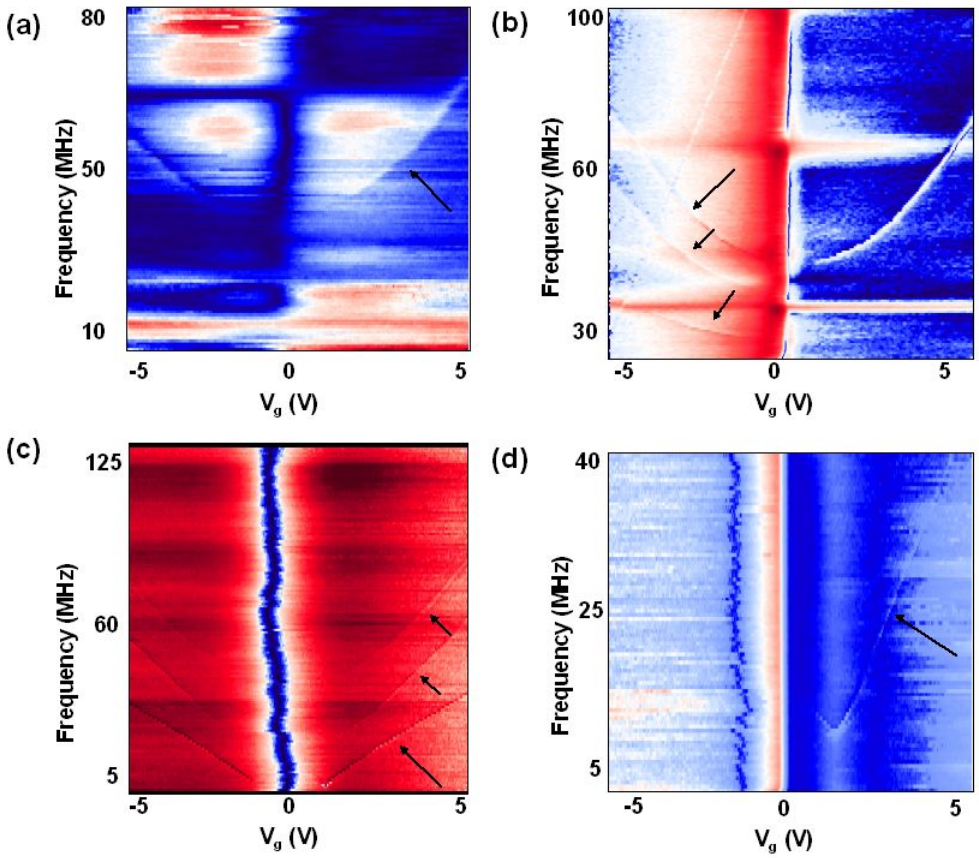

Figure 4.3: Examples of measured megasweeps. Detected current, in colorscale, as a function of the driving frequency (y-axis) and the gate voltage (x-axis) for four different devices. Positions of the resonances are marked with black arrows.

these dispersions and ignore the overall value of the current and the background. We will come back and analyze those in detail in Chapter 5.

There are three things worth noticing about the change in the position of the resonances as a function of gate voltage: first we see that the dispersion is approximately symmetric about zero gate voltage, second we observe several distinct resonances for most of the devices, and finally we see that the resonant feature shifts upward monotonically as the magnitude of the DC gate voltage is increased. In the following section we will qualitatively explain these observations.

4.3 NT resonator model

In order to make a model for a CNT resonator, let's look back at an SEM image of one of the suspended devices (Fig. 3.1a). We see on the image that the CNT appears to be slack, as indicated in the schematic. Slack here means that the tube is longer than the distance between the suspension points, which is a result of the NT's curvature on the substrate prior to suspension. We define slack s as the ratio of the extra length in the nanotube to its length L, where the excess length is the difference between the length of the CNT and the distance between the suspension points, W.

$$s = \frac{L - W}{L} \tag{4.1}$$

Slack was observed for almost all imaged devices in a SEM and has also been inferred from AFM force measurements on similar samples (Minot et al., 2003). The typical values of slack extracted from those experiments were on the order of $1\% - 2\%$. For the device geometry presented in Figure 3.1 with $W = 1.75\mu$m this corresponds to a sagging distance of $150 - 200$nm. For simplicity we assume that the clamping angles are zero in both the y, and z directions; in other words, that

the nanotube is confined to one plane and clamped horizontally. The profile of the nanotube is then a profile of a buckled beam (Fig. 4.4a). The DC gate voltage creates a DC force on the nanotube that we assume for a moment to be applied uniformly along the length of the nanotube. Under such a force the nanotube is pulled down, changing its profile according to the strength of the applied force. For very small forces the flexural rigidity of the tube is the dominant force scale, and the profile of the CNT is still given by the profile of a buckled beam: we refer to this force range as the *bending* regime. As the force increases, the flexural rigidity of the CNT is overcome and the CNT profile forms a catenary (Fig. 4.4b): we refer to this regime as the *catenary* regime. As the force is increased even further the tube starts to stretch. The extensional rigidity of the tube becomes dominant and the tube enters the *elastic* regime (Fig. 4.4c); the profile of the tube is still catenary.

In this model for the CNT resonator the profile and tension are controlled by a uniform downward DC force, set by the DC gate voltage. The resonant frequency of the CNT depends on both the NT's tension and the NT's profile. The nanotube can have two different kinds of vibrations: in-plane and out-of-plane (see Figs. 4.4d, e). These vibrations are degenerate at zero slack, but with finite slack they have different frequencies due to symmetry breaking. Harmonics of both of these kinds of modes can be excited with frequencies increasing with the number of nodes in the mode. It is, therefore, not surprising that we see several distinct resonances for a given device. These could be some of the harmonics of the fundamental in-plane and out-of-plane vibration modes.

In beam mechanics (section 2.3) the resonant frequency of the beam increases monotonically with tension. We expect the same effect with a slack beam. The

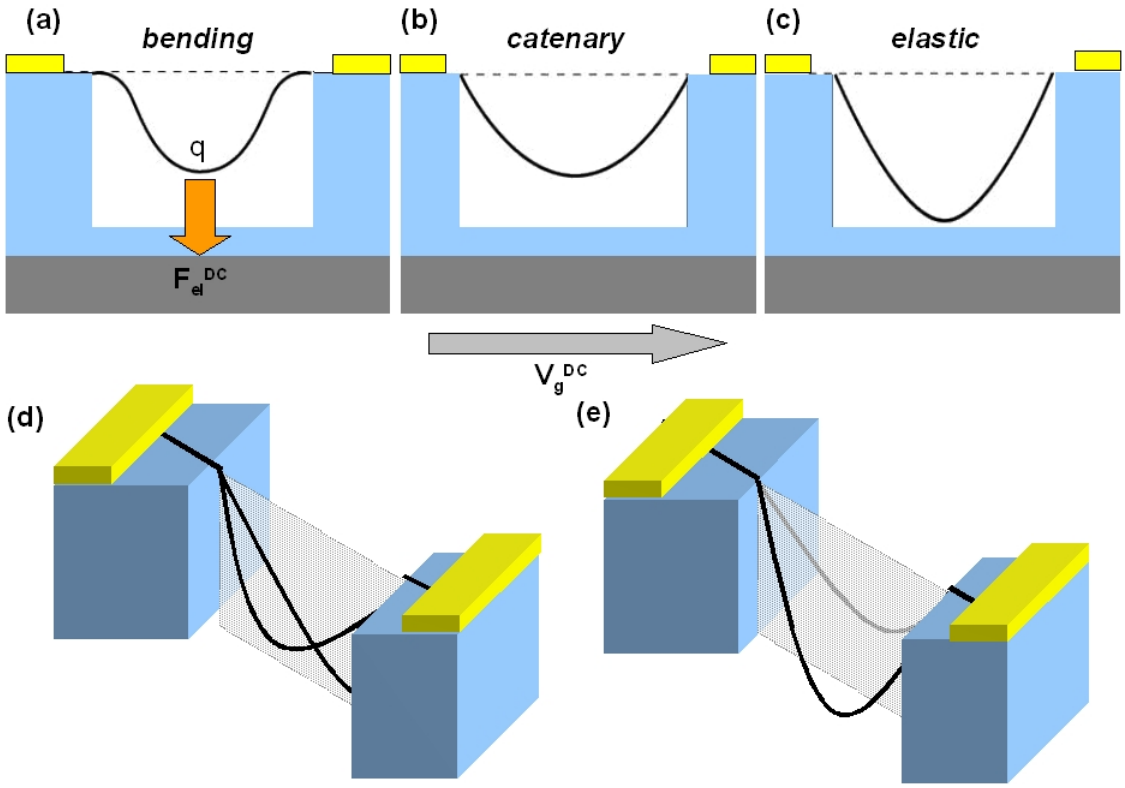

Figure 4.4: NT Resonator model. **(a),(b),(c)** Schematics of a CNT resonator profile in bending, catenary and elastic regimes, respectively. **(d)** A schematic of the fundamental in-plane vibrational mode. **(e)** A schematic of the fundamental out-of-plane vibrational mode.

tension in the CNT is set by the DC force on it and, using Eq. 3.4, we see that the DC force depends on the square of the applied DC gate voltage. In a real system the tube will feel a potential in addition to the one set by the gate voltage due to the work function difference between the tube and the contacts and various dopants. This potential can be incorporated into Eq. 3.4 as an offset gate voltage V_0, so that the DC force on the tube becomes

$$F_{\rm el}^{\rm DC} = \frac{1}{2} C_{\rm g}' \left(V_{\rm g}^{DC} - V_0 \right)^2 \tag{4.2}$$

From this relation we see that the CNT tension and the dispersion of its resonant frequency only depend on the magnitude of the voltage, are symmetric about $V_{\rm g}^{\rm DC} = V_0$ and increase monotonically with gate voltage.

4.4 Calculating resonant frequencies

We now analyze our model and present the results of numerical simulations (Üstünel et al., 2005) that will be discussed below. In our analysis we closely follow Üstünel et al. We calculate how the gate voltage affects the resonances of a buckled beam with small slack in three different regimes: bending, catenary, and elastic.

Before going into the details of the calculation, we summarize the basic result that is illustrated in Fig. 4.5. In the bending regime the vibration modes are similar to the doubly clamped beam modes. For small induced tensions the change in the frequency $\Delta\omega_0$ is proportional to tension T, and thus $\Delta\omega_0 \sim T \sim V_{\rm g}^2$. In the catenary regime the flexural rigidity is overcome and the CNT is similar to a string under tension with $\omega_0 \sim \sqrt{T} \sim V_{\rm g}$. In the elastic regime the CNT is stretched, and we still treat it as a string under tension with $\omega_0 \sim \sqrt{T}$. Since the extensional rigidity is now dominant, the induced tension starts saturating with increasing gate

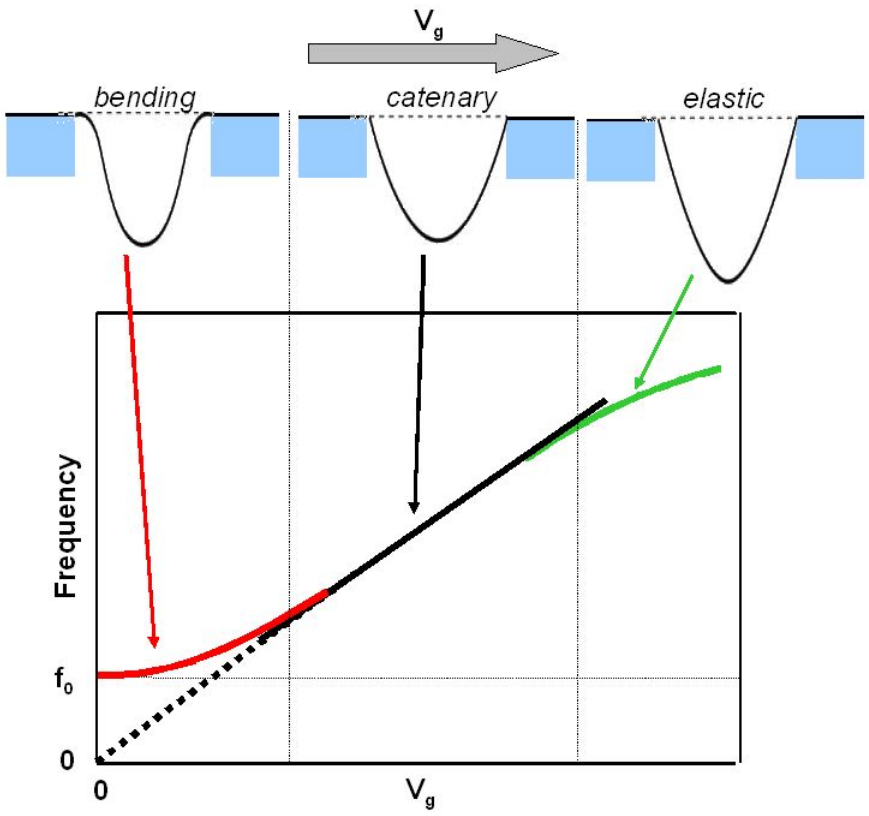

Figure 4.5: A qualitative prediction for the resonance frequency dispersion. In the bending regime the resonance frequency depends quadratically on the gate voltage, in the catenary regime the resonance frequency changes linearly, and in the elastic regime the dependence becomes sub-linear.

voltage, and the dispersion is sub-linear. So overall the frequency first changes quadratically on the gate voltage, then continues linearly, and eventually slowly starts to saturate at high gate voltages.

All the calculations presented here are done for a typical CNT device. We summarize the characteristics of such a device in Table 4.1.

Bending regime

For no force, $F_{\rm el}^{\rm DC} = 0$, and zero slack, the problem reduces to that of the doubly clamped beam with no tension, which was solved in section 2.3. The in-plane and out-of-plane modes are degenerate and their resonance frequencies are determined by the flexural rigidity of the nanotube and are given by (Eq. 2.21)

$$\omega_{\rm n}^{\rm bend} = \left(\frac{\beta_{\rm n}}{L}\right)^2 \sqrt{\frac{EI}{\mu}} \tag{4.3}$$

where E, I, and μ are the Young's modulus, moment of inertia, and linear mass density of the tube, respectively. $\beta_{1,2,3}$ are equal to 4.75, 7.85 and 11. These points are indicated as open circles in Fig. 4.6d for $s = 0$.

As slack is introduced, the tube buckles due to the Euler instability and the symmetry of the problem changes. For small forces, $F_{\rm el}^{\rm DC} \ll EI/L^2$, the flexural rigidity dominates the extensional rigidity. This means that the vibrations of the CNT are primarily due to NT's bending and not stretching, which essentially means that the length of the tube is constant under vibrations. Due to this length constraint, slack affects resonant modes differently with different symmetries, such as the in-plane and out-of-plane modes or the even and odd harmonics of their fundamental modes. This effect is illustrated in Fig. 4.6.

The out-of-plane modes are almost unaffected by slack since the length of the tube does not change during vibration, with the exception of the fundamental

Table 4.1: Parameters for a typical CNT device

Parameter	**Symbol**	**Value**
Radius	r	1.5nm
Length	L	1.75μm
Shell thickness	h	0.34nm
Slack	s	1%
Elastic modulus	E	1TPa
Linear mass density	μ	5ag/μm
Cross-sectional area	A	2nm^2
Moment of inertia	I	3×10^{-37}
Capacitance	C_{g}	1.3×10^{-17}F
Capacitance derivative	C'_{g}	4×10^{-12}F/m

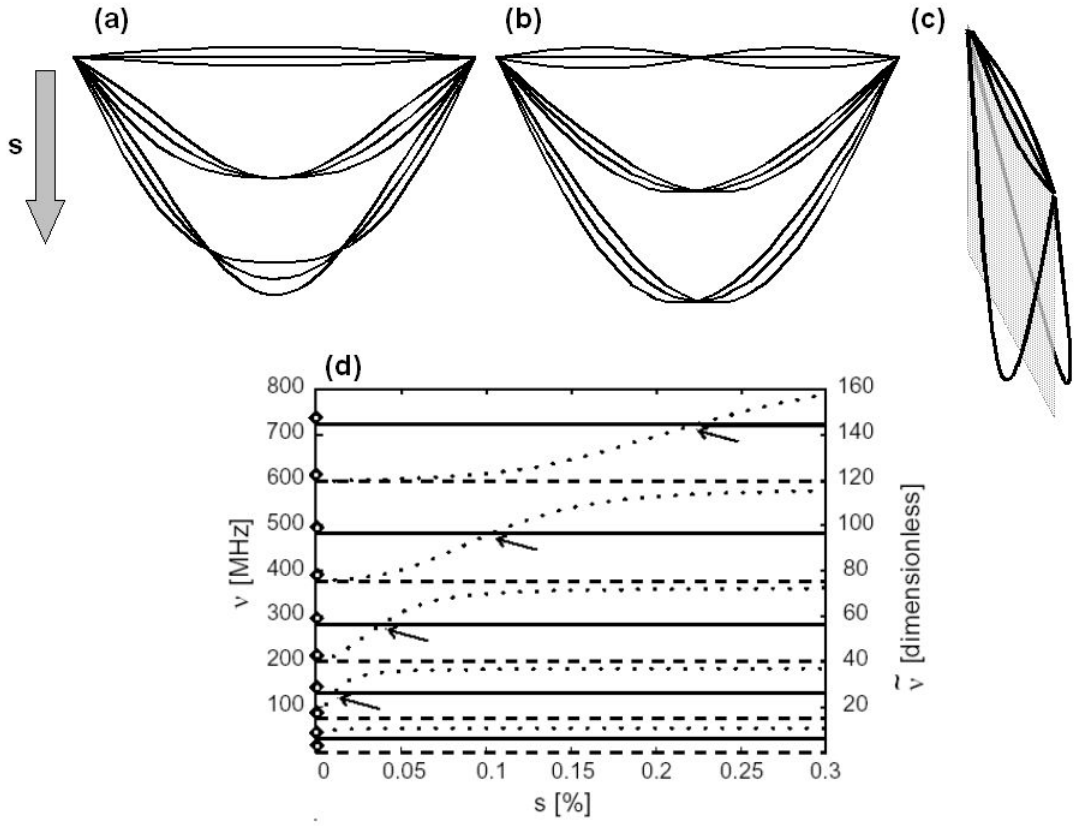

Figure 4.6: Effect of slack on different modes. **(a)** The even harmonics of the fundamental in-plane vibrational modes acquire two additional nodes as slack is increased. **(b),(c)** The shape of the odd harmonics of the fundamental in-plane mode and the all of the harmonics of the out-of-plane modes remains unchanged. **(d)** Numerically calculated frequency shift of all of the resonance modes with increasing slack for the out-of-plane modes (dashed lines), and odd and even harmonics of the in-plane modes (solid and dotted lines, respectively) (Üstünel et al., 2005).

mode, which, due to symmetry, corresponds to a rotation about the clamping axis at finite slack and thus has zero-frequency at zero external force (see Fig. 4.6c). Any symmetry breaking mechanisms (for example, different clamping angles) cause the mode to acquire a finite frequency. For the other out-of-plane modes the values of β_n for the resonance frequencies are slightly modified with the introduction of slack, but for small slack this modification is independent of the value of the slack itself.

The odd harmonics of the in-plane modes are also affected only slightly by slack as the length constraint is met automatically due to odd symmetry (Fig. 4.6b). Their frequencies then only change due to a small change in the values of β_n in the same fashion as for the odd harmonics of the out-of-plane modes. The degeneracy between the two is then not broken. The even harmonics of the in-plane modes are modified the most (Fig. 4.6a). As slack is increased the modes acquire two additional nodes in order to conserve the length, and their resonance frequencies increase to those of the corresponding out-of-plane modes, which results in a mode crossing between the odd and the even harmonics (illustrated by an arrow in Fig. 4.6d).

Catenary regime

In the catenary regime, the force is intermediate, $F_{\rm el}^{\rm DC} \sim EI/L^2$, and a tension T is induced in the beam. The resonance frequencies are given approximately by the tense string model (Eq. 2.26),

$$\omega_n = \frac{\pi n}{L}\sqrt{\frac{T}{\mu}} \tag{4.4}$$

We now need to express the tension induced in the nanotube in terms of the applied DC force $F_{\rm el}^{\rm DC}$. In principle, if $z(x)$ defines the profile of the nanotube along its

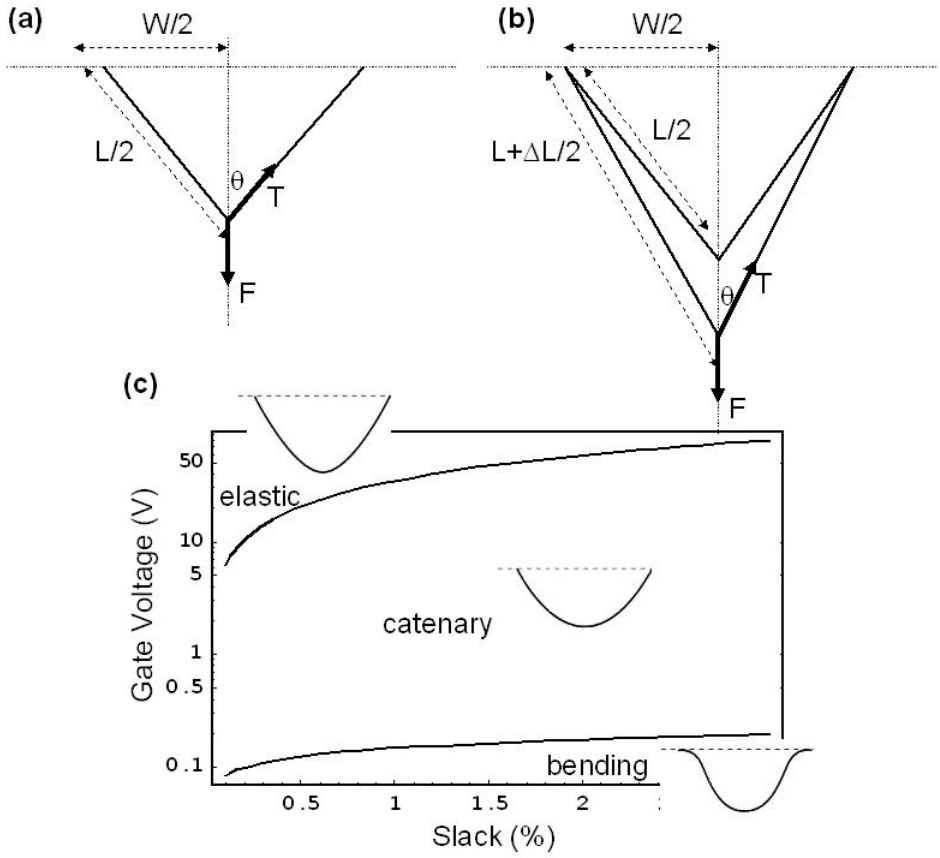

Figure 4.7: Calculating the dispersions and the applicability of the regimes with a toy theoretical model. **(a)** A schematic of the toy model for the catenary regime. The loading force F is applied in the center of the CNT of length L. The distance between the clamping points is W. **(b)**. A schematic of the toy model for the elastic regime. The CNT is now subject to a larger force, that stretches the CNT by ΔL. **(c)** A diagram of the applicability of different regimes in the slack-gate voltage space calculated for a typical device described in table 4.1

length coordinate x under $F_{\rm el}^{\rm DC}$, we recall that the tension in the nanotube is given by (Eq. 2.27)

$$T = \frac{EA}{2L}\int_0^L z'^2 dx \tag{4.5}$$

where A is the area of the CNT and z' is the spatial derivative of z. In order to find the tension, we can first find the profile of the CNT from the equilibrium equation (Eq. 2.12) and then find the tension self-consistently (Sapmaz et al., 2003). We can easily solve a simplified model, where the applied force is concentrated in the center (see Fig. 4.7a). In this case the tension is defined by $F_{\rm el}^{\rm DC} = 2T\cos(\theta)$, where θ is the angle between the nanotube and the vertical axis. Expanding this in terms of the length of the nanotube L and the distance between the clamping points W we find that

$$T = \frac{F_{\rm el}^{\rm DC}}{2\cos(\theta)} = \frac{F_{\rm el}^{\rm DC}}{2\sqrt{\frac{(L/2)^2-(W/2)^2}{(L/2)^2}}} = \frac{F_{\rm el}^{\rm DC}}{2\sqrt{\frac{L+W}{L}\frac{L-W}{L}}} \cong \frac{F_{\rm el}^{\rm DC}}{\sqrt{8s}} \tag{4.6}$$

Changing the problem to a uniformly applied force only changes the slack prefactor (Üstünel et al., 2005).

$$T = \frac{F_{\rm el}^{\rm DC}}{\sqrt{24s}} \tag{4.7}$$

The resonance frequency in the catenary regime is then:

$$\omega_{\rm n}^{\rm cat} = \frac{\pi n}{L}\sqrt{\frac{F_{\rm el}^{\rm DC}}{\mu\sqrt{24s}}} = \frac{\pi n}{L}\sqrt{\frac{C_{\rm g}'}{\mu\sqrt{96s}}V_{\rm g}^{\rm DC}} \tag{4.8}$$

To calculate how the resonant frequencies change in the transition from the bending to the catenary regime, we use the corrections calculated by Sapmaz et al. (2003) to the resonant frequencies in the bending regime for the fundamental mode (Eq. 2.28),

$$\omega = \frac{22.4}{L^2}\sqrt{\frac{EI}{\mu}} + 0.28T\sqrt{\frac{1}{\mu EI}} \tag{4.9}$$

Substituting the expression for T from Eq. 4.7 we arrive at

$$\omega^{\rm cat} = \frac{22.4}{L^2}\sqrt{\frac{EI}{\mu}} + 0.28\frac{C'_{\rm g}}{\sqrt{96s}}\sqrt{\frac{1}{\mu EI}}\, V_{\rm g}^{\rm DC\,2} \tag{4.10}$$

Thus, in the transition region the resonance frequency depends quadratically on the gate voltage.

The transition point is determined by equating the induced tension T to the force produced by the flexural rigidity EI/L^2. Setting $T = EI/L^2$ gives us the transition gate voltage

$$V_{\rm g}^{\rm DC} = \sqrt{\frac{2EI\sqrt{24s}}{C'_{\rm g}}} \tag{4.11}$$

For a typical slack of 1% that corresponds to a DC voltage of $\sim$ 0.15V. This relation is shown in the lower curve in Fig. 4.7c.

Elastic regime

In the elastic regime, the force is comparable to the extensional rigidity of the nanotube, $F_{\rm el}^{\rm DC} \sim EA$, and the length constraint is lifted. In this limit, slack is negligible compared to the elongation of the nanotube, and thus the modes are unaffected by the amount of slack in the system. In the absence of the length constraint the even harmonics of the in-plane modes return to their original shape by losing the two additional nodes. This process is exactly opposite to that illustrated in Fig. 4.6a, and it also requires an even-odd mode crossing.

To calculate the resonance frequencies in this regime we still use Eq. 4.4 for a string under tension. Equation 4.7, however, needs to be recalculated for the case of the nanotube with extension. This case is illustrated in Fig. 4.7b. The tension in the nanotube is still defined by equation $F_{\rm el}^{\rm DC} = 2T\cos(\theta)$, where $\cos(\theta)$ is given by $\frac{(\frac{L+\Delta L}{2})^2-(\frac{W}{2})^2}{(\frac{L}{2})^2}$, where the elongation of the tube ΔL is defined by the Hooke's

law $\Delta L/L = T/(EA)$. Putting it all together, we get

$$\begin{aligned} F_{\rm el}^{\rm DC} &= 2T\cos(\theta) = 2T\sqrt{\frac{(\frac{L+\Delta L}{2})^2 - (\frac{W}{2})^2}{(\frac{L}{2})^2}} \\ &= 2T\sqrt{\frac{L+\Delta L+W}{L}\frac{L+\Delta L-W}{L}} = 2T\sqrt{2s+2\frac{T}{EA}} \end{aligned} \tag{4.12}$$

Since in the elastic regime $s \ll \Delta L/L$, the equation reduces to

$$F_{\rm el}^{\rm DC} = T\sqrt{8\frac{T}{EA}} \Rightarrow T = \left(\frac{EA}{8}\right)^{\frac{1}{3}} {F_{\rm el}^{\rm DC}}^{\frac{2}{3}} \tag{4.13}$$

The resonance frequencies are still given by Eq. 4.4, and they reduce to

$$\omega_{\rm n} = \frac{\pi n}{L}\sqrt{\frac{(EA)^{\frac{1}{3}}}{2\mu}}\ {F_{\rm el}^{\rm DC}}^{\frac{1}{3}} \tag{4.14}$$

For the realistic profile, the derivation is similar and the resulting resonance frequencies are (Üstünel et al., 2005, Sapmaz et al., 2003)

$$\omega_{\rm n}^{\rm elast} = \frac{\pi n}{L}\left(\frac{5}{3}\right)^{\frac{1}{3}}\sqrt{\frac{(EA)^{\frac{1}{3}}}{6\mu}}\ {F_{\rm el}^{\rm DC}}^{\frac{1}{3}} = \frac{\pi n}{L}\left(\frac{5}{6}C_{\rm g}'\right)^{\frac{1}{3}}\sqrt{\frac{(EA)^{\frac{1}{3}}}{6\mu}}\ {V_{\rm g}^{\rm DC}}^{\frac{2}{3}} \tag{4.15}$$

Even though the resonance frequency, as expected, does not depend on slack, the transition point from the catenary to elastic regime does. The transition between the catenary and the elastic regimes occurs when the elongation of the nanotube under tension is comparable to slack. Substituting $T/(EA) = s$ into Eq. 4.13 with correct coefficients, we get that the transition occurs at

$$V^{\rm DC} = \sqrt{\frac{2\left(\frac{27}{25}\right)^{\frac{3}{2}}EA}{C_{\rm g}'}}s^{\frac{3}{4}} \tag{4.16}$$

For 1% slack, this corresponds to around 35V. Thus, the elastic regime is not likely to be relevant for a typical device. The three regimes are shown in Fig. 4.7c in the slack gate voltage space.

Spring constants

We can alternatively express the above results in terms of the spring constants of the resonator. For small tube displacements we can approximate the CNT by a harmonic oscillator and define a spring constant $k = m\omega_0^2$. In the bending regime the spring constant for a standard device described in table 4.1 is

$$k_n^{\text{bend}} = \frac{\beta_n^4}{L^3} EI = 0.2 \times 10^{-4} \frac{\beta_n^4}{\beta_1^4} m/N \tag{4.17}$$

In the catenary regime the spring constant is

$$k_n^{\text{cat}} = \frac{(\pi n)^2}{L} \frac{C_{\text{g}}'}{9.8s} \, V_{\text{g}}^{\text{DC}\,2} = 0.2 \times 10^{-4} n^2 \, V_{\text{g}}^{\text{DC}\,2} \, m/N \tag{4.18}$$

In the elastic regime the spring constant is

$$k_n^{\text{elast}} = \frac{(\pi n)^2}{L} \left(0.06 C_{\text{g}}' \sqrt{EA}\right)^{2/3} V_{\text{g}}^{\text{DC}\,4/3} = 2.7 \times 10^{-4} n^2 \, V_{\text{g}}^{\text{DC}\,4/3} \, m/N \tag{4.19}$$

Expectations for a typical device

Having derived the analytical expressions for all of the regimes, we can estimate what the dispersion curves look like for a typical device. We ignore the elastic regime, as it is not achievable in our experimental setup, and are left with the bending and catenary regimes (Eqs. 4.3, 4.8). To approximate the transition region we add the spring constants for the bending and the catenary regimes. This approximation seems valid since in the transition region both the bending restoring force and the elastic restoring force are relevant. The resulting resonant frequency is then $\omega = \sqrt{(k^{\text{bend}} + k^{\text{cat}})/m}$. Using Eqs. 4.17 and 4.18 we arrive at

$$\omega_n = \sqrt{\omega_n^{\text{bend}\,2} + \omega_n^{\text{cat}\,2}} = \sqrt{\omega_n^{\text{bend}\,2} + a \, V_{\text{g}}^{\text{DC}\,2}} \tag{4.20}$$

where $a = \frac{(\pi n)^2}{L} \frac{C_{\text{g}}'}{9.8s}$. Figure 4.8a presents the dispersions for the first three modes calculated in this manner for device described in table 4.1.

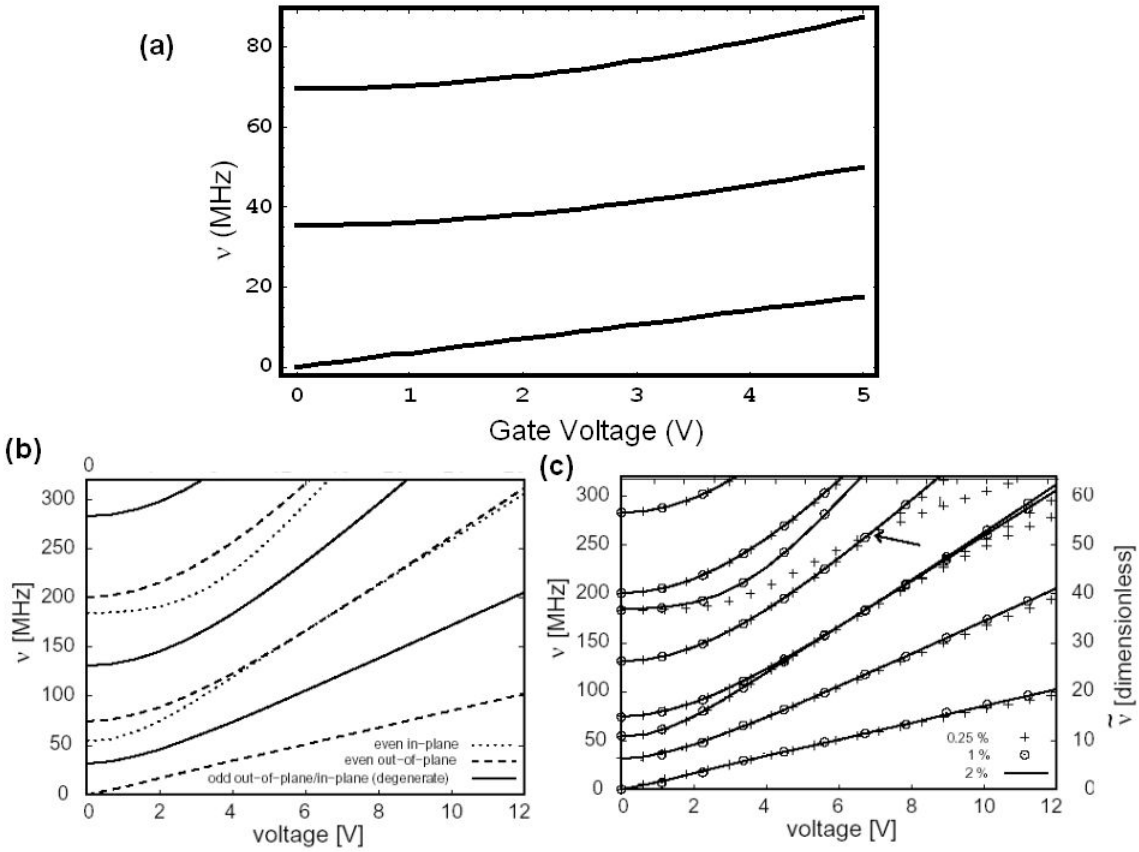

Figure 4.8: Theoretical prediction and numerical calculations. **(a)**. A calculation of the dispersion for the lowest three resonant modes for a typical device (Table 4.1). **(b)** Dispersions calculated numerically for a typical device. **(c)** Dispersions calculated for the same device for several values of slack scaled by $s^{1/4}$. From Üstünel et al. (2005)

Numerical simulations

Üstünel et al. have performed numerical simulations for this system using a finite element model. A discretized nanotube was placed in a standard potential (Eq. 2.9):

$$U = \frac{1}{2}\int_0^L \left(EA\epsilon^2(x) + \frac{EI}{R^2(x)} + \frac{F^{\mathrm{DC}}}{L} z(x) \right) dx \tag{4.21}$$

where, as we remember from section 2.3, EA is the extensional rigidity of the nanotube, EI is the flexural rigidity, ϵ is the local strain, R is the local radius of curvature, F^{DC} is the DC force on the nanotube, and z is the vertical displacement. For each given DC force and slack this potential is minimized by varying the profile of the tube and recomputing the local strains and radii of curvature until the "relaxed" profile is found. To compute the resonant frequencies a force constant matrix $K_{ij} = \partial^2 U / \partial x_i x_j$ is computed and diagonalized (for more details see Üstünel et al. (2005)). The basic results are shown in Figs. 4.6d and 4.8b and c.

Fig. 4.6d shows the behavior of resonances as the slack is increased. As described in the beginning of the section, slack only has an effect on the even harmonics of the in-plane vibrational modes, which increase their frequencies by acquiring two additional nodes and become nearly degenerate with the corresponding out-of-plane modes. Fig. 4.8b and c show the predicted dispersion relation for a typical nanotube (b) and for a typical nanotube with several values of slack (c). Since the tension in the the nanotube scales as $s^{1/4}$ (Eq. 4.7), the voltage axis was scaled by $(1\%/s)^{1/4}$ to collapse all the curves onto each other. We see that all but the the smallest values of slack (0.25% – marked by the crosses) collapse onto a single curve. The deviation for small slacks is due to the tube entering the elastic regime sooner. Overall, the results from the numerical simulations agree with our simple

model. The results of the calculations using the simple model and the numerical simulations, shown in Figs. 4.8a and b, respectively, are indistinguishable.

4.5 Model comparison with data

Having developed a model of the CNT resonator we can now go back to the data, which presented in Figure 4.9. Comparing with Figures 4.9a and 4.9b, we see good qualitative agreement with predicted dispersions. All resonances start dispersing parabolically, continuing into the linear regime as the gate voltage is increased. For the lowest resonance in Fig. 4.9b we also observe an $\omega \sim V_{\rm g}^{2/3}$ frequency dependence at large gate voltages. The frequency dependence of the resonances are thus in good qualitative agreement with theoretical expectations. The range of frequency that we find ($5\text{MHz} - 350\text{MHz}$) is also within the expected range for the expected distribution of lengths ($1\mu\text{m} - 2\mu\text{m}$) and diameters ($1\text{nm} - 3\text{nm}$).

We do, however, often find that the resonances are lower in frequency than predicted by the theoretical calculations. One possible source of this discrepancy could be additional mass coating of the CNT, for example, due to contaminants from the CNT growth or processing.

To see if the model describes the dispersion accurately, we fit the measured dispersion to the analytic dispersion relation presented in the previous section (Eq. 4.20). We have three fitting parameters: the zero gate voltage frequency $\omega^{\rm bend}$, the linear dispersion coefficient a, and the gate voltage offset V_0. The results of the fit with the fitting parameters are presented in Fig. 4.9c. We see that the majority of the resonances are described well by this model.

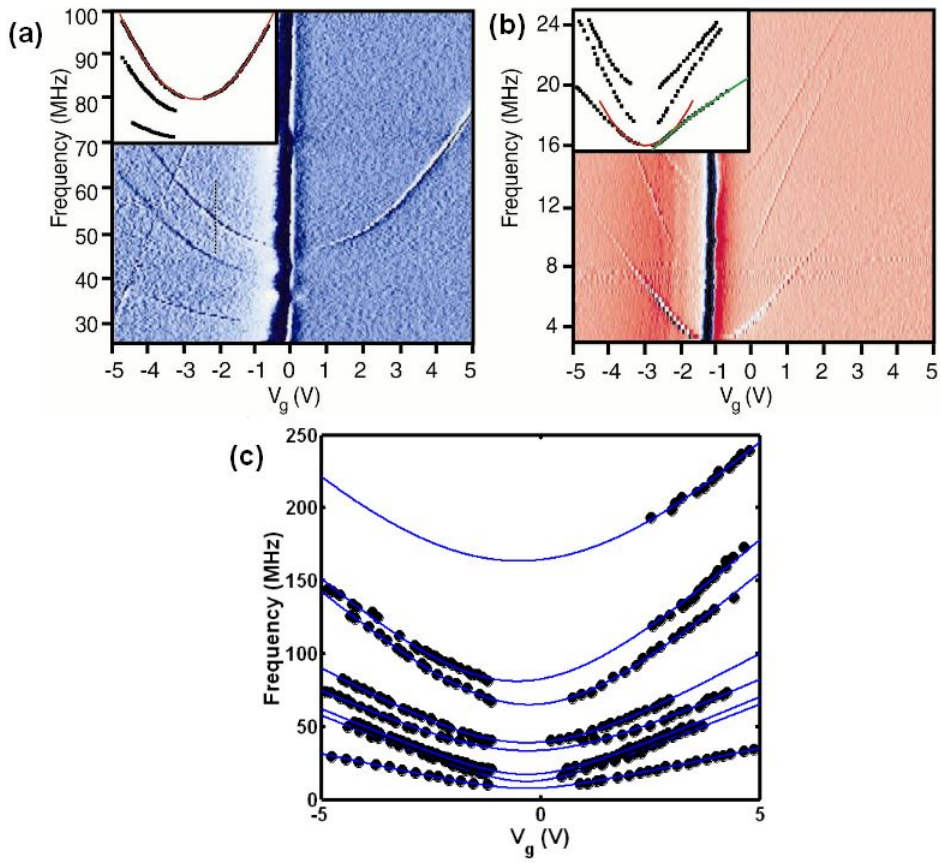

Figure 4.9: Qualitative data comparison with the theoretical model. **(a),(b)** Detected current (plotted as a derivative in color scale) as a function of gate voltage and frequency for two devices. The insets to the figures show the extracted positions of the peaks in the frequency-gate voltage space for the respective color plots. A parabolic and a $V_g^{2/3}$ fit of the peak position are shown in red and green, respectively. **(c)** A dispersion of a resonance fitted with the theoretical model from section 4.4.

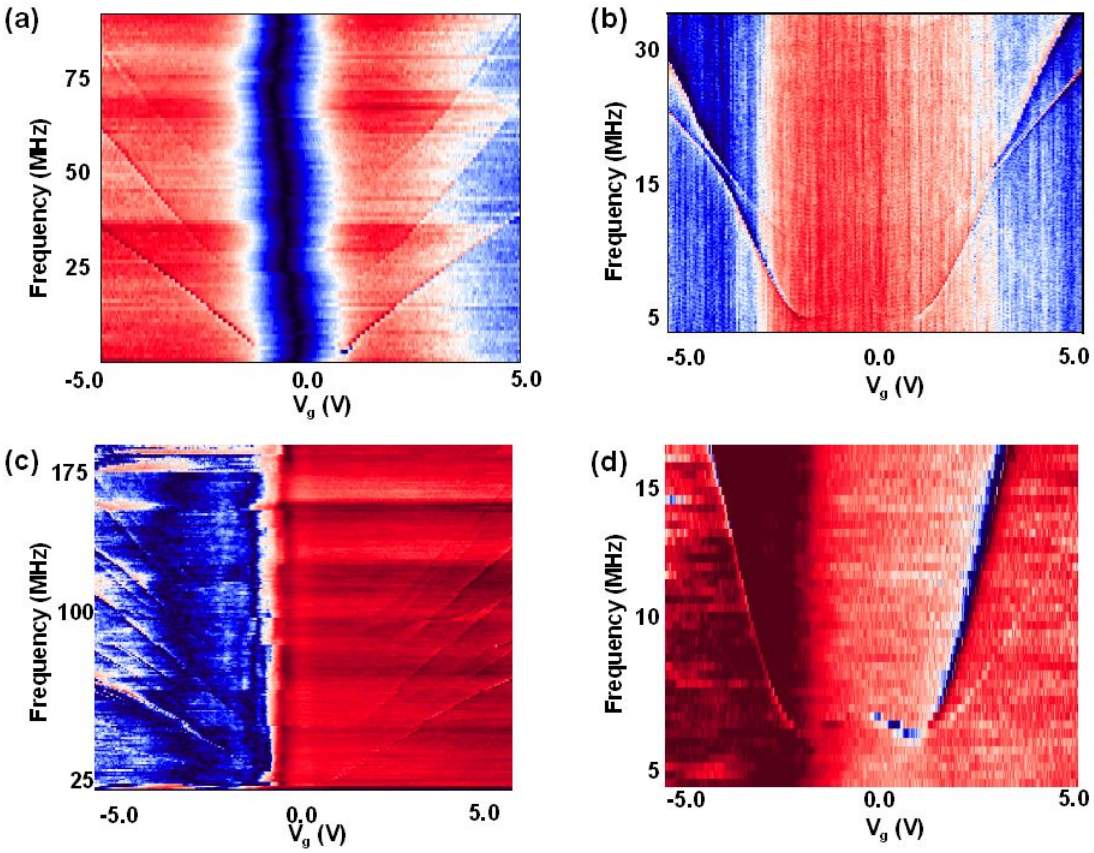

Figure 4.10: Examples of resonance with anomalous dispersions. **(a)** The lowest resonance exhibits sub-linear dispersion characteristic of the elastic regime. **(b)** An avoided crossing.**(c)** A device showing an abundance of resonances. **(d)** A devices showing a resonance with negative dispersion.

4.6 Anomalous dispersions

There are, however, several types of dispersions that we observe that cannot be explained by the above model. Typical representatives of such types are shown in Fig. 4.10.

Sub-linear dispersion

In the first class of devices (Fig. 4.10a), the resonance shows a sub-linear ($V_g^{2/3}$) dispersion behavior characteristic of the elastic regime (see Eq. 4.15), which should not be observable for the voltage of the experimental setup for a typical device. It is accessible, however, for tubes with extremely small slack. As indicated in Fig. 4.7, a CNT resonator could enter the elastic regimes at voltages as low as 5V for slacks of 0.1%. Another possibility for a sub-linear dispersion is a non-linear dependence of the potential of the tube on the gate voltage due to the charging of dopants on the tube. If the time constant for the charge movement around the tube is comparable to the time it takes to record one trace of the measurement, the actual voltage that the CNT feels will be less than the voltage applied to the gate, and the resonance will appear to saturate.

Abundance of resonances and avoided crossings

Some other anomalous dispersion examples include devices that show an abundance of resonances (Fig. 4.10c). From our theoretical model and from numerical simulations we expect $6-8$ resonances in the measurement range of 5MHz $-$ 200MHz. However, we do not expect all of them to couple to our measurement scheme, thus observing a device with the number of resonance above 5 is surprising. Even though we do not know the exact origin of this behavior, one possible

explanation is that the measured device consists of several tubes, and thus the different modes come from the different nanotube resonators.

Another type of anomaly is the presence of avoided crossings (Fig. 4.10b) in the mode dispersions. We could speculate that these crossing originate from the mode degeneracies predicted by theory that are lifted when the symmetry of the problem is broken. However, without further measurements we cannot say more on the origin of this behavior. Both of theses effects reflect, though, that there is a lot more complexity in the real system than in our simple model or in the numerical simulations.

Negative dispersion

Another class of anomalous devices (Fig. 4.10d) exhibits negative dispersion. This feature is extremely common in our devices. We have observed it for several samples made with method #1 and for all samples made with method #2 (section 3.2) whose low-gate-voltage dispersion was visible. One systematic difference between the samples made with methods #1 and #2 is that the suspended portion of the tube is typically slightly longer with the method #2 ($2\mu\text{m} - 3\mu\text{m}$) then with the method #1 ($1.25\mu\text{m} - 2\mu\text{m}$). We explain why the length of the resonator plays a role in this effect below.

Dispersions for four different samples that exhibit negative dispersion are presented in Fig. 4.11. We can explain this behavior by remembering that the CNT resonator is vibrating in a force field with a non-zero gradient. This force gradient is acting as an additional spring constant that is counteracting the restoring force and thus effectively decreasing the spring constant of the resonator and softening the resonance frequency. Remembering the DC force acting on the CNT, as de-

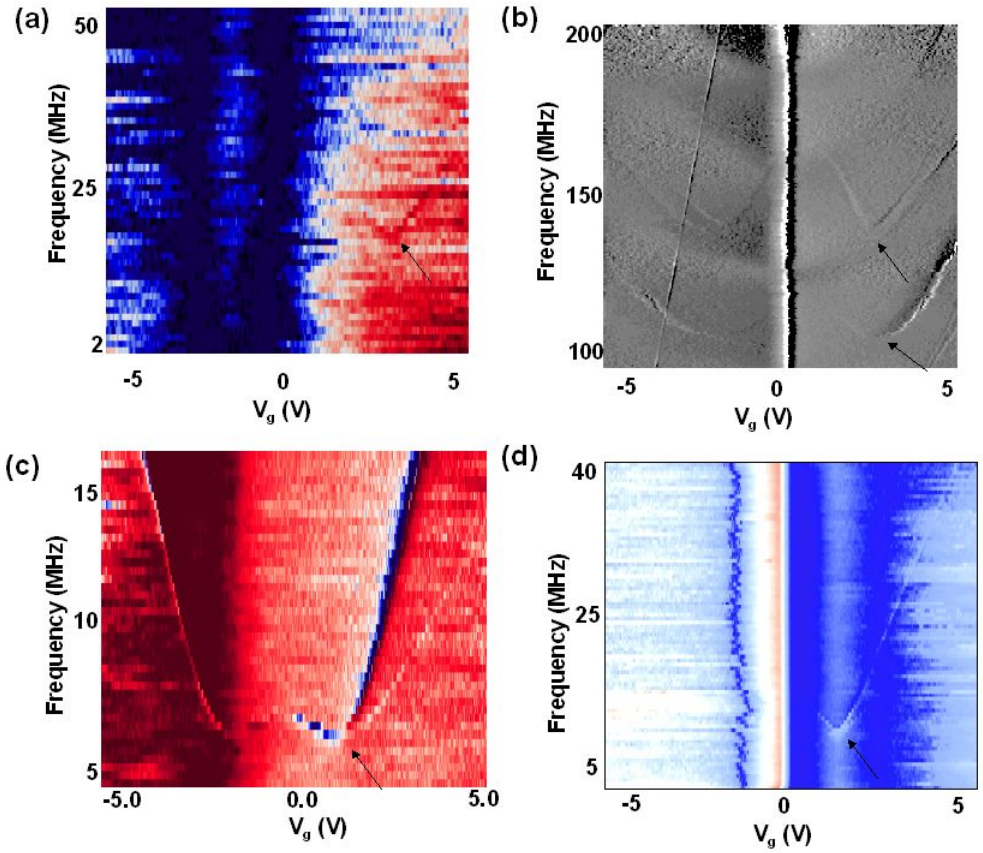

Figure 4.11: Samples exhibiting negative dispersions. In **(a)** and **(b)** the resonance is marked with an arrow for better visibility.

scribed by Eq. 3.4, we can derive that the additional spring constant acting on the CNT resonator is

$$k_{\text{softening}} = \frac{dF^{\text{DC}}_{\text{electic}}}{dz} = \frac{1}{2} C''_{\text{g}} \, V_{\text{g}}^{\text{DC}\,2} \tag{4.22}$$

Fig 4.12 shows the calculated results for the catenary and bending regimes for a fundamental mode of a typical device made with method two, using a simple capacitance model for the CNT (this model will be discussed in more detail in the next chapter). We can no longer use the arguments of adding spring constants to approximate the transition from the bending to catenary regimes. For that reason we show the effect of the electric field softening on both dispersions separately. We see that in the bending regime, the magnitude of the decrease in resonance frequency is comparable to the one observed in the measurements ($\sim 3 - 5$MHz); at higher voltages, in the catenary regime, the elastic force compensates for the softening and the frequency increases.

4.7 Conclusions

In conclusion, we have successfully observed a mechanical resonance of a suspended carbon nanotube. The device exhibits several vibrational modes, which disperse symmetrically as a function of the DC gate voltage. To explain these dispersion relations we model the suspended nanotube as a slack beam, to which we apply an external uniform downward force set by the DC gate voltage. Depending on the magnitude of the force, the nanotube can enter three different regimes: *bending*, *catenary* and *elastic*. We can analytically solve for the resonance frequencies in each of these regimes and predict the resulting dispersion curve. Alternatively, Üstünel et al. have performed numerical simulations of a slack nanotube system. The analytical results agree very well with the numerical simulations and can explain

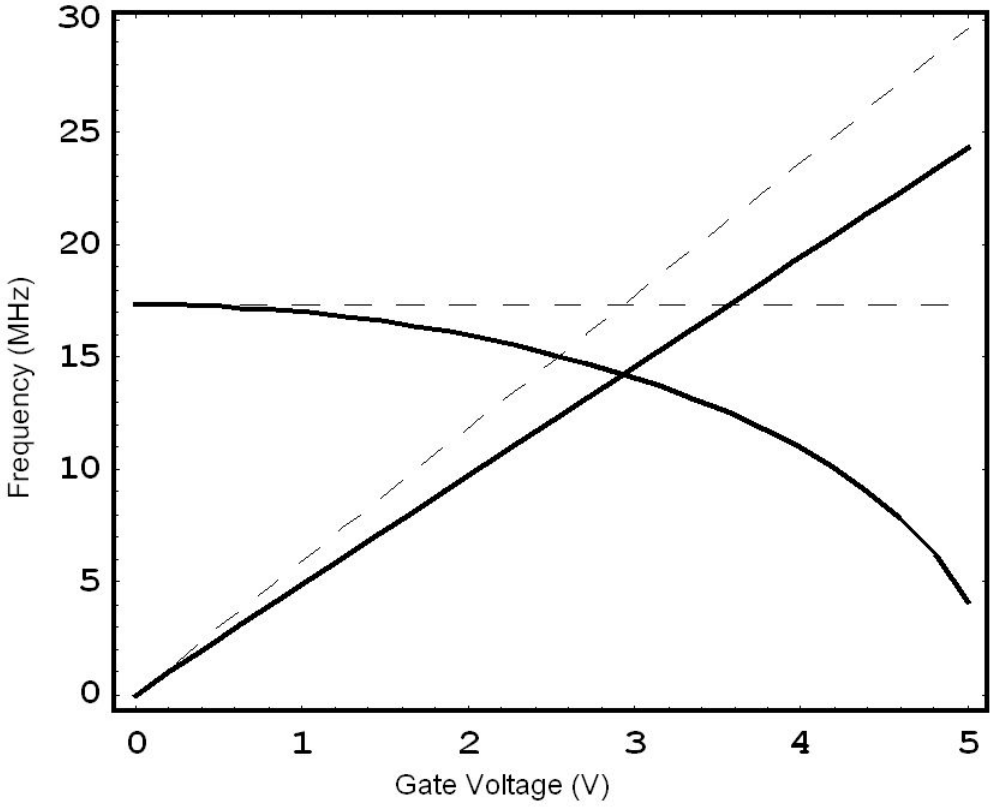

Figure 4.12: Theoretical predictions for negative dispersion for both bending and catenary regimes. The calculation was done for a typical nanotube resonator device made with the method #2.

the majority of the resonances. However, several features have been observed that do not fit in this model. Several devices show an unusually high number of resonances; several show avoided crossing types of behavior. Another set of devices shows sub-linear dispersions indicative of the elastic regimes that should not be observable at the experimental voltage ranges. Lastly, a large number of devices exhibit a temporal decrease in frequency as the DC gate voltage is increased. We propose a theory to explain these effects. However, further studies are needed to fully understand these phenomena.

CHAPTER 5

ANALYZING CNT RESONATOR PERFORMANCE

5.1 Introduction

In this chapter we present an analysis of the measurement of a CNT resonator device. First, we discuss the shape of the measured signal and present a fitting procedure that allows us to extract the parameters describing the performance of a resonator (section 5.2). In the following two sections we estimate the amplitude of motion of the resonator (section 5.3) and see how it changes with increasing driving voltage (section 5.4) (Sazonova et al., 2004). We finish the chapter with two sections on the limits of the device performance. Section 5.5 gives an estimate of the resonator's force sensitivity as it is cooled to lower temperatures; in section 5.6 we estimate the limits on its operational frequency.

5.2 Fitting the resonance

Fig. 5.1 shows the basic measurement result from the previous chapter: a measurement of the mixing current, $I^{\Delta\omega}$, as a function of driving frequency, ω, taken at room temperature in vacuum. In order to understand the shape of this signal we go back to Eq. 3.17, which we reproduce here for convenience:

$$I^{\Delta\omega} = \frac{1}{2}\frac{dG}{dq}\left(C_{\rm g}' z(\omega) V_{\rm g}^{\rm DC} + C_{\rm g}\,\tilde{V}_{\rm g}\right)\tilde{V}_{\rm sd} \tag{5.1}$$

Here $\tilde{V}_{\rm sd}$ and $\tilde{V}_{\rm g}$ are the AC voltages on the source and gate electrodes, respectively, $C_{\rm g}$ is the NT-gate capacitance, $\frac{dG}{dq}$ is the transconductance of CNT device, and $z(\omega)$ is the NT's amplitude of motion. The first term, which we refer to as $I^{\rm peak}$, describes the contribution to the current from the mechanical motion of the tube

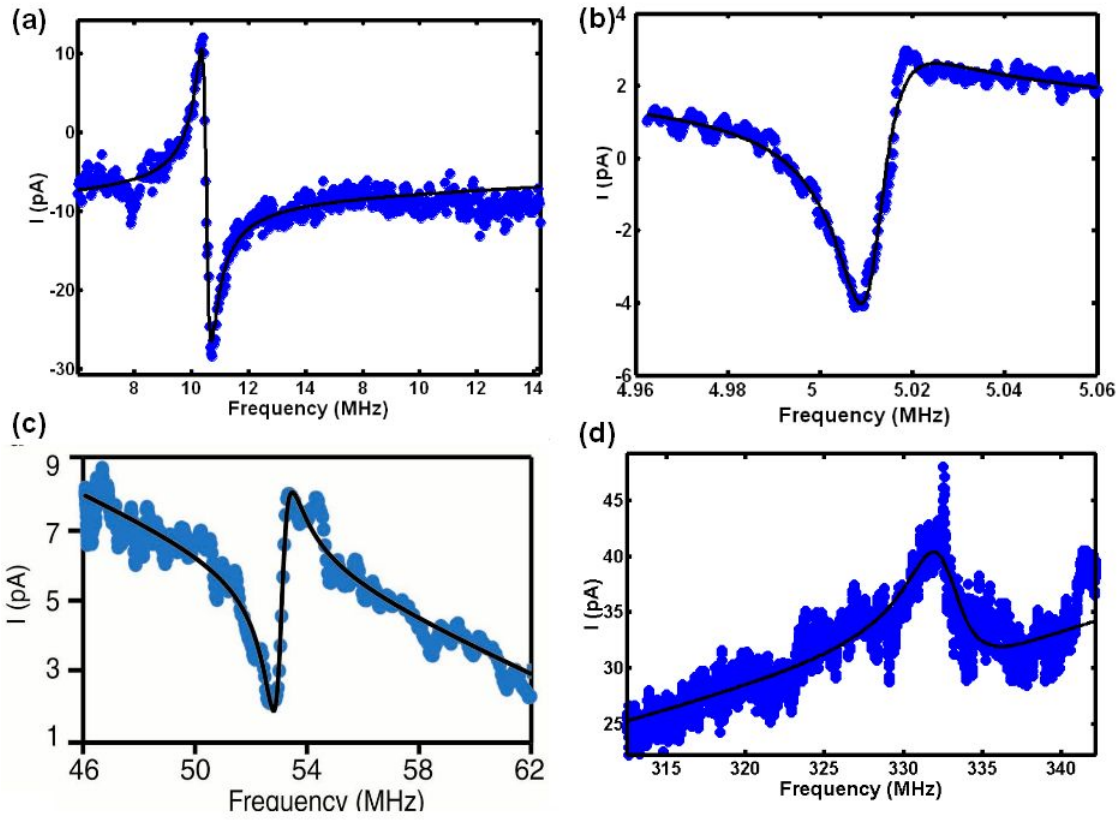

Figure 5.1: Resonances shown in Fig. 4.1 in the previous chapter, fit to a Lorentzian with an appropriate phase shift between peak and the background. Extracted parameters (good to within 3%) are: **(a)** $f_0 = 10.1$MHz, $Q = 50$, $I^{\text{peak}} = 30$pA. **(b)** $f_0 = 5.1$MHz, $Q = 100$, $I^{\text{peak}} = 7$pA. **(c)** $f_0 = 55$MHz, $Q = 80$, $I^{\text{peak}} = 6$pA. **(d)** $f_0 = 333$MHz, $Q = 81$, $I^{\text{peak}} = 10$pA.

changing the tube's potential. It is significant only near the resonance frequency and we associate it with it the sharp feature in Fig. 5.1. The second term, I^{BG}, describes the contribution to the current from the direct electrical modulation of the NT's potential by the AC gate voltage and is frequency independent, as discussed in section 3.7; we identify the background signal with the second term.

Inserting $z(\omega)$ from Eq. 2.4 into Eq. 3.17, we derive that $I^{\mathrm{peak}}(\omega)$ and $I^{\mathrm{BG}}(\omega)$ are given by

$$I^{\mathrm{peak}}(\omega) = \frac{1}{2}\frac{dG}{dq}C_{\mathrm{g}}' V_{\mathrm{g}}^{\mathrm{DC}} \tilde{V}_{\mathrm{sd}} \frac{z_0/Q}{\sqrt{\left(1-\left(\frac{\omega}{\omega_0}\right)^2\right)^2 + \left(\frac{\omega/\omega_0}{Q}\right)^2}} \tag{5.2}$$

$$I^{\mathrm{BG}}(\omega) = \frac{1}{2}\frac{dG}{dq}C_{\mathrm{g}} \tilde{V}_{\mathrm{g}} \tilde{V}_{\mathrm{sd}} \tag{5.3}$$

Naively we would just add these terms to get the total current; however, looking back at Eq. 3.5, we notice that its two terms have very different physical origin. The first comes from the electrons driven on and off of the tube by the change in the potential in phase with the mechanical motion of the CNT. The second originates from the electrons moving on and off of the the tube due to the change in the potential in phase with voltages applied to the gate and source electrodes. In principle, there is an arbitrary phase shift between these two terms, defined by the exact contact resistances and capacitances of the sample, which causes them to interfere (Knobel and Cleland, 2003). Therefore, when calculating the total current, we must add the peak and the background current contributions with a phase shift $\Delta\phi$ between them. The resulting total current is

$$I(\omega) = \frac{1}{2}\frac{dG}{dq}\left(C_{\mathrm{g}}' V_{\mathrm{g}}^{\mathrm{DC}} \frac{z_0}{Q} \frac{\cos\left(\Delta\phi + \arctan\left(\frac{\omega_0^2-\omega^2}{\omega\omega_0/Q}\right)\right)}{\sqrt{\left(1-\left(\frac{\omega}{\omega_0}\right)^2\right)^2 + \left(\frac{\omega/\omega_0}{Q}\right)^2}} + C_{\mathrm{g}}\tilde{V}_{\mathrm{g}} \right) \tilde{V}_{\mathrm{sd}} \tag{5.4}$$

Depending on the phase difference, the line shape of the signal changes from the

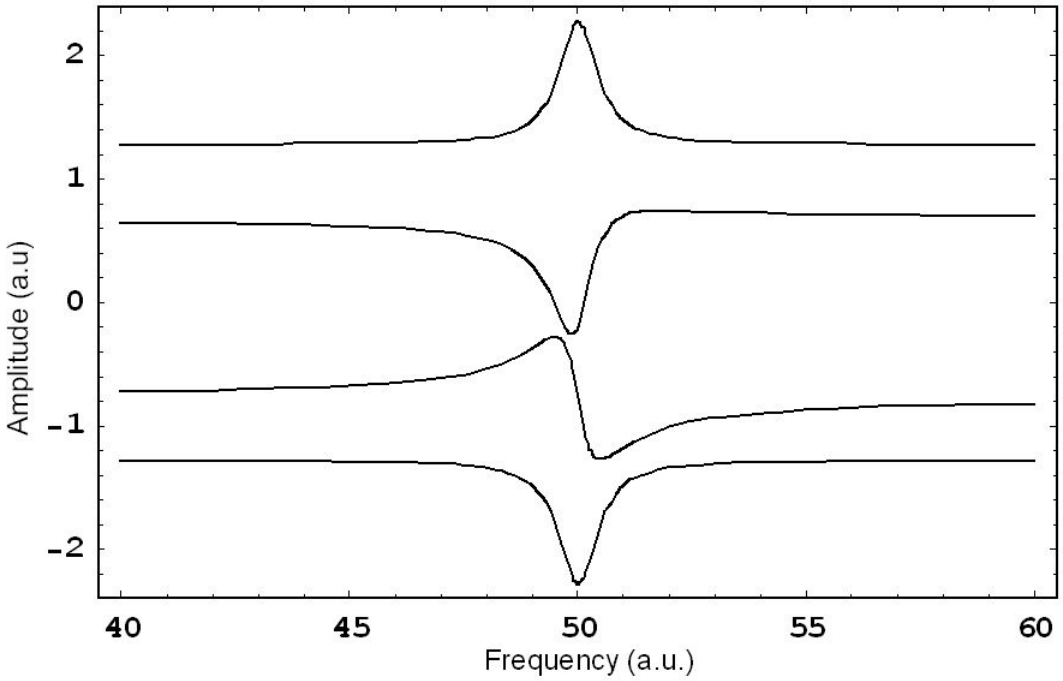

Figure 5.2: The calculated lineshape of the signal at four different values of the phase difference. From top to bottom, $\Delta\phi = 0, \Delta\phi = 3\pi/6, \Delta\phi = 7\pi/6, \Delta\phi = \pi$.

peak ($\Delta\phi = 0$) to the heart-beat shape ($\Delta\phi = \pi/2$) to the dip ($\Delta\phi = \pi$). Fig. 5.2 illustrates the possible lineshapes for different phases. The height of the peak, I^{peak}, defined as the height of the peak if $\Delta\phi = 0$ is

$$I^{\text{peak}} = \frac{1}{2}\frac{dG}{dq}C_{\text{g}}' V_{\text{g}}^{\text{DC}} \tilde{V}_{\text{sd}} z_0 \tag{5.5}$$

From discussion in section 3.7, we know that the background current changes with driving frequency due to capacitive losses and circuit resonances. For the frequency interval of the resonance we can approximate that frequency dependence by a straight line.

$$I^{\text{BG}}(\omega) = \frac{1}{2}\frac{dG}{dq}C_{\text{g}} \tilde{V}_{\text{g}} \tilde{V}_{\text{sd}} \left(A + B\omega\right) \tag{5.6}$$

Using these arguments, we fit the measured current to the following functional form

$$I^{\text{total}}(f) = A + Bf + \frac{H\cos\left(\arctan\left(\frac{f_0^2 - f^2}{\Gamma f} + \Delta\phi\right)\right)}{\sqrt{\left(1 - \left(\frac{f}{f_0}\right)^2\right)^2 + \left(\Gamma\frac{f}{f_0}\right)^2}} \tag{5.7}$$

Here A, B, H, f_0, Γ, and $\Delta\phi$ are five independent fitting parameters. A and B are the intercept and the slope for the background. H controls the height of the peak on top of the background, f_0 and Γ control the position and the width of the peak, respectively, and finally $\Delta\phi$ controls the lineshape of the resonance. We transform these fitting parameters into experimental parameters, such as the center frequency, f_0, the normalized linewidth, Q^{-1}, the height of the peak, I^{peak}, and the background, I^{BG}, in the following fashion

$$\begin{aligned} Q^{-1} &= \tfrac{\Gamma}{f_0} \\ I^{\text{peak}} &= HQ \\ I^{\text{BG}} &= A + Bf_0 \end{aligned} \tag{5.8}$$

The black line in Fig. 5.1 indicates the fit to the data. As we see, the fit works

very well for all the different shapes presented; the fits are good to within 3%.[1] The extracted parameters for Fig. 5.1 are given in the figure caption.

5.3 Estimating the amplitude of vibrations

Having developed a procedure to fit the resonances, we can extract and analyze the important mechanical parameters of the resonator. The resonance frequency f_0 and its dependence on the DC gate voltage was discussed in detail in the previous chapter (Chapter 4); the quality factor Q, describing the degrees of losses in the resonating system, will be discussed in the next chapter (Chapter 6); and in the remainder of this chapter we concentrate on the information we can extract from the magnitude of the peak and background currents, I^{BG} and I^{peak}.

To begin, we use Eq. 3.31 and Eq. 5.5 to extract the amplitude of motion of the resonator. As a first step, we calculate the relative change of capacitance on resonance from the peak current using Eq. 5.2

$$\frac{C_{\mathrm{g}}' z_0}{C_{\mathrm{g}}} = \frac{2I^{\mathrm{peak}}(\omega_0)}{\frac{dG}{dq} V_{\mathrm{g}}^{\mathrm{DC}} \tilde{V}_{\mathrm{sd}}} \tag{5.9}$$

We can estimate the transconductance dG/dq analogously to the analysis for the non-suspended CNT device (section 3.7) from the DC current measurement; alternatively, we can use the measured value of the background current. The latter takes into account the signal variations due to circuit resonances and capacitive losses. The value of the relative change of capacitance on resonance is then

$$\frac{C_{\mathrm{g}}' z_0}{C_{\mathrm{g}}} = \frac{I^{\mathrm{peak}}(\omega_0)}{I^{\mathrm{BG}}(\omega_0)} \frac{\tilde{V}_{\mathrm{g}}}{V_{\mathrm{g}}^{\mathrm{DC}}} \tag{5.10}$$

In order to determine the actual amplitude of the tube's displacement on resonance

$$z_0 = \left(\frac{\tilde{C}_{\mathrm{g}}}{C_{\mathrm{g}}}\right)^{\mathrm{measured}} \frac{C_{\mathrm{g}}}{C_{\mathrm{g}}'} \tag{5.11}$$

[1] For a typical fit, the standard deviation of $(I^{\mathrm{measured}}/I^{\mathrm{total}}(f) - 1) \approx 3\%$

we need to know C_g and C'_g. A simple model of a straight beam above an infinite plane gives the following dependence:

$$\begin{aligned} C_g &= \frac{4\pi\epsilon_0 L}{\ln(2Z/r_0)} \\ C'_g &\sim C_g/Z \end{aligned} \tag{5.12}$$

Where L is the length of the tube, r_0 is the tube's diameter and Z is the distance to the gate. Using this model, we arrive that the vibration amplitude is given by

$$z_0 = \frac{\tilde{C}_g}{C_g} Z = \frac{I^{\text{peak}}(\omega_0)}{I^{\text{BG}}(\omega_0)} \frac{\tilde{V}_g}{V_g^{\text{DC}}} Z \tag{5.13}$$

From chapter 3 we recall that Z is approximately 500nm for our devices. Calculating the vibration amplitude for one representative resonance curve, presented in Fig. 5.1c, (measured at $\tilde{V}_g = 7\text{mV}$) leads to $\tilde{C}_g/C_g = 0.3\%$, and $z \sim 10\text{nm}$.

5.4 Peak amplitude dependence on the driving voltage

Figure 5.3a,b show the dependence of the peak current, I^{peak}, and the peak's full width at half maximum (FWHM) on the driving voltage of the resonator, $\tilde{V}_g$, for one device. For low driving amplitudes the response on resonance is linear in $\tilde{V}_g$ and the FWHM is roughly constant. As the $\tilde{V}_g$ is increased, the response saturates and the response peak widens. For some devices, there is also a dramatic change in the signal shape observed at these high driving voltages (Fig. 5.3b). Instead of a smooth Lorentzian dip, the system develops a hysteretic transition between low and high amplitude states of oscillation.

Linear regime

To understand these results, we first address the linear response regime. From Eq. 5.13 we know that the peak current is proportional to the amplitude of oscillation

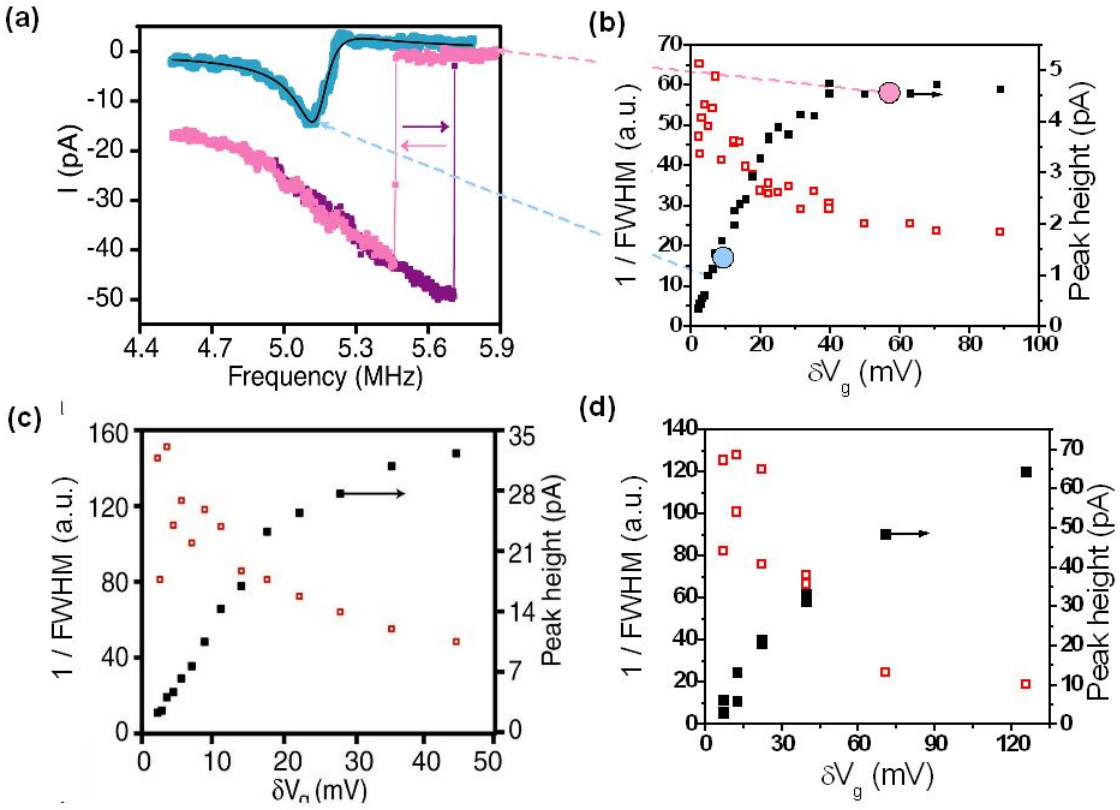

Figure 5.3: Amplitude dependence of the response. **(a)** Trace of detected current vs. frequency with the background signal subtracted for a device at two different driving voltages $V_g = 8.8$mV and $V_g = 40$mV. The solid black line is a Lorenzian fit to the low bias data. The traces of the current as the frequency is swept up and down are shown in purple and magenta, respectively. Hysteretic switching can be observed. **(b), (c), (d)** The inverse of the measured FWHM of the resonance peak and the height of the resonance peak for several devices are shown in red open squares and black solid squares, respectively, as a function of driving voltage V_g. Linear behavior is observed at low voltages, but the peak width decreases and the height of the peak saturates at higher driving voltages.

z_0 and from Eq. 3.4 we know that the driving force is proportional to the AC gate voltage $\tilde{V}_{\rm g}$. Thus the linear relation between the peak current and the driving voltage results in the linear response of the resonator. Consequently, we estimate the effective spring constant for this resonator from the slope of the amplitude vs. driving force curve. For the device in Fig. 5.3c it is 4×10^{-4}N/m. This is consistent with the spring constants for the bending and catenary regimes calculated in section 4.4. However, we need to remember that experimentally we measure the force spring constant

$$k_n^{\rm force} = \frac{\tilde{F}_{\rm el}}{z_0} Q = \theta k_n^{\rm bend,cat} \tag{5.14}$$

by measuring the vibration amplitude dependence on the driving voltage, and not the resonator spring constant

$$k_n^{\rm bend,cat} = m\omega_n^{\rm bend,cat\,2} \tag{5.15}$$

as it was defined in section 4.4. Here θ is the coupling coefficient that accounts for the fact that the CNT does not move purely in the z-direction, in which case θ would be one. Generally, the coupling is different for different modes. We, however, assume perfect coupling throughout this thesis.

Finally, we can calculate the force sensitivity of the device at room temperature. The smallest detected signal was at a driving voltage of $\tilde{V}_{\rm g} \sim 1$mV. Using Eqs. 3.4 and 5.13 above yields a motion of ~ 0.5nm on resonance and a force sensitivity of $\sim 3{\rm fN}/\sqrt{\rm Hz}$. This is within a factor of ten of the highest force sensitivities ever measured at room temperature (Jenkins et al., 2004, Stowe et al., 1997). We will discuss the limiting factors and the projections of the force sensitivity in the next section.

Nonlinear regime

As the amplitude of the oscillation is increased, we expect that non-linear effects due to changes in the spring constant become important. It is well known that non-linear resonators have a bi-stable region in their response-frequency phase space, which experimentally results in a hysteretic response (Yurke et al., 1995). The onset of non-linear effects in our case corresponds to driving voltages of 20mV. Assuming the same parameters as above yields the amplitude of motion of 30nm.

Several possible mechanisms, such as beam elongation, clamping, etc., can be responsible for the non-linear behavior. In NEMS the non-linearity is typically due to the elongation of the resonating beam (see section 2.4), and the onset of non-linearity is a well known parameter (Postma et al., 2005). In our devices the presence of slack compensates the elongation induced by the driving forces corresponding to the onset of non-linearity.

One other possible reason for this behavior is the direct dependence of the resonance frequency on the driving force, since both driving and tuning are done by controlling the voltage on the gate. From Eqs. 4.3, 4.8 the spring constant of the resonator in the bending and catenary regimes depends on the gate voltage. That means that the resonator's spring constant is modulated by the driving voltage around some central value defined by the DC gate voltage :

$$k(V_{\mathrm{g}}) = k_0(V_{\mathrm{g}}^{\mathrm{DC}}) + \tilde{k}(\tilde{V}_{\mathrm{g}}) \tag{5.16}$$

The equation of motion 2.3 for the resonator (Eq. 2.3) is then modified as follows

$$m\ddot{z}(t) + b\dot{z}(t) + k_0 z(t) + \tilde{k}(F_0\cos(\omega t))z(t) = F_0\cos(\omega t) \tag{5.17}$$

This type of equation is usually referred to as parametric amplification, as a parameter of the system (i.e. its spring constant) is modulated. Without solving

this analytically, we can estimate the magnitude of the frequency broadening due to the driving voltage for the values corresponding to the onset of non-linearity (20mV). For a typical resonance frequency of $f_0 = 50$MHz with a quality factor of $Q = 50$, and with a typical dispersion curve slope of $\Delta f/\Delta V_{\rm g}^{\rm DC} = 10$MHz/V, the frequency modulation will be

$$\Delta f = \frac{\Delta f}{\Delta V_{\rm g}^{\rm DC}} \tilde{V}_{\rm g}^{\rm non-linear} = 0.2\text{MHz} \tag{5.18}$$

which is smaller than, but comparable with, the half maximum width of the peak of $f_0/Q = 1$MHz, indicating its possible importance. We will return to possible mechanisms of non-linearity in chapter 6. Solving such equations is typically done numerically, and even though this presents a very interesting problem it is out of the scope of this thesis.

The exact cause of this hardening non-linearity is still subject to further investigations. We must also note that in all measurements of the hysteretic switching the traces were measured by sweeping the gate voltage, not the driving frequency. In such a case the driving force is larger on the high frequency side of the resonance (higher gate voltage), and smaller on the low side of the resonance (lower gate voltage). While this inhomogeneous measurement does not affect the presence of non-linearities and bi-stability, it might affect the exact shape of the resonance.

5.5 Calculations of force sensitivity

The ultimate limit on sensitivity is set by the thermal fluctuations of the CNT oscillator

$$S_F^{\rm thermal} = \frac{4k^{\rm bend,cat}k_{\rm B}T}{\omega_0 Q} \tag{5.19}$$

where $k_{\rm B}, T$ are the Boltzman constant and temperature, respectively. For a typical device (table 4.1), this translates to 15aN/$\sqrt{\rm Hz}$. The observed sensitivity is 1pN/$\sqrt{\rm Hz}$, 50 times worse than this limit.

To understand the origin of this poor sensitivity, we first consider the sources of noise in the system. The experimentally determined value for the *current noise* through the device was $\sqrt{S_I^{\rm exp}} \sim 0.3 \pm 0.05{\rm pA}/\sqrt{\rm Hz}$. Many sources of noise could be contributing to that value (Cleland and Roukes, 2002). We identify two major possible sources: the $1/f$ noise associated with the movement of charges in the substrate, and the thermal Johnson-Nyquist noise. According to measurements of Postma et al. (2001), $1/f$ noise

$$S_I^{1/f} = AI_{\rm ave}^2/f \tag{5.20}$$

is comparable to the thermal noise at the experimental frequencies $f = \Delta\omega/2\pi =$ 10kHz. The major source of noise in this system is the thermal Johnson-Nyquist noise

$$S_I^{\rm thermal} = 4k_{\rm B}TG \tag{5.21}$$

where G is the conductance of the CNT device. At room temperature for a typical device (table 4.1) this corresponds to 0.4pA/$\sqrt{\rm Hz}$, in excellent agreement with our findings. We therefore conclude that the dominating source of noise in our devices is the thermal electronic Johnson-Nyquist noise.

We can make a model of the theoretical force sensitivity in an CNT resonator. Using Eqs. 3.4 and 5.14, we can rewrite Eq. 5.5 in terms of the driving voltage $\tilde{V}_{\rm g}$

$$I^{\rm peak} = \frac{1}{2}\frac{dG}{dq}\frac{(V_{\rm g}^{\rm DC}C_{\rm g}')^2}{k^{\rm bend,cat}}Q\tilde{V}_{\rm sd}\tilde{V}_{\rm g} \tag{5.22}$$

To avoid any additional forces on the resonator we keep $\tilde{V}_{\rm sd} \leq \tilde{V}_{\rm g}$. [2]

[2] Increasing $\tilde{V}_{\rm sd}$ increases the peak current and so the sensitivity of the device.

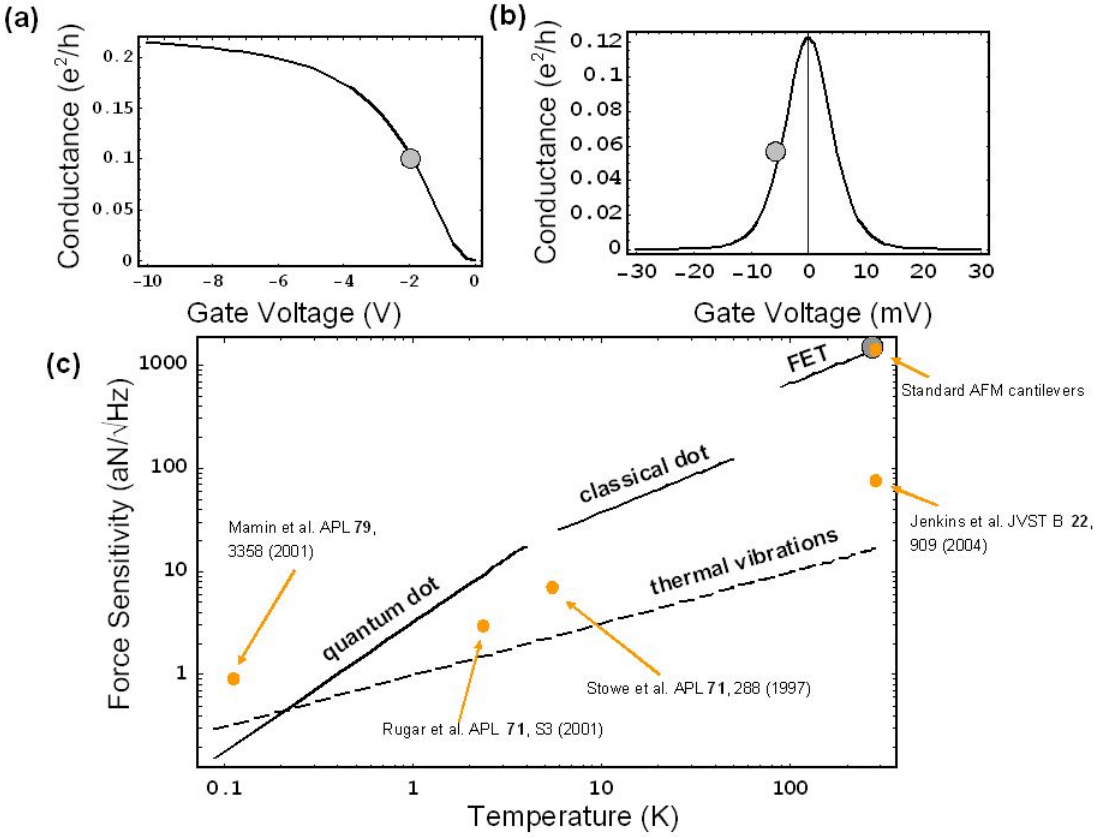

Figure 5.4: Calculation of a projected force sensitivity. **(a)** The gate dependence of the conductance for a transistor CNT device ($G_{\rm NT}(V_{\rm g}^{\rm DC})$), calculated for typical parameters. The voltage at which the maximum slope is achieved is marked by a gray circle. **(b)** The gate dependence of the conductance for a CNT device in the classical dot regime ($G_{\rm Q}(V_{\rm g}^{\rm DC})$), calculated for a typical parameters. The voltage at which the maximum slope is achieved is marked by a gray circle. **(c)** The projected force sensitivity calculated for three different regimes: FET, classical dot, quantum dot for a typical device is shown as solid black line. A dashed black line indicates the thermal vibrations limit on the sensitivity. The force sensitivities recently achieved in the NEMS community are shown as orange circles.

Equation 5.22 then leads to the following expression for the force sensitivity S_F

$$S_F = \frac{2\sqrt{S_I B}k^{\text{bend,cat}}}{\frac{dG}{dq}QB} \tag{5.23}$$

where S_I is the current noise in the device and B is the bandwidth of the measurement.

To estimate the theoretical limit on force sensitivity, we estimate the limits on the CNT conductance G and transconductance dG/dq.

The CNT's conductance consists of two parts: the contact's conductance G_{c} and the CNT's bulk conductance G_{NT} that arises mostly from scattering from acoustical phonons (Kane et al., 1998). From chapter 1 we know that for perfect transmission G_{c} is given by the Landauer-Büttiker formula

$$G_{\text{c}} = 4\frac{e^2}{h} \tag{5.24}$$

In real devices conductance is typically smaller. For the remainder of this chapter we assume the contact resistance of $G_{\text{c}} = 1/100\text{k}\Omega$. For a semiconducting CNT, the bulk conductance in the p-regime is given by

$$G_{\text{NT}}(V_{\text{g}}^{\text{DC}}) = 4\frac{e^2}{h}\frac{l_0}{L}\frac{(V_{\text{g}}^{\text{DC}}/a)^2}{1+(V_{\text{g}}^{\text{DC}}/a)^2} \tag{5.25}$$

where $a = 8e/3\pi DC'_{\text{g}}$, and l_0 is the phonon mean free path. For a detailed analysis and derivation of this formula see Rosenblatt (2005). The total conductance is given by the $1/G = 1/G_{\text{c}} + 1/G_{\text{NT}}$. Figure 5.4a illustrates the behavior of the CNT conductance for some typical device values (table 4.1). We estimate the

However, following the arguments in section 3.6, $\tilde{V}_{\text{sd}}$ creates an additional force on the CNT resonator of $\tilde{F}^{\omega+\Delta\omega} = 1/2C'_{\text{g}}V_{\text{g}}^{\text{DC}}\tilde{V}_{\text{sd}}$ at the frequency $\omega + \Delta\omega$, resulting in an additional motion at that frequency. Since the width of the resonance peak (typically on the order of $f_0/Q \approx 300\text{kHz}$) is larger than $\Delta\omega/2\pi = 1\text{kHz}$, this additional force could affect the resonance and, perhaps, lead to additional dissipation.

maximum transconductance of the device, dG/dq, by calculating the maximum slope of this graph (marked with the grey circle) and using the fact that

$$\frac{dG}{dq} = \frac{dG}{dV_{\mathrm{g}}^{\mathrm{DC}}} \frac{1}{C_{\mathrm{g}}} \tag{5.26}$$

Using these equations in conjunction with Eq. 5.23, we calculate $\sqrt{S_F} = 1.5\mathrm{fN}/\sqrt{\mathrm{Hz}}$, in good agreement with our measurements.

Decreasing temperature affects both the conductance and the transconductance of the CNT. While the contact conductance does not change with temperature, the phonon mean free path increases with the inverse of temperature, and so does the bulk conductance (Zhou et al., 2005, Rosenblatt, 2005). From Eq. 5.25 we see that the transconductance has the same temperature dependence

$$G, \frac{dG}{dq} \sim \frac{1}{T} \tag{5.27}$$

At lower temperatures the CNT enters into a *classical* Coulomb blockade regime. By this point the bulk contribution to resistance is small and the overall conductance is determined by the contacts. The gate-voltage dependence of the conductance is modulated by the individual charging events of the CNT dot that manifest themselves as Coulomb oscillations

$$G_{\mathrm{Q}}(T, V_{\mathrm{g}}^{\mathrm{DC}}) = G_{\mathrm{c}} \left(\cosh \left(\frac{\alpha e V_{\mathrm{g}}^{\mathrm{DC}}}{k_{\mathrm{B}} T} \right) \right)^{-2} \tag{5.28}$$

where $\alpha \sim 6$ (Zhou et al., 2005) is a constant relating voltage and energy scales. At even lower temperatures the transport through the CNT happens through individual energy levels of the CNT dot and the CNT is in the *quantum dot* regime.

$$G_{\mathrm{Q}}(T, V_{\mathrm{g}}^{\mathrm{DC}}) = G_{\mathrm{c}} \frac{\Delta E}{k_{\mathrm{B}} T} \left(\cosh \left(\frac{\alpha e V_{\mathrm{g}}^{\mathrm{DC}}}{k_{\mathrm{B}} T} \right) \right)^{-2} \tag{5.29}$$

where ΔE is the average level spacing. An example of a classical Coulomb oscillation at 10K is presented in Fig. 5.4b. Again, we estimate the maximum transcon-

ductance by calculating the slope of $G_{\mathrm{Q}}(T, V_{\mathrm{g}}^{\mathrm{DC}})$. From the above equations we can derive that in the *classical dot* regime

$$\frac{dG}{dq} \sim \frac{1}{T} \tag{5.30}$$

and in the quantum dot regime

$$\frac{dG}{dq} \sim \frac{1}{T^2} \tag{5.31}$$

Assuming that Johnson-Nyquist noise is the only noise source in the system, we calculate the expected force sensitivity for a typical CNT resonator device as a function of temperature. The result is shown in Fig. 5.4c as a black solid line. A dashed line indicates the limit on sensitivity set by the thermal vibrations of the resonator. We see that at low temperatures ($\sim$ 1K), the sensitivity should increase by orders of magnitude. Force sensitivities below 5aN should theoretically be attainable. This is comparable to the highest sensitivities ever measured (Stowe et al., 1997, Mohanty et al., 2000, Stipe et al., 2001), indicated on the graph with orange dots. Additionally, sensitivity may increase due to the temperature dependence of the quality factor $Q(T)$. We will discuss the quality factor and its temperature dependence in detail in the next chapter.

5.6 Frequency limits

One of the goals in the NEMS community is to push the limit of the operating resonant frequency. Resonators with fundamental frequencies up to 1.5GHz have been fabricated (Huang and Roukes, 2003). The highest resonance measured so far in our devices was at 400MHz. In this section, we estimate the inherent upper bound on the resonant frequency (not limited by the external circuit) that we can detect with our measurement technique.

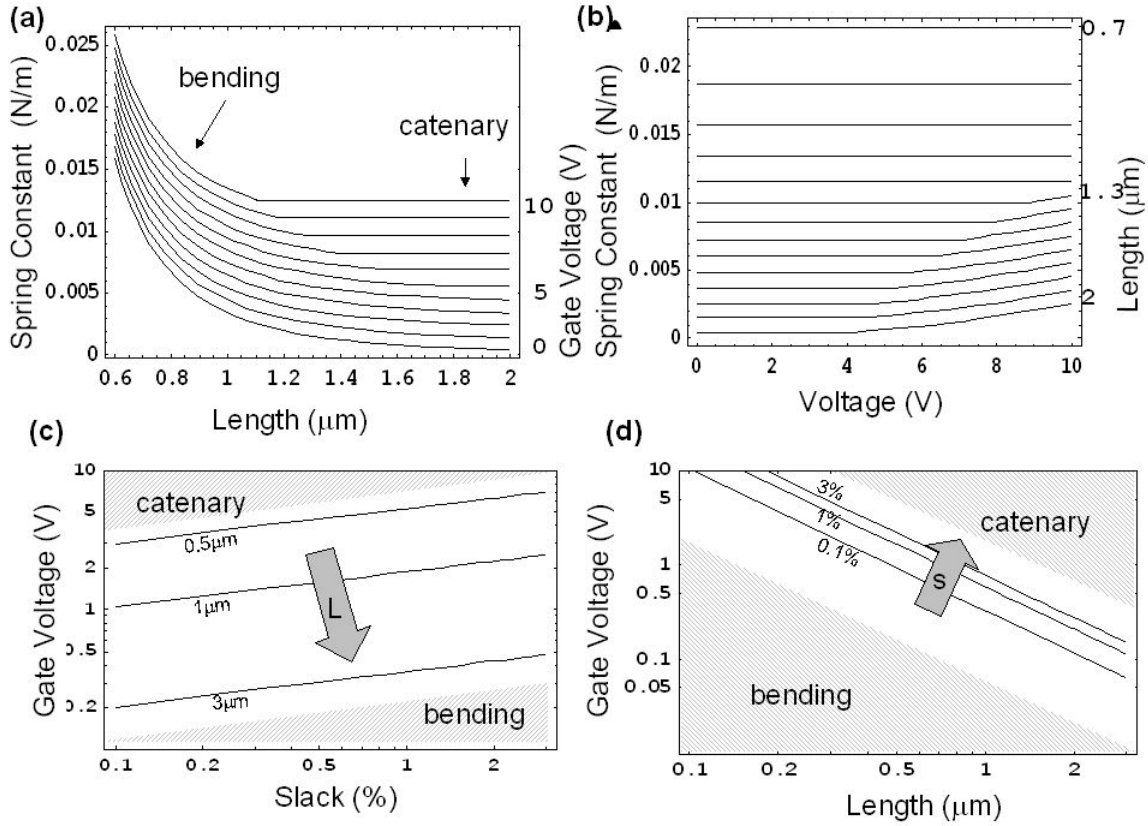

Figure 5.5: Spring constant length dependence. **(a),(b)** The spring constant (the maximum of k^{bend} and k^{cat} is presented) calculated for a typical device as a function of device length, **(a)** and gate voltage **(b)**. **(c), (d)** The transition gate voltage between the bending and catenary regimes as a function of slack **(c)** and device length **(d)**. We see that for shorter devices the bending regime dominates, as the onset of catenary regime is inaccessible with the experimentally available voltages.

One way to increase the resonant frequency in our devices is to decrease their length (see Eq. 4.3, 4.8). Then, in order to calculate the upper bound on the resonant frequency we calculate the lower bound of the NT's length.

Recall Eq. 5.22; in order to find the lower bound on the device length, we calculate the maximum possible resonant current as a function of the length of the device and find for which lengths the current is less than the noise in the system (see Fig. 5.6a).

In the FET regime the driving voltage is not bounded and the maximum resonant current is bounded by the total change in the conductance of the device in the experimentally accessible voltage range. The mixing voltage is not bounded, in contrast to the previous section, as the goal now is to maximally drive the resonator. For our calculations we used the driving and mixing voltages of 1V. For the case of the Coulomb blockade, the driving voltage and the mixed voltage are bounded by the charging energy of the dot.

$$\tilde{V}_{\mathrm{g}} \approx e/C_{\mathrm{g}} \tag{5.32}$$

In this case the dot is always in the classical regime. Using Eqs. 5.22, 5.25, 5.28, and 4.17 we calculate the maximum resonant current from the device and obtain the minimum allowed length by equating it to the noise in the system.

$$I^{\mathrm{peak}}_{\mathrm{FET,dot}} = \sqrt{S_I B} \tag{5.33}$$

Before presenting the results of the calculation, let us note that only the bending regime is relevant for the calculation for the short devices. This is illustrated in Fig. 5.5, where we calculate the value of the spring constants as a function of device length and gate voltage (panels (a) and (b)), and the transition gate voltage between the bending and catenary regimes (panels (c) and (d)). We see that for

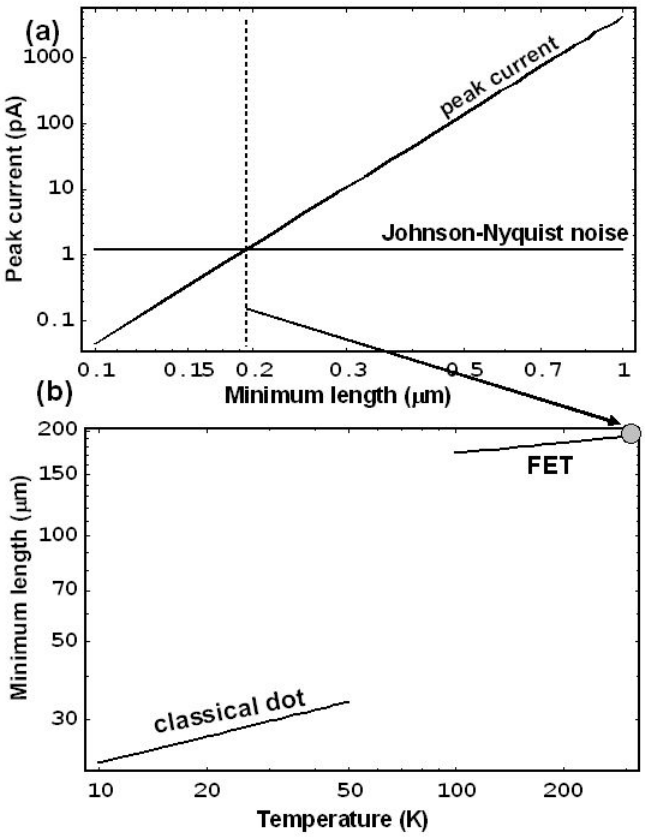

Figure 5.6: Noise-limit dependence on the device length. **(a)** Peak current and the noise in the system as a function of device length. The intersection defines the limiting length. **(b)** Calculated limiting length as a function of temperature for a typical device in the FET and classical dot regimes.

shorter CNT resonators the bending regime dominates and the catenary regime is not accessible with operational gate voltages. Ignoring the catenary regime, we perform the calculation outlined above and obtain the minimum device length as a function of temperature. Figure 5.6b presents the result. We see that at room temperature, detecting the motion of a resonator with lengths down to 160nm should be possible. At low temperatures, in the Coulomb blockade regime, the minimum length decreases even further, down to $\sim$ 10nm.

A 200nm long CNT resonator has the fundamental resonant frequency of $\sim$ 2GHz (Eq. 4.3). This is already higher than the highest resonant frequencies ever measured with NEMS (Huang and Roukes, 2003). A 30nm long CNT resonator has the fundamental resonant frequency of $\sim$ 150GHz (Eq. 4.3). It has been shown that the electronic part of the current detection setup can be extended to frequencies of 50GHz (Rosenblatt et al., 2005), so pushing the frequency limits of the resonator at least up to 50GHz seems feasible.

5.7 Conclusion

In this chapter we have analyzed the performance of a CNT resonator. After understanding the details of the shape and amplitude of the current response signal, we developed a fitting procedure that allows us to extract the three parameters that describe the performance of a resonator: the resonant frequency, the quality factor, and the amplitude of the induced resonant current. Using a simple model for NT-gate capacitance, we estimated the actual amplitude of motion of the CNT resonator to be on the order of nm. We further studied the response amplitude dependence on the driving amplitude. For low driving voltages, the CNT resonator operates in the linear regime with an effective spring constant of $\sim 4 \times 10^{-4}$N/m.

At higher driving voltages the resonator enters into a non-linear regime exhibiting a bi-stable behavior.

We calculated the force sensitivity of our device to be $3\text{fN}/\sqrt{\text{Hz}}$. We find that our measurement is limited by the thermal electron noise in the CNT. The ultimate limit on the sensitivity is given by the thermal motion of the CNT resonator and is a factor of 50 smaller. Finally, we estimated the bounds on force sensitivity and resonant frequency of the CNT resonator as a function of temperature. We find that at temperatures of $\sim$ 1K, force sensitivities on the order of several $\text{aN}/\sqrt{\text{Hz}}$ should be attainable. In the calculation of the upper bound on the resonant frequency we limit ourselves to the fundamental harmonics and switch the calculation into the calculation of the lower bound on the length of the device. We find that at low temperatures, devices with lengths down to 30nm, corresponding to resonant frequencies of $\sim$ 150GHz, should produce a detectable signal.

CHAPTER 6

QUALITY FACTOR OF CNT RESONATORS

6.1 Introduction

One of the most important parameters characterizing a resonator is the quality factor, Q, the ratio of the energy stored in the resonator to the energy lost per cycle due to damping. Maximizing Q is important for most applications. In the NEMS community, Q's up to $250,000$ have been achieved (Yang et al., 2000) and Q's in the range of $10,000 - 100,000$ are typical. As the devices are miniaturized, their respective Q's decrease as shown in Fig. 6.1a as a graph of Q vs. volume. This linear scaling of the Q's with the surface-to-volume ratio has been attributed to losses associated with dissipation at surfaces, giving promise for high quality factors from well-terminated structures such as carbon nanotubes (Ekinci and Roukes, 2005).

Previous measurements on larger MWNTs and ropes of SWNTs yielded Q's in the range between 150 to $2,500$ at room temperature (Gao et al., 2000, Poncharal et al., 1999, Purcell et al., 2002, Reulet et al., 2000). A comparison of the previously measured Q and a Q measured from one of our samples (Fig. 5.1a) with the NEMS Q's is presented in Fig. 6.1a. We see that surprisingly the CNT resonator Q continues nicely the trend established by the NEMS and MEMS. We, thus, would like to understand the dissipation in CNT resonators.

In this chapter we investigate the possible reasons for such behavior and the overall values for the quality factors, and look for the main dissipation mechanism. We first study the dependence of the quality factor on various resonator parameters, such as air pressure, temperature, device conductance, DC and AC gate voltages at room temperature (section 6.2), and then we study the temperature

dependence of the system (section 6.3), and finally we build an empirical model for the findings (section 6.5) and correlate it with various theoretical dissipation models (section 6.6).

6.2 Room temperature results

We measured 30 different devices, each producing between one and eight resonant modes, making a total of 120 vibration modes. Devices were created with three different methods (for details see section 3.2) illustrated in Fig. 6.2c. Method #1 results in a CNT suspended over a trench, clamped by the adhesion to the SiO_2 substrate; method #2 results in a suspended CNT clamped by the electrical contacts; and method #3 results in a suspended CNT on top of the contacts, clamped by the adhesion to the contacts. The electrical resistance of the devices varied from range of 60 to 800kΩ.

Following the procedure described in section 5.2, we extracted representative quality factors for each of the measured resonances at room temperature. Figure 6.1b shows the resulting quality factor distribution. We see that Q is in the range of $40 - 200$, with the maximum of the distribution around 75.

As a first step in understanding the dissipation in CNT resonators, we investigate the quality factor dependence on various parameters at room temperature. We start with the ambient conditions and device characteristics: the chamber pressure, the electrical resistance of the device, and the fabrication method. We then proceed to the characteristics of a particular resonance: the mode number, the driving force (i.e., the driving voltage), and the tension in the tube (i.e., the DC gate voltage).

As illustrated in Figs. 6.2a and b, we do not observe a correlation between

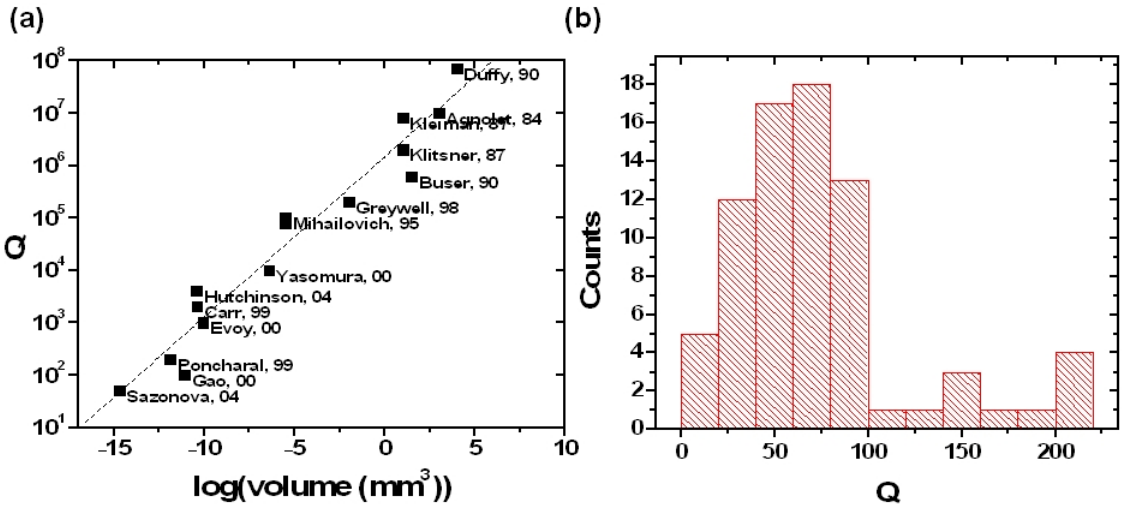

Figure 6.1: CNT quality factor comparison with NEMS. **(a)** NEMS quality factor as a function of the device volume on the log scale. A dashed line is a linear fit. **(b)** Distribution of the quality factor values measured among the 120 resonant modes of 30 CNT devices.

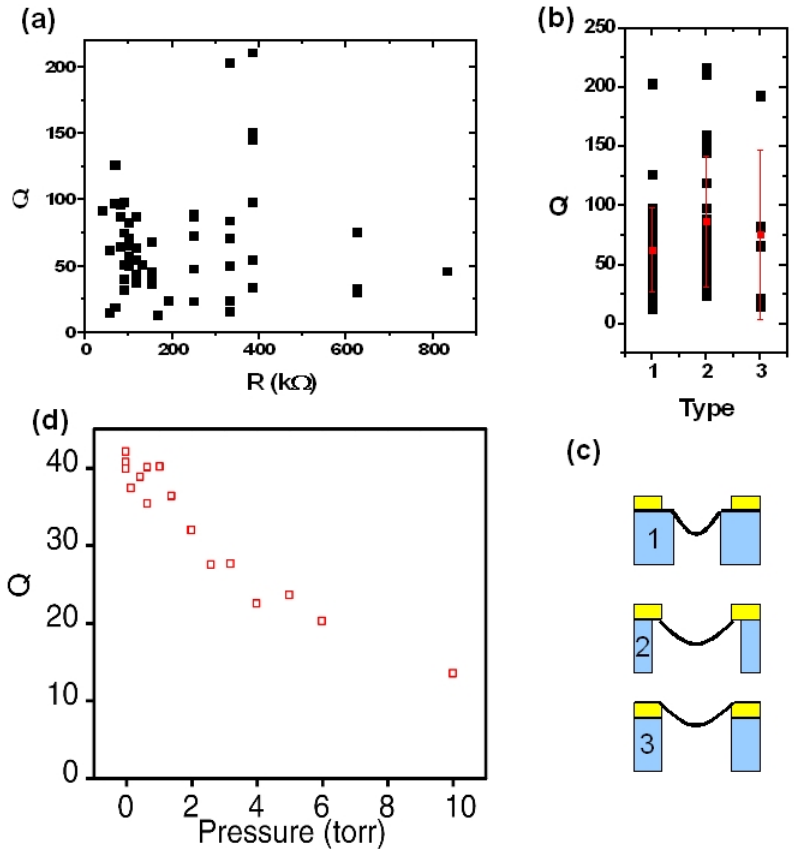

Figure 6.2: Quality factor dependence on various external parameters. **(a)** Quality factor dependence on the resistance of the device. No correlation is observed. **(b)** Quality factor dependence on the device geometry. The averages for the three distribution are all within a standard deviation of each other (indicated in red). **(c)** A schematic of the three different geometries. **(d)** Pressure dependence of the resonance peak for one device. The Q of the resonance peak is shown in red open squares. The peak was no longer observed above pressures of 10torr.

Q and the electrical resistance of a device. We also see that the quality factor distributions for devices with different geometries are very similar. The respective quality factor averages for each geometry are 62 ± 35, 87 ± 55 and 75 ± 72, all within a standard deviation of each other.

Fig. 6.2c shows the dependence of quality factor on the chamber pressure for one device. At experimental vacuum levels ($< 10^{-4}$torr), Q is independent of pressure. Only at higher pressures does Q start to decrease. The resonance is no longer observed at pressures above 10torr.

A large fraction of the measured devices had more than one resonance mode. An example of that is illustrated in Fig. 6.3a. The figure shows the dispersions for all the different vibration modes of one device with the respective Q factor values written on the corresponding mode. We see that even though the dispersions of the two neighboring modes look alike (modes #2 and #3), their quality factors are very different $Q(2) = 51$ and $Q(3) = 98$. Numbering the resonance modes consecutively, starting from the lowest frequency mode and then plotting the measured Q factor vs. the mode number, results in the plot shown on the inset of Fig. 6.3b. Despite the large fluctuations in the quality factor, there is a trend towards higher quality factors for higher frequency modes. To confirm the existence of this trend, we fit a line through the data, as shown on the inset of Fig. 6.3b. The resulting slope is ~ 5, or, normalized by the quality factor of the lowest mode, $0.012 = 12\%$/mode. Performing the same analysis for all of the devices with more than two resonance modes, yields a distribution of the Q vs. n shown in Fig. 6.3b. We see that the distribution has a peak around 20%/mode and a width of around 10%/mode, indicating that there is a correlation between the mode number and the quality factor. However, we also see that this behavior is not present for all devices, as we

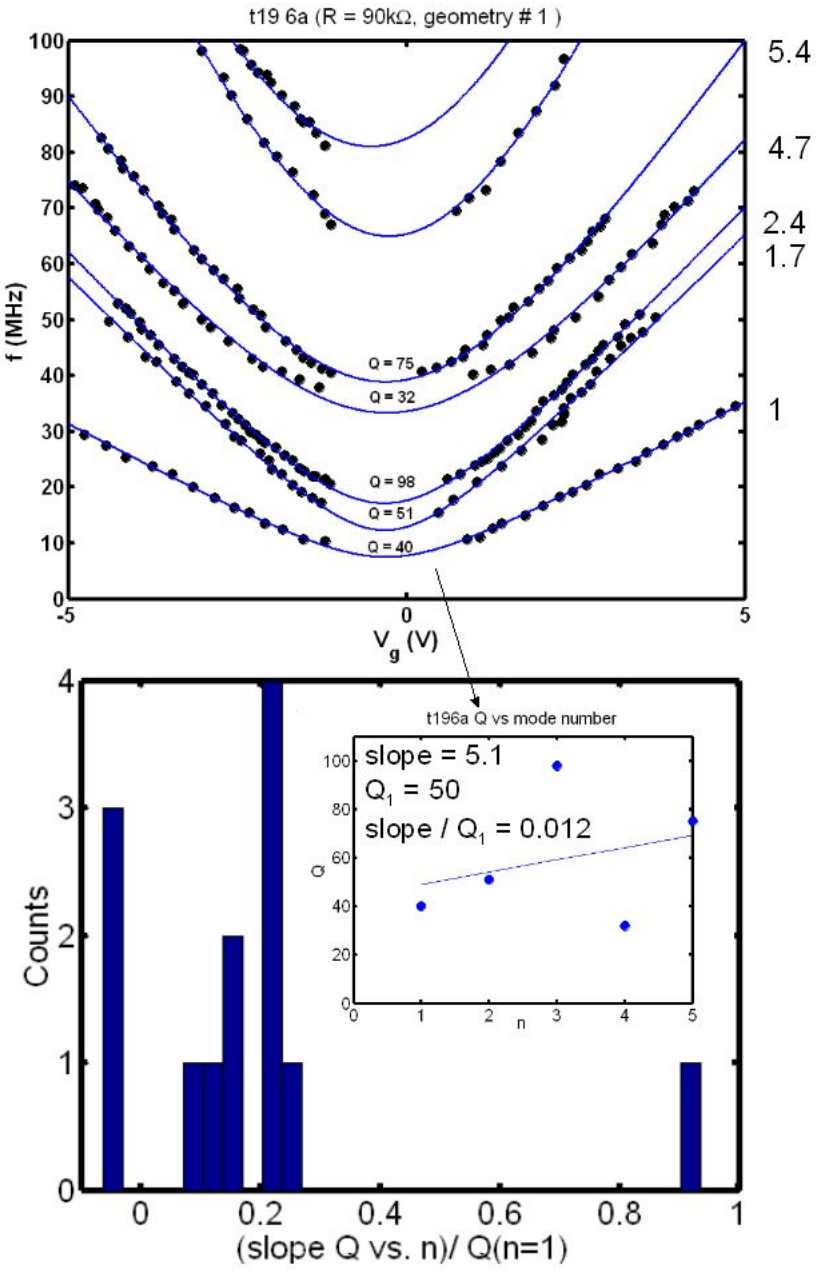

Figure 6.3: Quality factor mode dependence. **(a)** Resonance dispersions with their respective quality factors for one device. The numbers on the right indicate the zero gate frequency normalized by the frequency of the lowest mode. **(b)** Inset: Quality factors vs. the consecutively assigned mode number with a line fit for the same device. Main panel: A distribution of the Q vs. mode number slopes for all of the devices.

can observe another peak in the slopes distribution around -5%/mode.

Figures 6.4 a and b show the quality factor and the corresponding resonance frequency as a function of the DC gate voltage for two devices. Both devices have complicated dispersions (see section 4.6) and a non-trivial relation between the quality factor and the DC gate voltage.

The device in Fig. 6.4a shows one resonance mode that exhibits negative dispersion in the range of $0 - 1$V, then continues linearly until it changes slope at about 3.5V. The Q dependence on the DC gate voltage changes as the dispersion goes through these different regimes. In the negative dispersion interval, the Q exhibits a lot of scattering and slowly increases. In the linear part of the dispersion, the Q decreases and comes to a minimum roughly at the point of the inflection, where the Q starts to increase dramatically.

The device shown in Fig. 6.4b (see also Fig. 4.11d) has two resonant modes (shown in solid and open circles) that have an avoided crossing. The crossing is particularly well seen on the negative gate voltage side. The frequency of the lower resonance mode increases parabolically and then linearly with the DC gate voltage until it hits the upper resonance mode at about 3.5V. At this point, the slope of the lower resonance mode changes to the slope of the upper mode and vise versa. At the same time the quality factors of both the lower and the upper resonance modes do not change with the gate voltage until the point of the anti-crossing, where the Q of the lower mode increases to the value of the upper mode, and the value of the upper mode decreases to the value of the lower mode. In other words, the resonances "exchange" the magnitudes of their quality factors.

Finally, Fig. 6.5 reproduces Fig. 5.3, which shows the measured quality factor dependence on the driving voltage. As discussed in section 5.4, at low driving

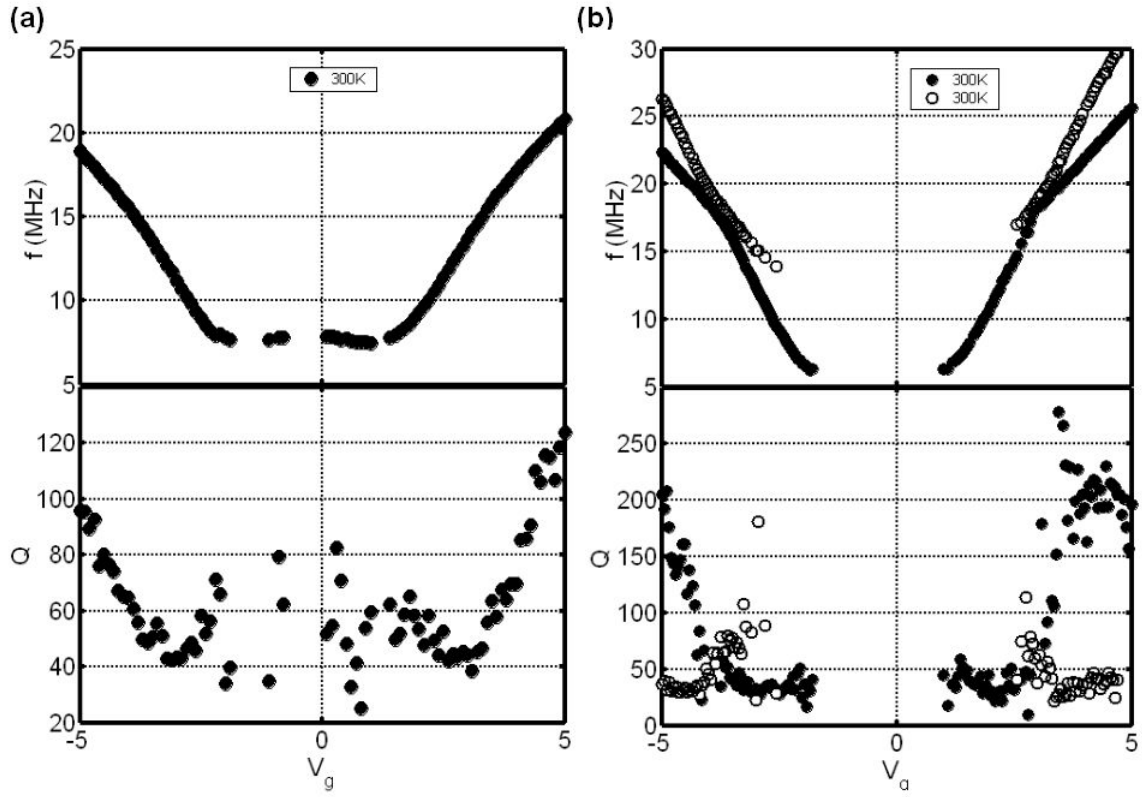

Figure 6.4: Quality factor gate voltage dependence at room temperature. **(a,b)** Resonance frequency (upper panel) and the quality factor (lower panel) vs. DC gate voltage for two different devices. The quality factor changes its behavior at the gate voltages corresponding to the inflection in the frequency curve.

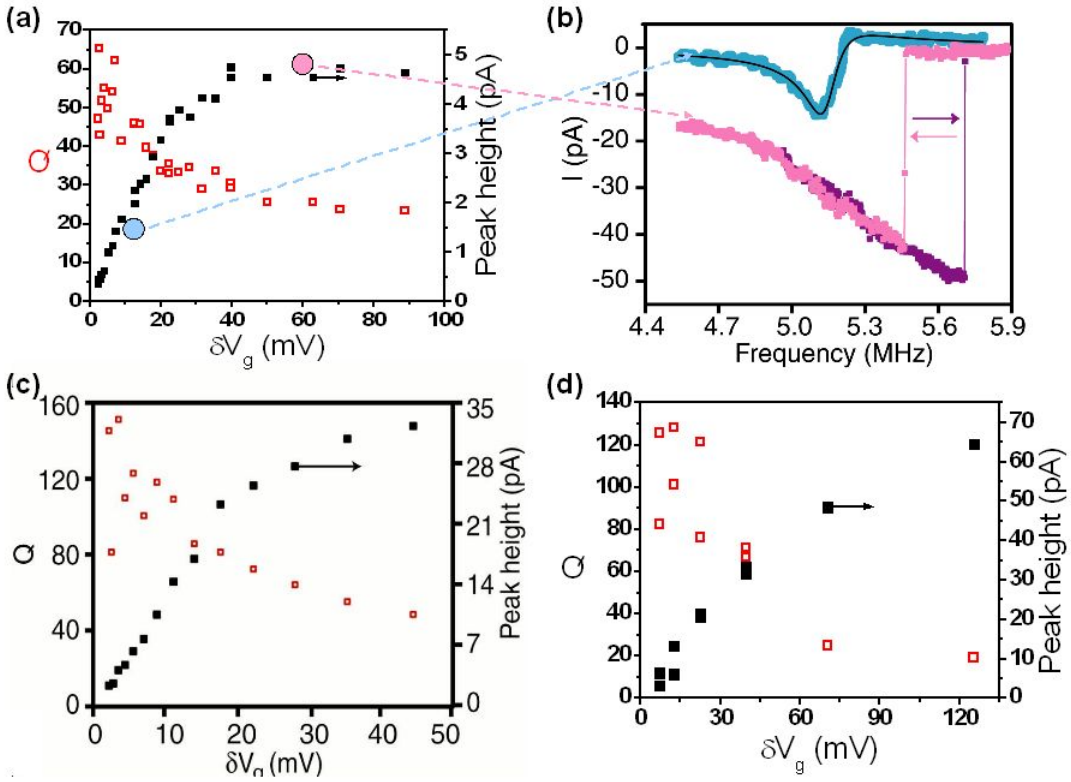

Figure 6.5: Quality factor dependence on the driving voltage. **(a), (c), (d)** Q and the height of the resonance peak for several devices are shown in red open squares and black solid squares, respectively, as a function of driving voltage. Linear behavior is observed at low voltages, but the peak width decreases and the height of the peak saturates at higher driving voltages. **(b)** Trace of detected current vs. frequency with the background signal subtracted for a device at two different driving voltages, $V_g = 8.8$mV and $V_g = 40$mV. The solid black line is a Lorentzian fit to the low bias data. The traces of the current as the frequency is swept up and down are shown in purple and magenta, respectively. Hysteretic switching can be observed.

voltages, the quality factor is independent of the driving voltage, despite the large scattering in the data; at higher voltages, non-linear effects become important and the resonant peak shape deviates from a Lorentzian.

6.3 Temperature dependence results

The temperature dependence of the quality factor can give further insight into the origin of losses in our system. As the temperature of the system is lowered, the overall behavior of the system changes in a very complex manner, as illustrated in Figs. 6.6, 6.7, 6.9. We observe temperature dependence in all measurable quantities: the resonant frequency dispersion curves, the amplitude response to the increasing driving amplitude, and the quality factor dependence on the gate voltage. We first address the overall behavior of the system and then describe in detail the temperature dependence of the quality factor.

Resonance frequency

Figures 6.6a and b show the resonant frequency dispersion curves at different temperatures for the two devices shown in Figs. 6.4. For the device in panel a, we see that the zero gate voltage frequency increases as the temperature is lowered; at the same time, the shift to the linear dispersion is pushed to higher and higher gate voltages. Empirically, we can describe this as a resonant frequency increase in the bending regime with temperature, illustrated in Fig. 6.6c. For the device in panel b, there is no observable change in the resonance frequency as the temperature is lowered. Figure 6.6d shows the resonance frequency as a function of temperature for several other devices at a particular value of the DC gate voltage and driving voltage. Here again we observe a consistent, but variable in magnitude, shift to

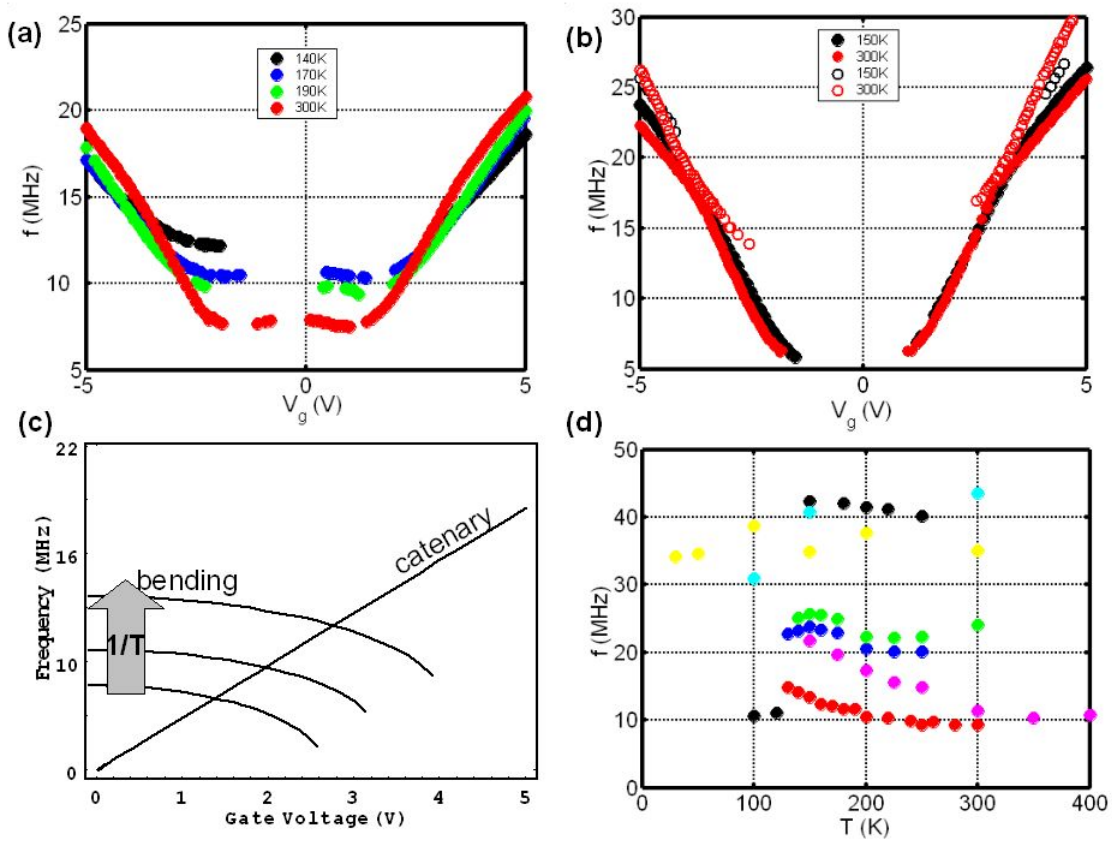

Figure 6.6: Temperature effects on the dispersions. **(a), (b)** Resonant frequency dispersion curves taken at several different temperatures for the devices shown in figures 6.4a and b. For the device in panel a, we see that the zero gate voltage resonance frequency is shifting upwards as the temperature is decreased. **(c)** A schematic for the bending mode frequency shifting upwards with lowered temperature and the catenary regime frequency staying constant. **(d)** Extracted resonance frequency for some value of the DC and driving gate voltages for all the measured devices. Note the constant upward shift with decreasing temperature.

higher frequencies as the temperature is lowered.

Quality factor dependence on the gate voltage

Figure 6.7 shows the corresponding quality factor dependence on DC gate voltage. For the device in panel a, we again observe two major trends. The first is an overall increase in the value of Q. The second is a consistent shift to higher gate voltages of the prominent features in the Q vs. $V_{\mathrm{g}}^{\mathrm{DC}}$ dependence, such as the peak in the Q vs. V_{g} curve.

Since both the dispersions and the Q vs. $V_{\mathrm{g}}^{\mathrm{DC}}$ dependence change with temperature, we would like to correlate the two. In the previous section we saw that the quality factor changed its behavior at points where the dispersion behavior changed, i.e. at the inflection points. We can bring out this correlation by plotting side by side the loss and the derivative of the dispersion with respect to the gate voltage, $\frac{df_0}{dV_{\mathrm{g}}^{\mathrm{DC}}}$. This plot at different values of temperature for both of the devices is shown in Fig. 6.8. For simplicity, we show only the positive gate voltage side. Concentrating on panel a, we see that indeed the loss mimics the qualitative behavior of the resonance frequency dispersion curve, for all of the values of temperature. As the peak in the derivative shifts to higher gate voltages, so does the peak in the loss.

For the device in panel b, we also see an overall increase in the values of the quality factor, and perhaps a slight shift to the higher gate voltages of the crossing position. The relation between the dispersion and the quality factor is again more visible on the dispersion derivative and loss vs. gate voltage plot, Fig. 6.8b. Here we see that the gate voltage where the quality factors are equal ($V_{\mathrm{g}}^{\mathrm{DC}} \approx 3\mathrm{V}$) coincides with the point where the two slopes are equal, which is also the point of

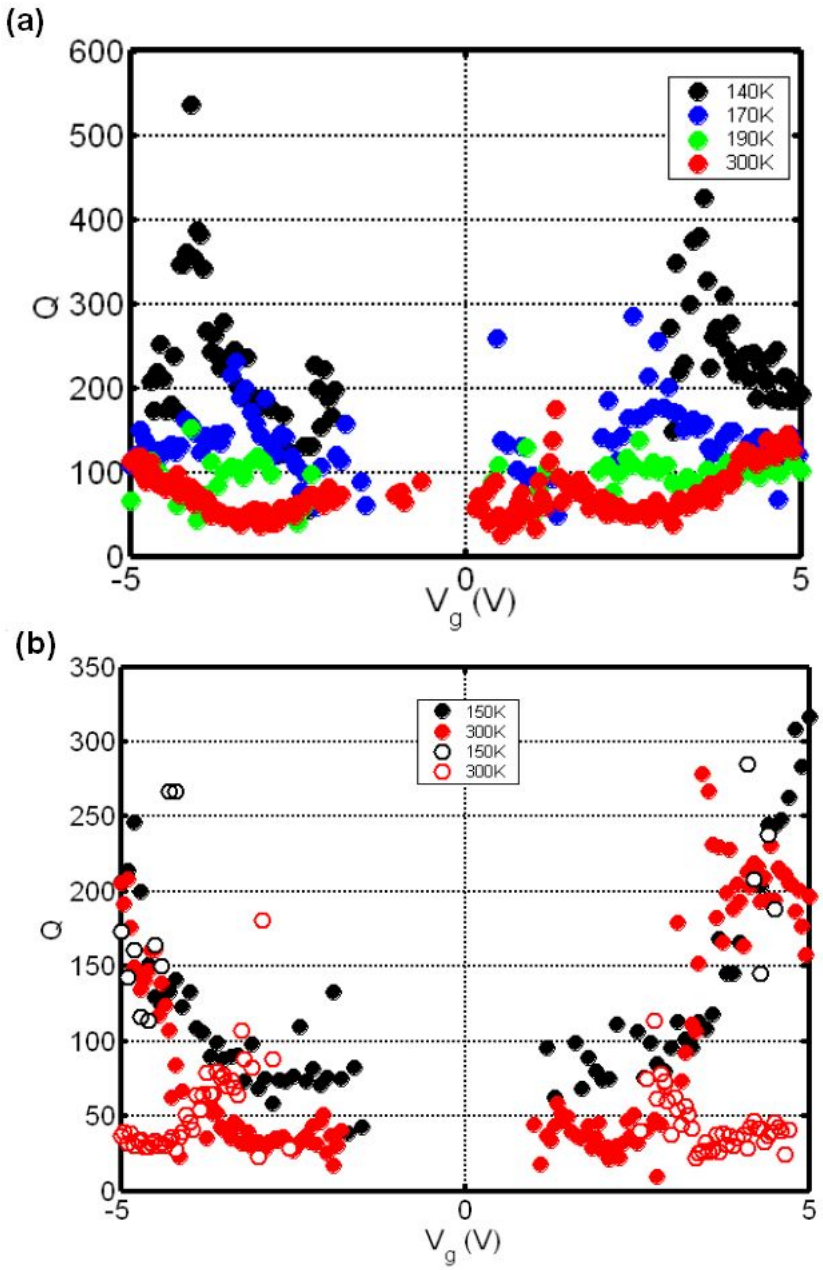

Figure 6.7: Temperature effects on quality factor gate voltage dependence. **(a), (b)** The corresponding Q's vs. DC gate voltage for the same two devices as in Fig. 6.6a, b. While Q exhibits a complex dependence on both temperature and gate voltage, we still notice an overall increase in the values at lower temperatures and a consistent shift outwards of the prominent features in the dependence.

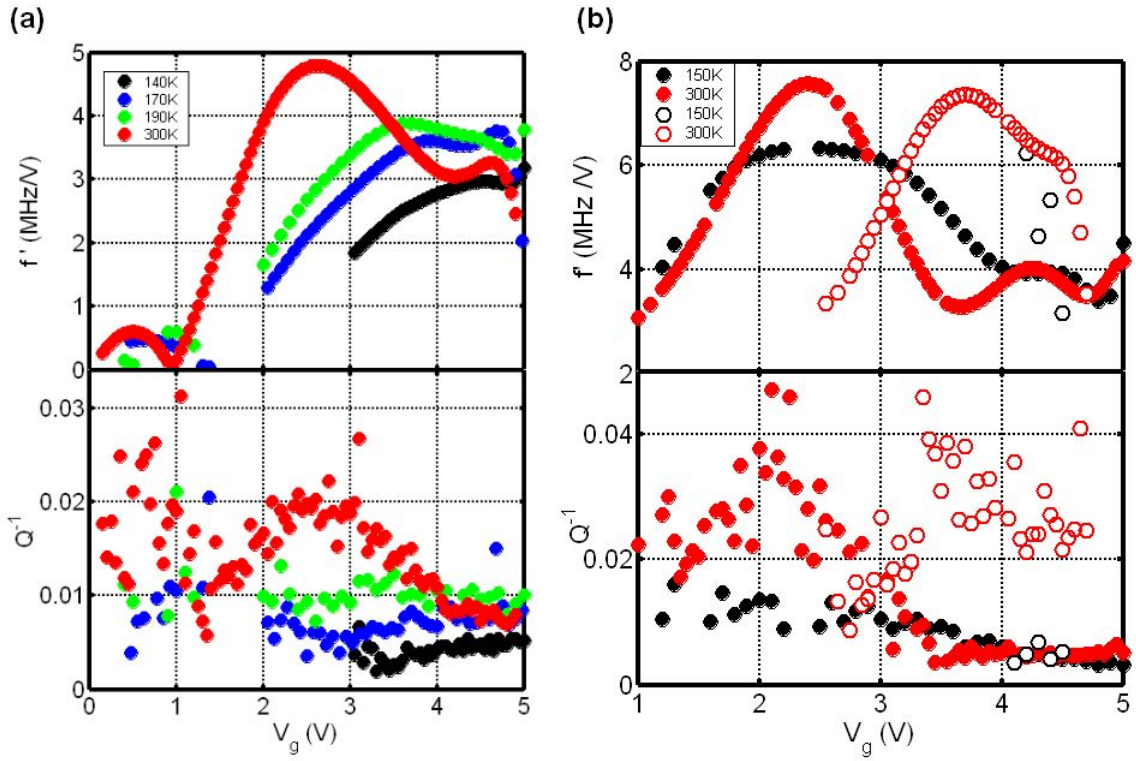

Figure 6.8: Quality factor and the derivative of the resonance frequency dispersion. **(a, b)** The numerical derivative of the resonance frequency dispersion curve (upper panel) and the corresponding loss (lower panel) vs. DC gate voltage for the same two devices as shown on Figs. 6.4, 6.7 for several value of temperature. We see that the loss mimics the behavior of the derivative.

crossing. The overall resemblance between the dispersion derivative and the loss is quite evident.

Quality factor dependence on the driving voltage

Finally, Fig. 6.9 shows observed changes in the quality factor dependence on the driving voltage, $\tilde{V}_{\mathrm{g}}$. We see that again there is an overall increase in the value of Q at lower temperatures. At the same time we see that while at room temperature Q is independent of $\tilde{V}_{\mathrm{g}}$, at lower temperatures, the Q develops a dependence on the driving voltage that we have so far attributed to non-linear effects in the resonator (section 5.4). The dependence is stronger for lower temperatures, such that at lower temperatures the linear regime of a resonator becomes increasingly difficult to attain. Figure 6.9b and d show the same data as the loss dependence on the driving voltage. We see that the loss, Q^{-1}, varies linearly with $\tilde{V}_{\mathrm{g}}$. The strength of this dependence varies between the samples.

6.4 Extracting the quality factor dependence on temperature

Because of the complexities described above, assigning one representative value for the quality factor at a given temperature is difficult. To eliminate the effects of the DC gate voltage and driving voltage, we adopted three different procedures. The first is extracting the representative value of Q from the driving voltage dependence measurements. In this procedure, for a particular temperature we assign the Q measured at the lowest driving voltage that produces a measurable signal. The extracted quality factors for all of the measured devices with this method are shown in Fig. 6.10a, as Q^{-1} vs. T.

The second procedure is extracting the representative value of the Q from the

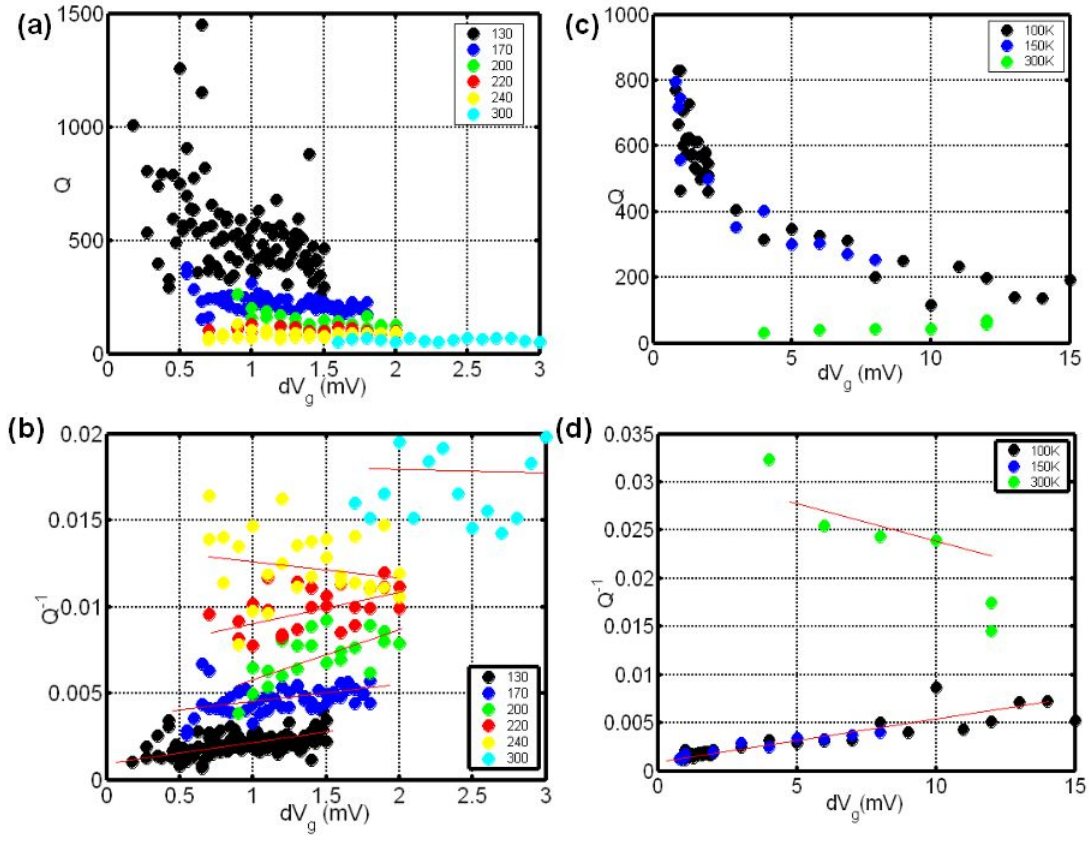

Figure 6.9: Temperature effects on quality factor gate voltage dependence. **(a),(c)** Quality factor dependence on the driving voltage for two different devices for several values of temperature. We see the overall increase of Q at lower temperatures and the development of the the dependence of the Q on the driving voltage. **(b),(d)** Loss dependence on the driving voltage for the same two devices. Note the linear dependence on the driving voltage indicated by linear fits through the data (in red)

.

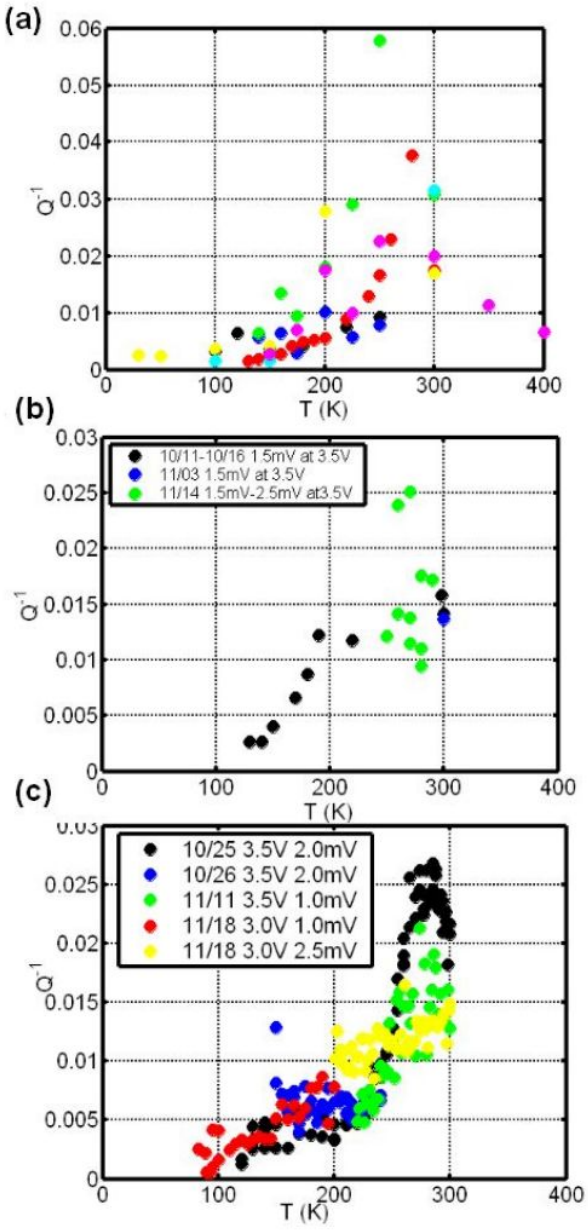

Figure 6.10: Quality factors as a function of temperature for all of the measured devices extracted with three different methods. **(a)** Q was extracted from the Q vs. $\tilde{V}_{\rm g}$ dependence at the minimum detectable driving voltage. **(b)** Q was extracted from the Q vs. $V_{\rm g}^{\rm DC}$ dependence at a particular value of the DC gate voltage. **(c)** Q was measured as a function of temperature, at a particular value of driving voltage and DC gate voltage. Note the presence of a peak in loss at 280K for all three figures.

DC gate voltage dependence measurements. In this procedure, the Q is extracted at a particular value of the gate voltage as a function of temperature. The resulting Q^{-1} vs. T dependence for this method is shown in Fig. 6.10b, for the only device (from Fig. 6.4a) where this method was applicable.

The last method is directly measuring Q as a function of temperature at the lowest detectable driving voltage, at a constant value of the DC gate voltage. The result is shown in Fig. 6.10c, for the only device (from Fig. 6.4a) where this measurement was performed.

We see that for all the methods and all the devices, there is an increase in the value of Q at lower temperatures, in some cases by as much as an order of magnitude. In most devices we also see a dominating peak in the loss around 280K. This is particularly visible in Fig. 6.10a and c. For the device shown in Fig. 6.10c, the peak disappeared after several days of measurement and could not be brought back by either introducing air[1] or water[2] into the chamber.

We performed a several hour bake-out in vacuum at 350K and several day bake-out at 400K on another sample (indicated by magenta in Fig. 6.10a). The heating did not result in any significant changes in the room temperature value of Q.

6.5 Empirical model

Summarizing our findings above, we can say that three major trends were observed as the temperature was lowered. First, the value of the quality factors increased. Second, the quality factor dependence on gate voltage changed consistently with

[1]The chamber was left in ambient pressure overnight.

[2]A wet napkin was introduced into the chamber over the weekend at ambient pressure.

the resonance mode dispersions. The loss mimicked the behavior of the resonance frequency derivative. Lastly, the loss developed an increasingly stronger linear dependence on the driving voltages. Below we discuss these findings.

DC gate voltage dependence

The DC gate voltage, $V_{\mathrm{g}}^{\mathrm{DC}}$, controls the resonant frequency of a particular mode by controlling the tension in the tube (see section 4.4 for details). Naively, for frequency-independent loss mechanisms, we expect the quality factor to increase with the increasing frequency, as the energy of the resonator increases and the loss stays constant. The similarity between the dispersion derivative and the Q's behavior, though unexpected, points to the need for understanding the details of the resonance frequency dispersions.

Pragmatically, we can build an empirical model for Q^{-1}, without understanding the underlying reasons for this behavior. Since we observed similarities between the loss and the derivative of the frequency dispersion, we fit the Q^{-1} vs. $V_{\mathrm{g}}^{\mathrm{DC}}$ curve to the numerical derivative of f_0 vs. $V_{\mathrm{g}}^{\mathrm{DC}}$ as:

$$Q^{-1} = a_1 \frac{df_0}{dV_{\mathrm{g}}^{\mathrm{DC}}} \tag{6.1}$$

The result of the fit can be seen in Fig. 6.11 for the two devices shown previously in Fig. 6.7. The prefactor, a_1, comes out to be approximately 3×10^{-9}. Its behavior with temperature is shown in Fig. 6.13a and will be addressed later.

Any low-frequency noise that can result in the modulating of the resonance frequency would cause an inhomogeneous broadening of the response peak. Also, coupling to external systems with out-of-phase response would lead to the same effect. This broadening Δf would have the same functional form as given by Eq. 6.1.

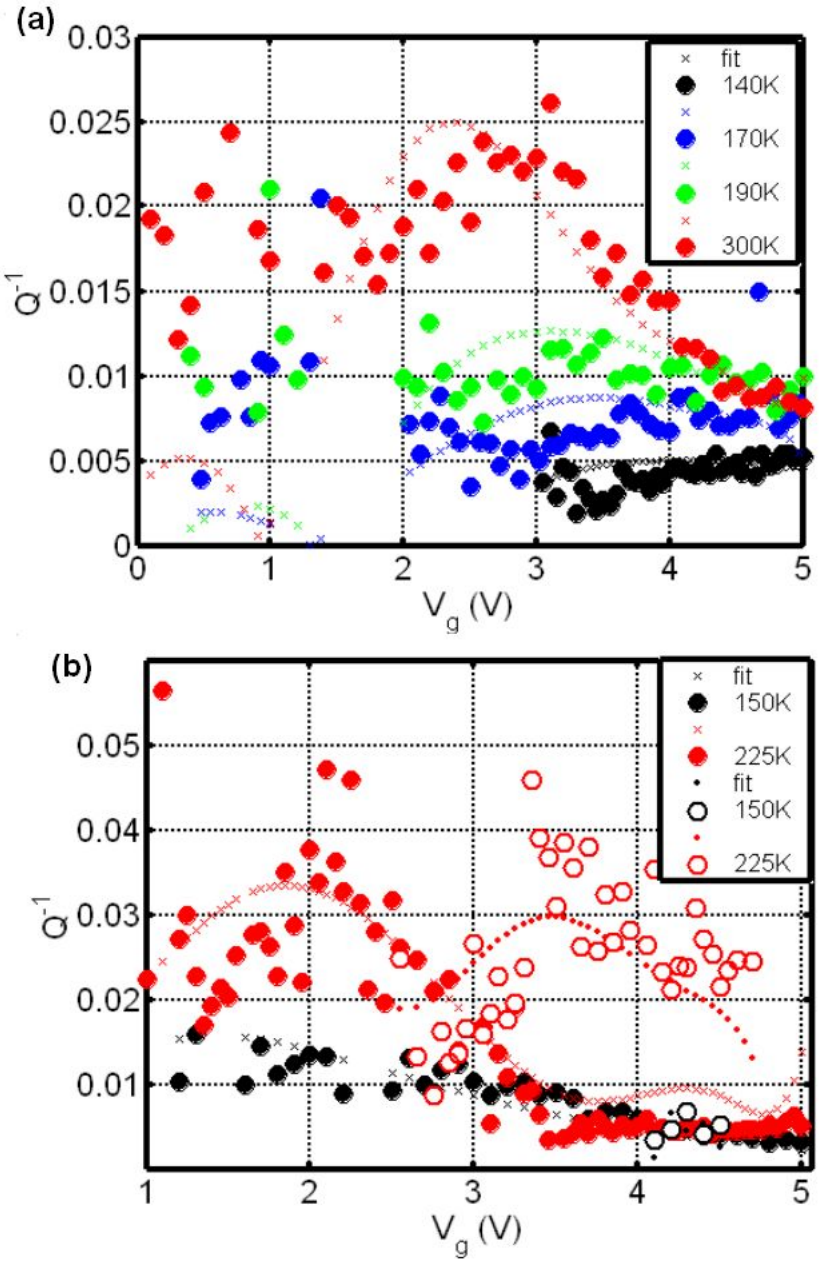

Figure 6.11: Fitting Q^{-1} dependence on the DC gate voltage. **(a)**,**(b)** Loss (solid circles) vs. the DC gate voltage at several different temperatures for the same two devices as in Fig. 6.4 and their respective fits (crosses and dots). The loss was fitted to the $a_1 f'$ functional form.

The parametric nonlinearity model described in section 5.4, where the resonance frequency is modulated directly by the driving voltage, might also lead to similar effects. Ro know the functional dependence of the broadening in the case of parametric nonlinearity, a more accurate, numerical solution of the model given by Eq. 5.17 is needed.

Driving voltage dependence

The driving voltage, $\tilde{V}_{\mathrm{g}}$, controls the AC force driving the resonator. As discussed in the previous chapter (see section 5.4), for small voltages, we expect the resonator to be in the linear regime and the quality factor to be independent of the driving voltage. In our measurements we observed that as the temperature decreases, a linear dependence of the loss on the driving voltage develops. This developing dependence can be empirically described as

$$Q^{-1} = b_1 \tilde{V}_{\mathrm{g}} + b_2 \tag{6.2}$$

The behavior of slopes, b_2, and intercepts, b_1 from a fit of the device shown in Fig. 6.9a as a function of temperature is shown in Fig. 6.13b and c.

The nonlinear loss behavior shown in Fig. 6.9 is very different from the nonlinearities that we observed at room temperature shown on Fig. 6.5, and from the simple model of a Duffing oscillator (see section 2.4). First, we expect Q vs. $\tilde{V}_{\mathrm{g}}$ to exhibit both a driving voltage independent plateau (linear regime) and a driving voltage dependent (non-linear regime) region in loss, as was the case for room temperature measurements. Instead, we see either an absence of any loss dependence on driving voltage or a linear dependence with a variety of slopes. Second, in the non-linear region, we expect the shape of the signal to deviate from a Lorentzian, as in the room-temperature case shown in Fig. 6.5b. For the low temperature non-

linearity, however, the shape of the signal remains Lorentzian. Also, for a typical Duffing resonator, the resonance frequency of the peak is expected to shift to higher frequencies for a hardening non-linearity, and to lower frequency for a softening non-linearity. We, however, observe an inconsistent behavior among the samples, with resonance frequencies shifting either up or down in different samples.[3]

It is feasible that the solution to the parametric nonlinearity model defined by Eq. 5.17 gives a driving voltage dependent broadening, as the driving voltage would define how much frequency is modulated. The exact functional form of this dependence can not be extracted without fully solving the model.

Temperature dependence

Figure 6.12a reproduces the results with the three methods that we described in section 6.4.[4] Panel b zooms in on the data. We see a strong temperature dependence of the loss. The dependence consists of two parts: a peak in the loss at 280K, and a temperature-dependent background. It is difficult to separate the two, as we do not know the exact functional dependence of the peak, and, thus, can not be certain that we are not measuring the peak's tail. We try to eliminate the contribution of the peak by concentrating on the data where the peak is no longer visible (shown in green in Fig. 6.12). Phenomenologically, we can fit the loss with either a linear or a quadratic dependence on temperature, indicated by

[3]We must note that one possibility is that this shift is not due to the the non-linearity, but rather to a drift of the effective DC potential of the tube, i.e., its tension.

[4]For simplicity we only combined a few of the curves from each method.

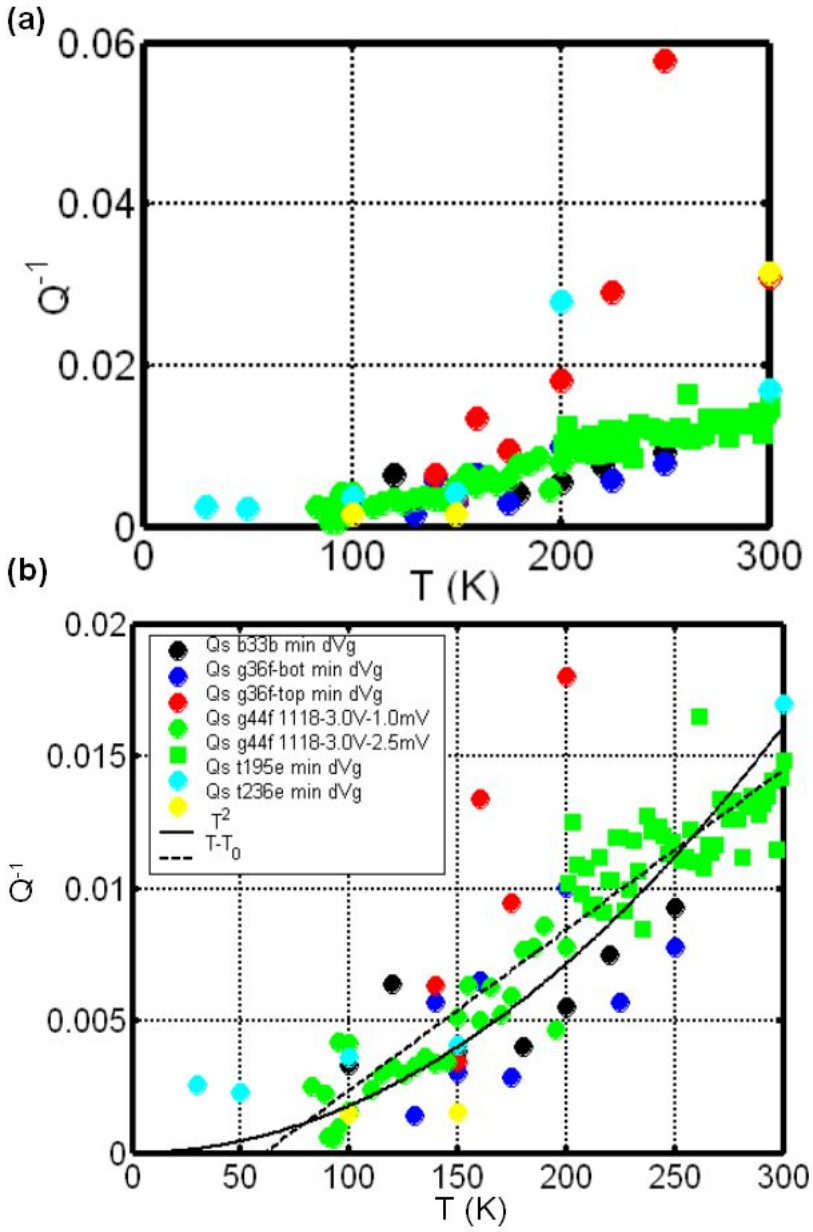

Figure 6.12: An extracted loss as a function of temperature for all of the measured devices, **(a)**, and a zoom in, **(b)**. Various datasets collected with the three different methods shown in Fig. 6.10 were combined. Not all of them were selected to avoid cluttering. A linear (dashed line) and a quadratic (solid line) fits are superimposed on the data in panel **(b)**.

a dashed and a solid line, respectively, in Fig. 6.12b.

$$\begin{aligned} Q^{-1} &= c_1(T - T_0) \\ Q^{-1} &= c_2 T^2 \end{aligned} \tag{6.3}$$

The linear fit of the data shown in green yields $c_1 = 6.3 \times 10^{-5}\mathrm{K}^{-1}$, $T_0 = 72\mathrm{K}$, and the quadratic fit yields $c_2 = 1.8 \times 10^{-7}\mathrm{K}^{-2}$

Finally we can also look at the temperature dependence of the fitting coefficients. Figure 6.13 shows results for a_1, b_1, and b_2 from the last two sections. Both a_1 and b_2 show a peak around 280K. For a_1, the underlying temperature dependence is roughly constant, while for b_2, the background changes with temperature, in a fashion similar to the data from Fig. 6.12. b_1 does not show any strong temperature dependence, but due to large scattering in the data, it is hard to interpret.

Ideally, we would like to combine the empirical findings given by Eqs. 6.1, 6.2, and 6.3 into one model. Unfortunately, to investigate the relation between the three sets of coefficients a_1, b_1 and b_2, and $c_{1,2}$ a complete dataset of Q^{-1} vs. T, $\tilde{V}_\mathrm{g}$, and V_g^DC is necessary. With current data, which contains only specific cuts through this data set, we can not confidently combine these results into one model.

6.6 Theoretical discussion of possible loss mechanisms

In order to understand these findings we go back to section 2.6, where we have described common dissipation sources in NEMS. We can examine these mechanisms one-by-one to see if their predictions are consistent with our measurements. We begin our discussion with the extrinsic mechanisms applicable in our system: air friction, clamping, and ohmic losses. We then move on to the intrinsic mechanisms: surface losses and phonon-phonon interactions. Table 6.1 summarizes the

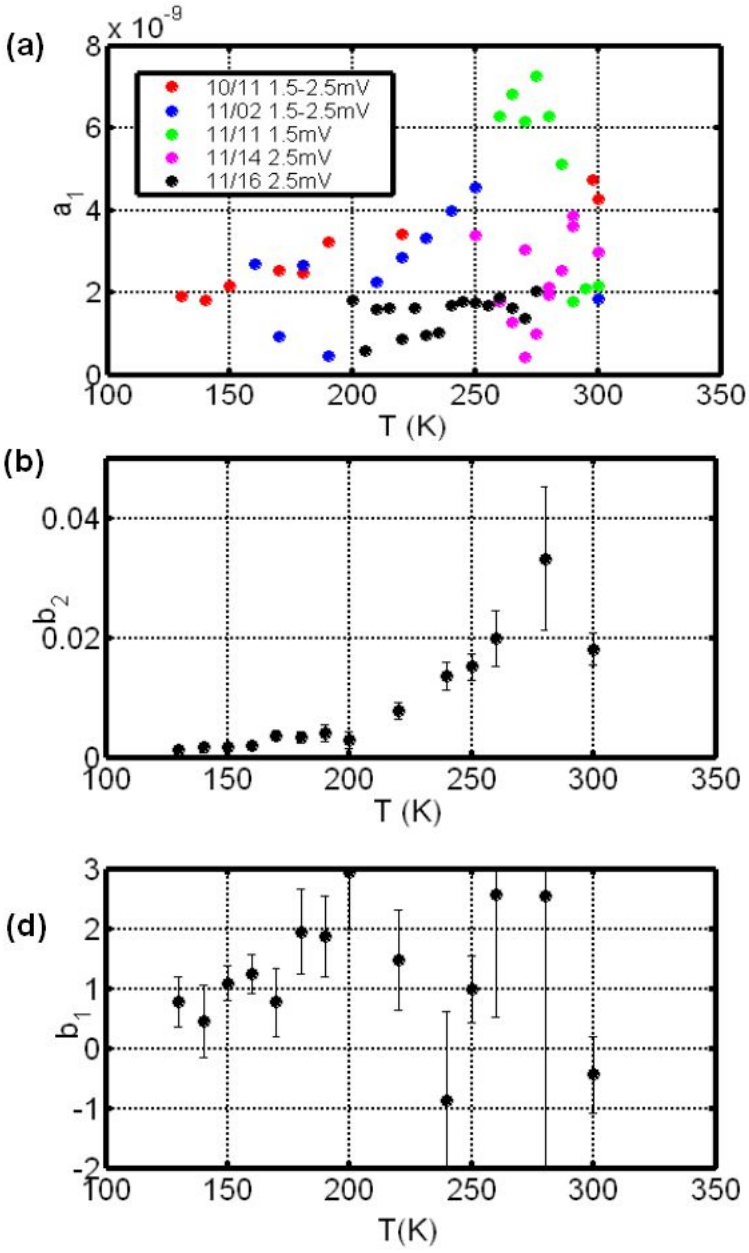

Figure 6.13: Fitting parameters; temperature dependence from a device shown in Fig. 6.4a. **(a)** a_1 from the fits of $Q^{-1} = a_1 f_0'$ shown on Fig. 6.11a. **(b), (c)** Fitting parameters b_1 and b_2 from the $Q^{-1} = b_1 \tilde{V}_g + b_2$ fits shown on Fig. 6.9b. Note the presence of a peak at 280K for a_1 and b_2.

Table 6.1: Calculation of various dissipation processes for a standard CNT. We see that none of the extrinsic mechanisms typically limiting the performance of the resonator could dominate the losses.

Dissipation Process	Q^{-1}	**Q Value**
Air friction	$\frac{p(2\pi r^2 L)}{m\omega_0\sqrt{3k_BT/m_{\mathrm{N}_2}}}$	4×10^7
Clamping	$\left(\frac{t}{L}\right), \left(\frac{t}{L}\right)^3, \left(\frac{t}{L}\right)^5$	$10^3, 10^9, 10^{16}$
Ohmic	$\frac{(C'V)^2}{\pi kC}\left(\frac{\omega_0\tau}{1+(\omega_0\tau)^2}\right)$	10^5
Thermoelastic effect	$\frac{\alpha^2 TE}{c}\left(\frac{\omega_0\tau}{1+(\omega_0\tau)^2}\right)$	400

calculated contributions to dissipation (Q^{-1}) for a typical CNT device (table 4.1). We discuss them in detail below.

6.6.1 Extrinsic losses

We observed no quality factor dependence on pressure at the experimental vacuum levels ($< 10^{-4}$torr). This is consistent with the calculations of Bhiladvala and Wang (2004) for the quality factor of doubly clamped beams, which predict the interval of large losses due to air friction at pressures of $1 - 10$torr, and consecutively, negligible losses at the experimental vacuum levels. We can thus eliminate air friction as a relevant dissipation source in our experiment.

In section 2.6 we were given three different expressions for the dissipation due to clamping. Using each of these, we calculate the upper bound on the quality factor to be $Q_{\text{clamping}} < 10^3, 10^9, 10^{16}$, respectively; at least an order of magnitude higher than observed. Also, we observed similar quality factors in devices with three different geometries (see Fig. 6.2d), and thus with very different clamping and different expected levels of dissipation. This argues against clamping losses as an important source of dissipation.

If ohmic loss dominated, we would expect lower quality factors from the devices with higher resistances. In our samples there was no correlation between the electrical resistance of the device and the measured quality factor (see Fig. 6.2a). We can also calculate the expected dissipation from this mechanism, using Eq. 2.69 with the typical CNT parameters (table 4.1), which yields the upper bound on the quality factors of $Q_{\text{ohminc}} < 10^5$. We can thus eliminate ohmic losses as the largest dissipation source.

Residues from processing and other contamination of the CNT could also pro-

vide a mechanisms for dissipation. However, devices produces with the third method yield clean devices, as the CNT is grown last and does not undergo any processing, and thus should give higher Q's. As we do not observe any systematic difference between the devices created with different methods, we conclude that contamination is not likely to be the dominant dissipation source in our system.

6.6.2 Intrinsic losses

Among the intrinsic losses, the possible dissipation sources are phonon-phonon interactions, electron-phonon interactions and surface losses. Naively, we expect losses associated with surface effects to be negligible for CNT resonators, as CNTs have well terminated bonds on the surface. But, as illustrated in Fig. 6.1b, the quality factors observed in CNT resonators follow the linear trend in the Q vs. device volume dependence observed with MEMS and NEMS. Such a trend is typically attributed to surface-related loss mechanisms, as the surface-to-volume ratio increases for smaller structures.

The large dissipation peak at 280K could also be attributed to the losses in the surface water layer. Similar peaks have been observed in the dissipation dependence on temperature (Hutchinson et al., 2004) and are typically attributed to Debye type losses with a thermally activated process (see section 2.6). To correctly extract the attempt time and the activation temperature, a complete measurement of the peak for samples with different vibration frequency is needed. Our data, unfortunately, does not allow us to accurately extract these parameters. We can say from the position of the peak, however, that the activation temperature is around 280K, suspiciously close to the freezing temperature of water.

Further experiments, in particular mapping out the position of the peak in

temperature as a function of the gate voltage (i.e., resonance frequency) are needed to investigate its exact nature. Repeating the experiments after passing a sufficient DC current through the CNT to heat it up and evaporate the water layer on the CNT would also provide valuable information on the relation of the peak to water.

Surface losses are then a possible source of dissipation. It is not clear that surface effects can also explain the observed loss dependence on the gate voltage and derivative of the dispersion. So, we conclude that even though surface losses are likely to be an important source of dissipation, there are other mechanisms that also contribute to the overall dissipation.

Phonon-phonon interactions set the fundamental limit on the resonator's performance. Levels of dissipation close to this limit have been achieved in Si NEMS (Roszhart, 1990, Yasumura et al., 2000).

The geometry of our system differs from the typical NEMS geometry for which the standard thermoelastic theory (see section 2.6) was developed. First, as CNTs are initially slacked, their profile is a catenary (see section 4.3). The motion during a vibration is not the pure flexural motion that it is for NEMS. Second, unlike in NEMS, the CNT is under tension, defined by the DC gate voltage. These difference make the standard thermoelastic effect not directly applicable to our system; however, given the lack of a theory that captures all of the nuances, we use the existing models.

Depending on the length of the phonon mean free path compared to the size of the system, thermoelastic losses manifest themselves as either the *thermoelastic effect* (diffusive limit) or the *Landau-Rumer effect* (ballistic limit). In NTs, the measured length of the acoustic phonons is on the order of $0.5 - 1\mu$m (Kim et al., 2001). As our device lengths are on the same order of magnitude, we treat the

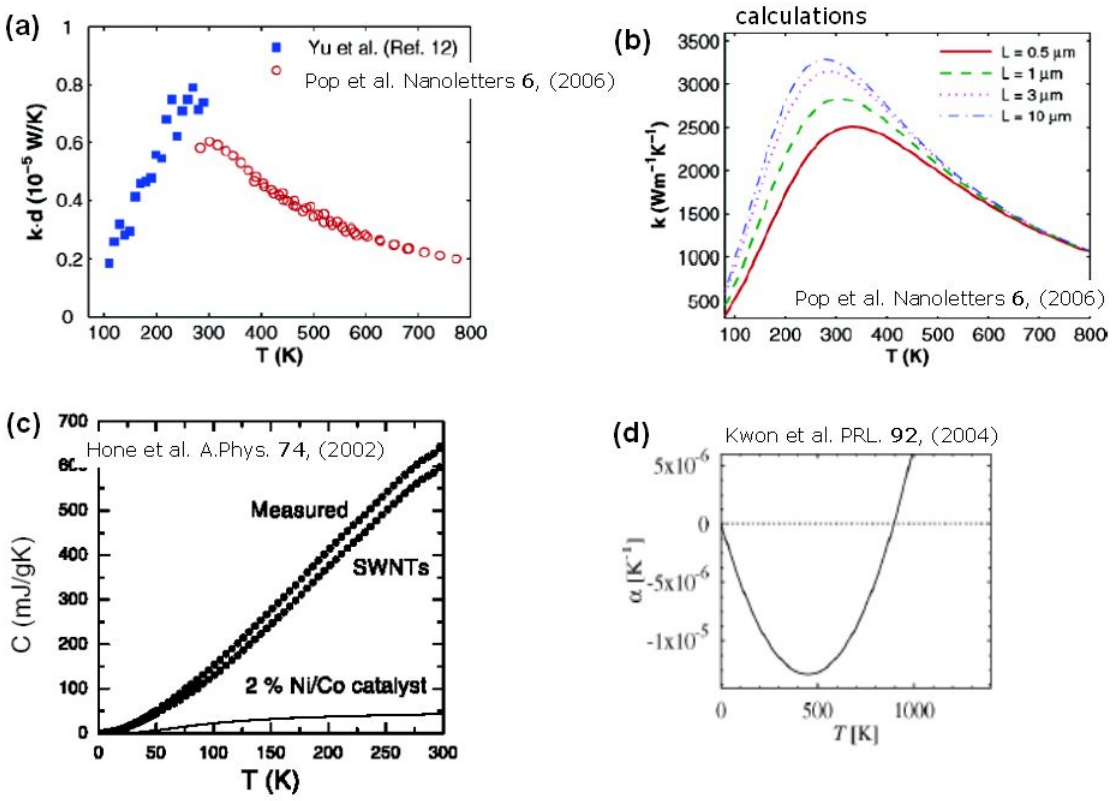

Figure 6.14: Thermal parameters of CNT extracted from literature. **(a), (b)** thermal conductivity κ from (Pop et al., 2005). **(c)** heat capacitance c from (Hone et al., 2002) **(d)** Calculations for the thermal expansion coefficient α from (Kwon et al., 2004).

phonon-phonon losses in our system in the framework of thermoelastic effect (see section 2.6). The degree of loss associated with thermoelastic effect is given by Eq. 2.51, which we reproduce here for convenience.

$$Q^{-1} = \frac{\alpha^2 TE}{C}\left(\frac{\omega\tau}{1+(\omega\tau)^2}\right) \tag{6.4}$$

The first factor, the dissipation strength $\alpha^2 TE/C$, defines the possible maximum loss due to this mechanism. Using the values for $\alpha = 1.5 \times 10^{-5}\mathrm{K}^{-1}$ (Kwon et al., 2004), $\kappa = 2500\mathrm{W/mK}$ (Kim et al., 2001, Pop et al., 2005), $E = 1\mathrm{TPa}$, and $C = 600\mathrm{mJ/gK} \times 2300\mathrm{kg/m}^3$ (Hone et al., 2002) found in the literature, we calculate a lower bound of $Q_{\mathrm{thermoelastic}} > 20$ at room temperature. To extract the temperature dependence we note that α, κ and C have linear temperature dependence in the region of interest (Kwon et al., 2004, Kim et al., 2001, Pop et al., 2005, Hone et al., 2002) (see Fig. 6.14), and using Eq. 6.4, we conclude that

$$Q^{-1} \sim T^2 \tag{6.5}$$

which is consistent with our measurements.

The second factor in Eq. 6.4 defines the relative time scales for heat and strain. Here τ is the characteristic time for heat transfer between the points of maximum and minimum strain. Our vibrations are neither purely flexural nor purely longitudinal. We can calculate the characteristic time scales for both effects. For flexural vibration, τ is given by the diameter, d, of the CNT and the heat diffusion constant.

$$\tau = \frac{dC}{(\pi)^2\kappa} \tag{6.6}$$

This model yields a dissipation time of 1ps, many orders of magnitude smaller than the time for one oscillation, $1/f = 20\mathrm{ns}$. Thus, this model does not lead to significant losses.

For longitudinal vibrations, the resonance wavelength for the n^{th} harmonic for a typical device of length $L = 1.75\mu$m is given by $\lambda_n = 2L/n = 3.5\mu$m/n. τ is then given by the mode wavelength and the heat diffusion constant (Eq. 2.53):

$$\tau = \frac{\lambda_n^2 C}{(2\pi)^2 \kappa} \tag{6.7}$$

For a finite DC gate voltage, our CNT resonators are typically under tension, which means that during an oscillation all of the tube is strained and thus the extra heat has to flow in from the contacts due to the lack of the compressed regions in the tube. For a tensed string model τ is then given by

$$\tau = \frac{L^2 C}{(\pi)^2 \kappa} \tag{6.8}$$

For the fundamental mode, both of these models lead to the same result. The characteristic time dissipation is then 2ns, comparable to the time for one oscillation $1/f = 20$ns. Using Eq. 6.4, this yields $Q_{\text{TED}} \approx 400$ for a typical device at room temperature. Assuming the same linear temperature dependencies as above, we find that for both models τ is independent of temperature, and thus the temperature dependence of Q is given solely by the dissipation strength term.

For typical resonance frequencies ($f = 50$MHz) $\omega\tau \leq 1$, the time-scales factor of the loss reduces to $\frac{\omega\tau}{1+(\omega\tau)^2} \approx \omega\tau$. Equation 6.4 reduces to either

$$Q^{-1} = \frac{\alpha^2 T E}{(2\pi)^2 \kappa} \omega_n \left(\frac{2L}{n}\right)^2 \tag{6.9}$$

for the "longitudinal" model or

$$Q^{-1} = \frac{\alpha^2 T E}{(2\pi)^2 \kappa} \omega_n L^2 \tag{6.10}$$

for the "tensed string" model.

For a given resonance mode, we expect the loss to increase with the increasing vibration frequency (i.e., with increasing DC gate voltage) as the strain is modulated faster, while the heat flow time remains the same. This hold for both models. The time scales for heat flow and one vibration become closer to each other, and the amount of loss increases.

$$Q^{-1} \sim \omega_n(V_{\mathrm{g}}^{\mathrm{DC}}) \sim V_{\mathrm{g}}^{\mathrm{DC}} \tag{6.11}$$

The loss dependence on the mode number at a given DC gate voltage is different for the two models above. For the longitudinal model, the resonance frequency increases with the mode number, $\omega_n \sim n$, and thus the strain is modulated faster. At the same time, though, the number of nodes increases proportionally, decreasing the heat flow time. We expect the loss factor to decrease with the mode number n.

$$Q^{-1} \sim \frac{\omega_n}{n^2} \sim 1/n \tag{6.12}$$

For the tensed string model we expect the opposite behavior, since the heat path does not change for different modes, but the vibration frequency does.

$$Q^{-1} \sim \omega_n \sim n \tag{6.13}$$

In our measurement, we observed a complicated, device dependent quality factor dependence on the DC gate voltage that, if anything, points to the increase of the quality factor with increasing gate. We have also observed a correlation of the quality factor with the mode number for most devices, as indicated in Fig. 6.2e, that agrees better with the longitudinal model rather than the tension model.

We see that overall, the loss in CNT resonators can not be explained with a single theoretical model, as different trends in its behavior point to different dissipation mechanisms. First, with few assumptions, the thermoelastic effect predicts

a reasonable value for the dissipation strength in our system, and predicts the correct underlying temperature dependence. However, the relative time scales for the heat flow and vibration are still not understood. Second, the correlation of the loss and the derivative of the resonance frequency dispersion could be attributed to the inhomogeneous noise broadening, but the exact nature of the noise is still under question. Last, some surface-related dissipation processes could account for the presence of the peak in loss at 280K, but the exact process is still unclear. The overall complicated behavior of the loss indicates that no single dissipation mechanism is the dominant one, and that the correct theoretical model is a combination of several mechanisms.

6.7 Conclusion

In this chapter we studied the quality factor in CNT resonators. At room temperature values in the range of $30-200$ were measured, and at low temperatures quality factors increased by an order of magnitude. Values up to $1,000$ were observed. We investigated the quality factor dependence on various device and resonance characteristics. We found no correlation to the device geometry, the device's electrical resistance, or the chamber pressure. We did find, however, a dependence on the resonance mode number, driving voltage, and the DC gate voltage. We also found that temperature had a significant effect on the the behavior of the system, and led to a large increase of the quality factor values.

From these dependencies we extracted that Q changed linearly with the mode number, that Q^{-1} had the same DC gate voltage dependence as the derivative of the frequency dispersion curve ($Q^{-1} \sim f'$), and that Q^{-1} depended linearly on the driving voltage ($Q^{-1} \sim \tilde{V}_{\rm g}$). We also observed a peak in the dissipation at

280K that could not be correlated with the changes in either the dispersion or the driving voltage. The underlying temperature dependence of Q could be fit to either a linear ($Q^{-1} \sim T - T_0$), or to a quadratic ($Q^{-1} \sim T^2$) dependence.

After considering several dissipation mechanisms, we concluded that the overall values of the Q's and their temperature dependence point to the presence of several dissipation mechanisms of comparable strength. We identified the surface effects, inhomogeneous response broadening, and thermoelastic effect as the possible key players, but more work needs to be done to confirm this.

CHAPTER 7

CONCLUSIONS

7.1 Summary

We have demonstrated the first tunable self-detecting carbon nanotube resonator. We investigated the resonator frequency tunability, the limits on the resonator's performance, and the origin of losses in the resonator.

To perform these measurements, we designed a fabrication procedure described in Chapter 3 that resulted in suspended CNT devices in a transistor geometry. We were able to electrically excite and detect the doubly-clamped CNT vibrational modes using a capacitive actuation and detection scheme in conjunction with a mixing technique described in Chapter 3.

In Chapter 4, we described our results on the resonance frequency tuning with an applied gate voltage. We could understand the behavior of the frequency vs. gate voltage behavior both qualitatively and numerically by modeling the resonator as a slack beam, to which we apply an external uniform downward force set by the DC gate voltage. Depending on the magnitude of the force, the nanotube can enter three different regimes: bending, catenary, and elastic, in each of which a different type of frequency gate voltage dependence is observed.

In Chapter 5, we further analyzed the performance of a CNT resonator and investigated its limitations. We developed a fitting procedure to extract the important parameters of a resonator: the resonant frequency, the quality factor, and the amplitude of the induced resonant current. Using this procedure, we estimated the measured force sensitivity of $1.5\text{fN}/\sqrt{\text{Hz}}$, consistent with theoretical calculations of electron Johnson-Nyquist noise; at temperatures below 1K sensitivities down to

aN/$\sqrt{\text{Hz}}$ should be achievable. We also estimated the upper bound on the resonant frequency detectable by our techniques, limiting ourselves to the fundamental harmonic. We find that at low temperatures devices with lengths down to 30nm, corresponding to resonant frequencies of $\sim$ 150GHz, should produce a detectable signal.

Finally, in Chapter 6, we investigated the losses in CNT resonators. By investigating the quality factor dependence on various parameters, we found a strong quality factor dependence on temperature and a complicated dependence on the mode number, the DC gate voltage, and the driving voltage. At room temperature values in the range of $30 - 200$ were measured, and at low temperatures quality factors increased by an order of magnitude, with values observed up to $1,000$. We were able to empirically fit the loss dependencies on the derivative of the dispersion mode, driving voltage and temperature. After considering several dissipation mechanisms, we concluded that the overall values of the Q's and their behavior point to the presence of several equally important dissipation mechanisms. We concluded that the overall values of the Q's and their behavior point to surface effects, coupling to external systems, and the thermoelastic effect as possible key mechanisms in dissipation. Further investigation is necessary to confirm these findings.

7.2 Future work

The small mass of CNT resonators makes them very attractive for two potential experiments.

The first experiment is to build a mass sensor. The typical mass of a CNT used in our devices is on the order of 7ag. Using Eq. 2.71 for mass sensitivity, we

see that even at room temperature with the quality factors around 70, detecting masses down to 200zg, comparable with the highest sensitivities up-to-date (Ekinci et al., 2004, Ilic et al., 2004), should be possible. At lower temperatures, $T \approx 100$K, the mass sensitivity should increase by at least an order of magnitude as quality factors increase to $1,000$. This yields the smallest detectable mass of 10zg, or only 30 Au atoms.

The second application is to study single electron charging (Woodside, 2001) and quantum mechanical (LaHaye et al., 2004) effects on the mechanical motion of the CNT resonator. At low temperatures, $T < 10$K, a quantum dot can form on the nanotube. The transport through the CNT reduces to single electron charging events, which manifest themselves as oscillations in the conductance as a function of the gate voltage. These oscillations result in improvement of the force sensitivity, as discussed in Chapter 5. They also are expected to affect the mechanical motion of the CNT resonator, causing both a shift in the resonant frequency and an additional dissipation, analogously to the system of a vibrating cantilever on top of a quantum dot, as was studied by Woodside (2001).

Quantum effects become important when the mechanical resonator is cooled further down to its "quantum temperature," $T_{\mathrm{Q}} = \hbar\omega_0/k_{\mathrm{B}}$. For a typical 100MHz resonator, this means cooling to $\sim$ 1mK, which is hardly achievable with current technology. As calculated in Chapter 5, however, the upper limit on resonance frequency detectable with this technique is in the hundreds of GHz. For a few-GHz device, the quantum temperature rises to a few mK, accessible with a dilution refrigerator. To see quantum effects, a displacement sensitivity comparable to the "standard quantum limit," $\Delta z_{\mathrm{SQL}} = \sqrt{\hbar/2m\omega_0}$, is necessary. Since the product of $m\omega_0$ is independent of length, for a fundamental harmonic, the required sensitivity

is $\approx$ 5pm, for either a typical device or a few-GHz device, comparable to what has been achieved in the literature and perhaps feasible with our detection technique for shorter tube-gate distances.

APPENDIX A

BEAM MECHANICS

Let us consider a small section of a bent beam. One side of it is compressed and another side is stretched, which implies that there is line of neutral stress along the length of the beam (See Fig. C.2). Let $\hat{x}$ be the coordinate along the beam, and $\hat{y}, \hat{z}$ the coordinates perpendicular to the beam. For the bending radius of curvature R, the relative elongation of an infinitesimal segment previously of length dx along the beam (or else strain) is given by

$$\epsilon = \frac{dx' - dx}{dx} = z/R \tag{A.1}$$

Using Hooke's law we have that the stress in the beam, σ, is given by

$$\sigma = \epsilon E = \frac{z}{R} E \tag{A.2}$$

where E is the elastic modulus of the beam.

We can define the torque due to the internal stresses in the cross section of the beam. For each area element $d\vec{A}$ there is a force $\sigma d\vec{A}$ acting on it along the $\hat{x}$ direction. The torque created by it with respect to the $\hat{x}$ axis is equal to $z\sigma d\vec{A}$, which means that the total torque about the $\hat{y}$ axis is

$$\vec{M} = \int_A z\sigma d\vec{A} = \frac{E}{R} \underbrace{\int_A z^2 dA}_{I_y} \tag{A.3}$$

where it is useful to define the quantity I_y - the moment of inertia of the beam around the $\hat{y}$ axis.

For small deformations $1/R = d^2z/dx^2$ and thus

$$\vec{M} = -EI_y \frac{d^2 z}{dx^2} \tag{A.4}$$

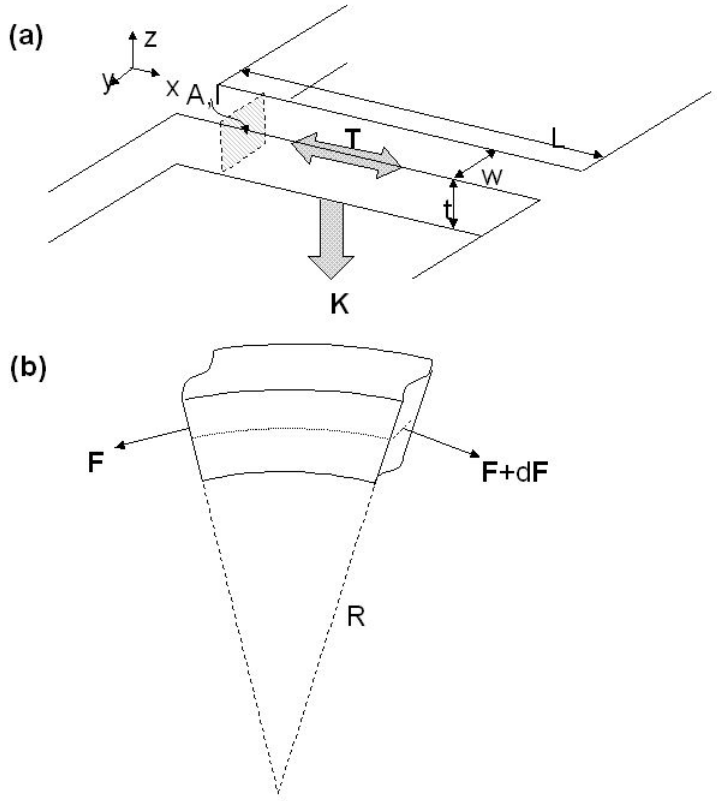

Figure A.1: A schematic of a doubly clamped beam made out of material with elastic modulus E. **(a)**. The beam, with dimensions $t \times w \times L$, has a cross-sectional area A, and a moment of inertia I with respect to the $\hat{z}$-axis. The beam is subject to a load $\vec{K}$, and tension $\vec{T}$. **(b)**. A segment of the beam, expanded on one side and contracted on the other. The line of neutral stress is indicated in dash.

The total force due to internal stress applied to a cross section of the beam F is equal to

$$\vec{F} = \int_A \sigma d\vec{A} \tag{A.5}$$

If $\vec{K}$ is the external force per unit length applied to the beam, the balance of forces requires that the sum of all forces acting on the segment of length dl is equal to the external force acting on that segment. If $\vec{F}$ is the total internal force on the lower base of the segment and $\vec{F} + d\vec{F}$ is the total internal force applied to the base, their difference $d\vec{F}$ should balance out the total external force applied to the segment $\vec{K}dl$. From this we can derive that

$$\frac{d\vec{F}}{dl} = -\vec{K} \tag{A.6}$$

The balance of torques requires that the difference in the internal torques $d\vec{M}$ acting on the top and bottom bases of the segment of the beam is equal to the torque created by the total force applied to the bases $\vec{F}$.

$$d\vec{M} + \vec{dl} \times \vec{F} = 0 \tag{A.7}$$

dividing everything by the length of the segment dl, and noticing that $d\vec{l}/dl = \vec{t}$ is the unitary tangential vector, leads to

$$\frac{d\vec{M}}{dl} = \vec{F} \times \vec{t} \tag{A.8}$$

For small bending, the radius of curvature is large and thus we can assume that the direction of $\vec{t}$ changes slowly, or in other words that $d\vec{t}/dl$ is small. If we differentiate Eq. A.8 along the length

$$\frac{d^2\vec{M}}{dl^2} = \frac{d\vec{F}}{dl} \times \vec{t} + \vec{F} \times \frac{d\vec{t}}{dl} \tag{A.9}$$

Using Eq. A.6 we get

$$\frac{d^2\vec{M}}{dl^2} = \vec{t} \times \vec{K} + \vec{F} \times \frac{d\vec{t}}{dl} \tag{A.10}$$

from the arguments above we know that the term $\frac{d\vec{t}}{dl}$ is small and we can neglect the second term in the equation except for the cases where the force $\vec{F}$ is large, or in other words for the beams under tension. If we set the force along the beam to tension

$$F_x = T \tag{A.11}$$

and use Eq. A.4, Eq. A.10 reduces to

$$\begin{aligned} EI_y \frac{d^4 z}{dx^4} - T\frac{d^2 z}{dx^2} - K_z = 0 \\ EI_z \frac{d^4 y}{dx^4} - T\frac{d^2 y}{dx^2} - K_y = 0 \end{aligned} \tag{A.12}$$

APPENDIX B

NANOTUBE IN THE SEM BEAM

A home built insert for a Keck LEO SEM system shown in Fig. B.3 allowed us to simultaneously image and perform electrical measurements on a CNT device. The sample were imaged at acceleration voltages of 1kV, which allowed a resolution of better than 10nm.

As can be seen in Fig. B.1, CNTs can be easily imaged in the SEM. The difference between a suspended and a non-suspended portion of tubes is clearly visible. The non-suspended portion appears "fuzzy", due to charging of the underlying silicon oxide, while the suspended portion appears as a sharp, thin line.

The purpose of this setup was to electrically actuate vibrations of doubly clamped CNT devices and to detect them by imaging. For one device, as shown in Fig. B.2, an image resembling a vibrating CNT was obtained. This result, however, could not be reproduced with further samples, and, as discussed below, imaging in a SEM beam proved to be very destructive to the sample both structurally and electrically.

Figure B.3 shows the structural damage that can be done to a CNT sample. On panels b and c we see a suspended CNT before and after intensive imaging. During imaging, the apparent diameter of the CNT has more than doubled due to carbon deposition in the SEM. On panels d and e we see another example of this effect. A series of three "dots" were deposited on the CNT by zooming in on the corresponding region. The second dot indicated by a line on panel d, was made by a 4min scan at 400× zoom. The third dot shown on panel e, was made in similar conditions.

Figure B.4 shown the changes in NT's conductance after imaging in the SEM.

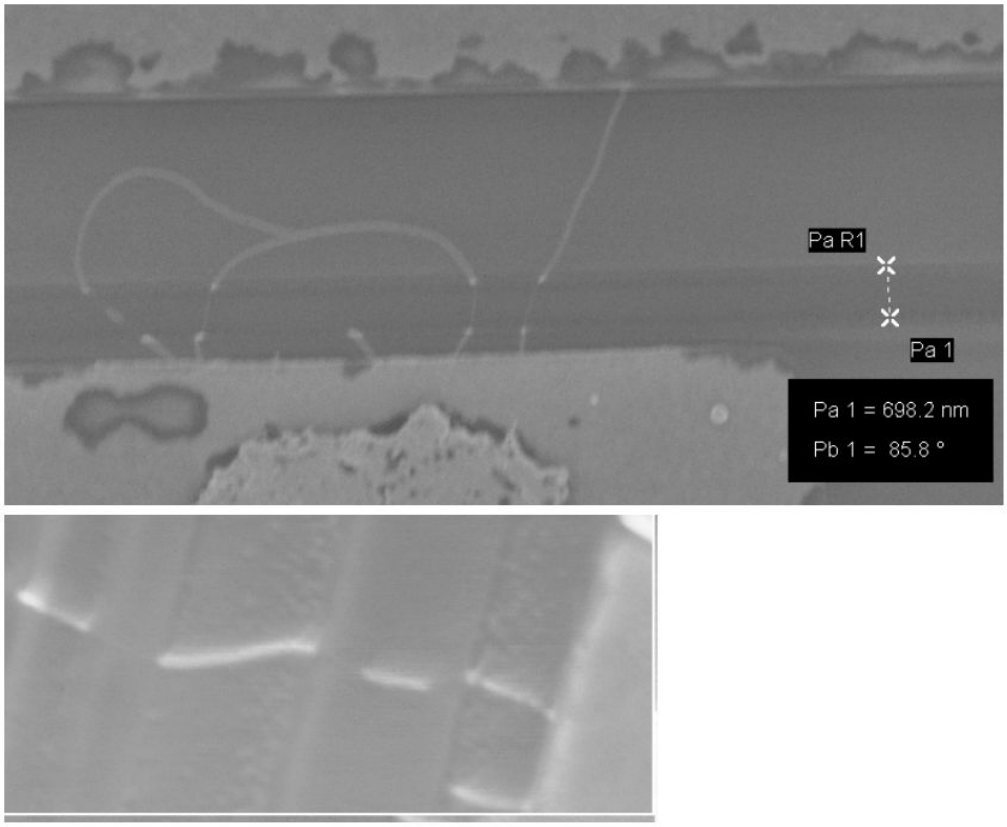

Figure B.1: Imaging CNTs in a SEM. The suspended portion of the CNT shows up as a thin, sharp line, while the portion on the oxide appears "fuzzy" due to charging.

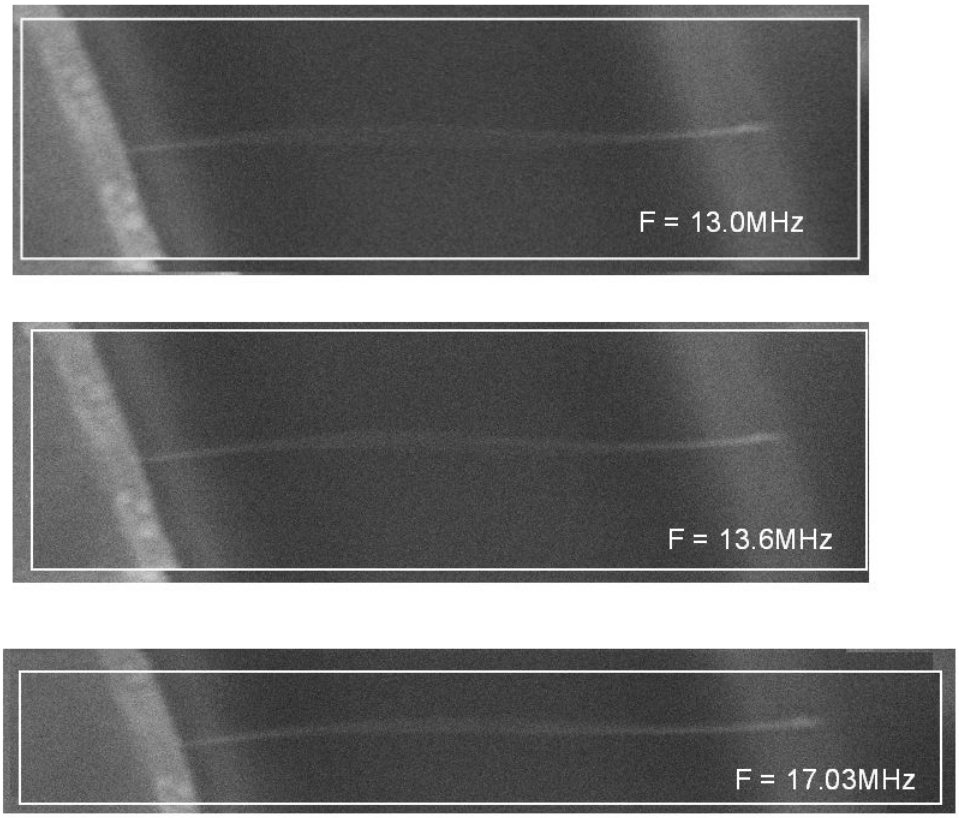

Figure B.2: NT resonance in a SEM. An SEM image of what may be a vibrating doubly-clamped CNT. The CNT is excited electrically through an AC voltage on the substrate.

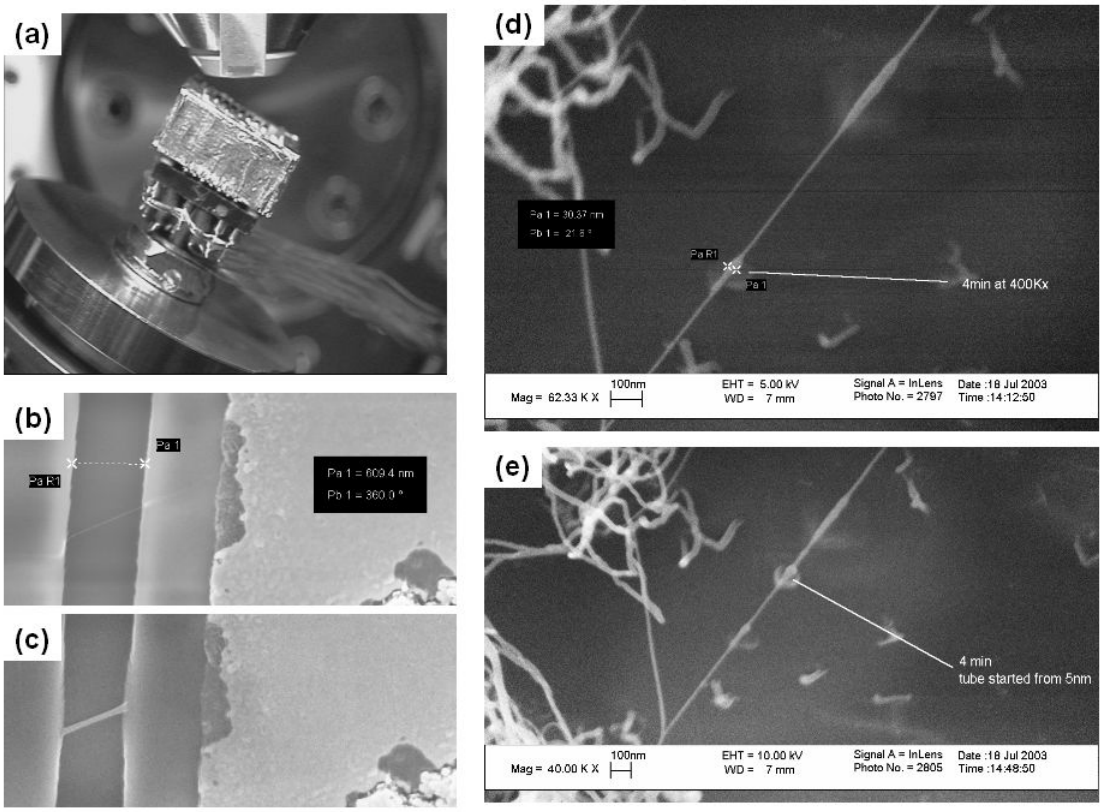

Figure B.3: Structural modifications in a SEM. **(a)** An image of the electrical measurement setup inside the SEM. **(b), (c)** A CNT device pre- and post- intensive imaging. The increase in the apparent CNT diameter is evident. **(d), (e)** A CNT device on which a series of "dots" were created by intensive imaging.

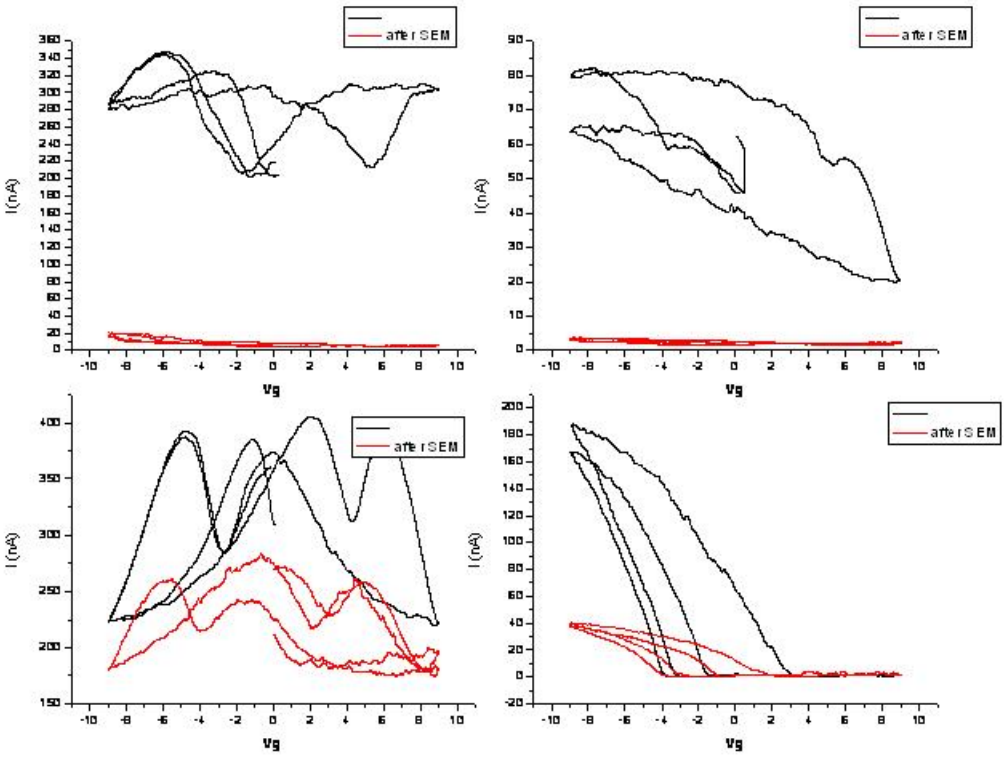

Figure B.4: Conductance modifications in a SEM. Current through CNT at a 10mV source-drain excitation vs. the DC gate voltage before and after imaging in an SEM, shown in black and red, respectively, for four different devices.

The conductance was measured by measuring a DC current through the CNT with a 10mV source-drain voltage. The graph shows the measured current as a function of the DC gate voltage; the current measured pre- and post-imaging is shown in black and red, respectively. For all of the devices the conductance decreases by as much as an order of magnitude.

Figure B.5 shows the behavior of the CNT's conductance while imaging. Again, the graph shows the current through the CNT at 10mV source-drain excitation as a function of the DC gate voltage. We observed three stages in the conductance behavior. First, the overall values of conductance decrease. Then the system develops n-type characteristics. Finally, each pass of the electron beam across the CNT registers as a spike on the measured current.

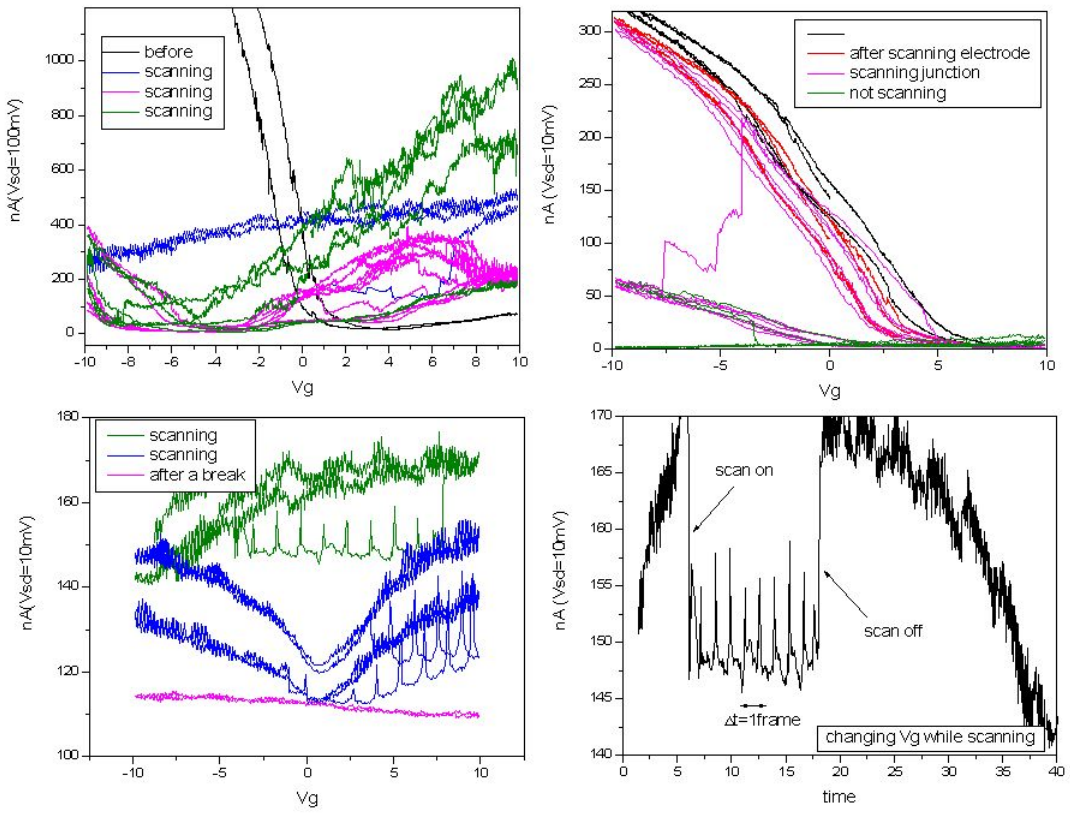

Figure B.5: Further conductance modifications in a SEM. As the CNT device is imaged, its conductance goes through three different stages of behavior, shown here for four different devices. First, the overall conductance decreases. Then n-type behavior develops. Last, the current through the CNT starts registering individual rasters of the electron beam.

APPENDIX C

MEASUREIT

C.1 Introduction

For the measurements of done in this thesis, a program capable of controlling a digital-to-analog computer card (DAC) and various instrumentats through a GPIB interface was needed. For this purpose, we wrote a custom program, "Measureit". The program was written using Labview 7.1 and should run on any computer system that has a NI digital-to-analog card with "DAQmx" driver support and/or a GPIB card.

The program bundle contains the following files:

1. default.cfg – the default configuration of the program
2. measureit2.2.llb – the program library
3. sources.dat – a list of supported GPIB instruments
4. manual.pdf – this document

We first describe the general capabilities of this program and then give some details of the implementation. Help is also available during the program execution. It can be accessed by pressing *Ctrl-H*

C.2 General capabilities and usage

The program is capable of three different types of measurement:

1. Setting all output channels to user-defined values, while reading-in values from all input channels.

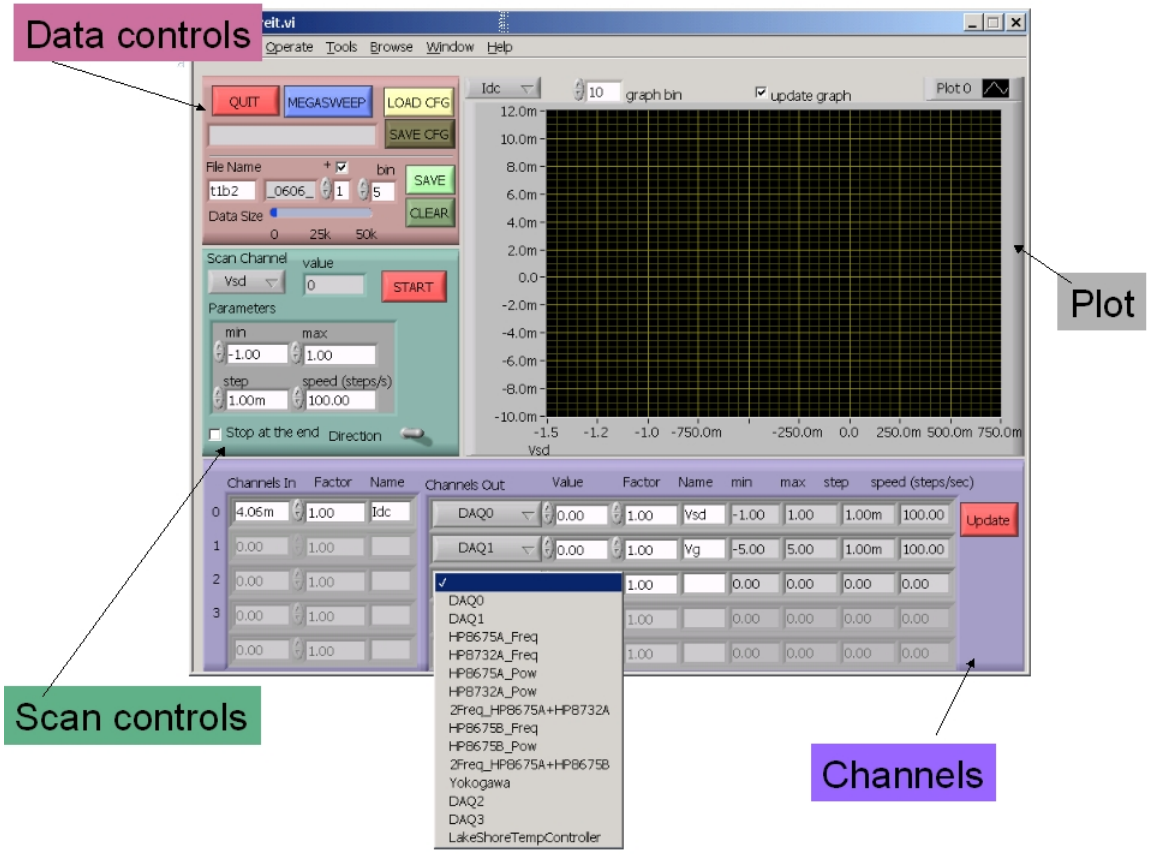

Figure C.1: Measureit program front panel

2. Recording input channels as a function of one output channel (sweep).

3. Recording input channels as a function of two or three output channels (megasweep).

The main window of the program is shown on Fig. C.1. It has four different panels: the data controls, the channels, the scan controls, and the plot. The data controls panel defines the program's configuration and data-saving parameters; the channels panel defines the input and output channels; the scan controls panel defines parameters for a single channel scan; the plot panel graphically shows the result of a single-channel scan. Before we describe the areas one by one, a word of caution: Currently no error catching is implemented in the program, thus the user must avoid canceling any started operations.

Channels

The channels panel allows the user to select and define the instruments he/she wants to control in a particular measurement.

For input, only the first four input channels of the DAC are supported. The user can only add the input channels sequentially: from 0 to 3. For each channel, the user can specify a factor that always multiplies the raw input value, and the channel name. The resulting value (raw value $\times$ *Factor*) is displayed and saved in the *Value* field (first column on the input channels panel). The input values are read in every 150 ms. The channel name is used for defining scans and graphs.

For output, both of the DAC output channels and a number of instruments controlled through the GPIB interface are supported. The list of all supported instruments can be seen in table C.1. In order to use the DAC channels, the user must ensure that the two DAC output channels are added in the NI channel control

software. They should be named *AO0* and *AO1*. If a second DAC is available, its output channels should be named *AO2* and *AO3*.

For each output channel, the user selects the controlled instrument, the value to set, the scaling factor (the value set on the instrument is *Value* × *Factor*), the channel name, the limits on the applied values, the default increment step, and the scanning speed (in steps per second). Even though the latter four fields are grayed out, they can be edited. The output channels are set to their respective values only when the *Update* button is pushed. If the value requested exceeds the limits, the limit value is set.

Scan controls

The scan controls panel defines the parameter of a single scan. The top drop-down menu, lets the user select, by name, the channel to scan of the defined output channels. The scan limits, increment, and scan speed, defined in the channels panel, are automatically copied to the *Parameters* cluster. The scan starts at the current value of that channel. The direction, and whether the scan stops at the limits, can be set by in the bottom of the panel by the *Direction* and *Stop at the end* controls. The scan starts after the *Start* button is pushed. Any of the scan parameters, including the direction, and the stop condition can be changed during the scan. The current value of the channel is displayed in the *Value* field. The recorded input and output channel values are stored in a buffer.

Plot

The plot panel displays the value of one of the input channels as a function of the scanned channel. User can select, by name, which input channel is displayed,

Table C.1: Instruments supported by measureit

N	Name	Description	Address	Command string
1	DAQ0	DAC out 0		
2	DAQ1	DAC out 1		
3	HP8675A_Freq	Frequency of the HP8675A	6	“FR” + value[MHz] + “MZ”
4	HP8732A_Freq	Frequency of the HP8732A	19	“FREQ” + value
5	HP8675A_Pow	Power of the HP8675A	6	“AP” + value[V] + “VL”
6	HP8732A_Pow	Power of the HP8732A	19	“POW” + vaue[dBm]
7	2Freq_HP8675A_HP8632A	Frequency of the HP8675A and the HP8732A together		
8	HP8675B_Freq	Frequency of the HP8675B	7	“FR” + value[MHz] + “MZ”
9	HP8675B_Pow	Pow of the HP8675B	7	“AP” + value[V] + “VL”
10	2Freq_HP8675A_HP8675B	Frequency of the HP8675A and the HP8675B together		
11	Yokogawa	Voltage source	5	“S” + value[V] + “E”
12	DAQ2	DAC out 0 on the second DAC board		
13	DAQ4	DAC out 1 on the second DAC board		
14	LakeShoreTempController	Temperature controller	12	“SETP 1,+” + value[K]

the graph bin size (whether every, or every second, or every third, etc. point is displayed), and whether the graph is to be updated.

Data controls

The upper portion of the data controls panel contains program configuration parameters. The *Quit* button quits the program, the *Megasweep* button opens the megascan panel, which we describe below, and the *Load CFG* and *Save CFG* buttons load and save the program configuration. The configuration consists of the defined channels, and which channel is currently selected to be scanned. The default configuration has one input channel and two output channels, as indicated in Fig. C.1.

The lower portion of the data controls panel defines how data is saved. The data is saved in ASCII column format, by stacking together values from all defined input and output channels. The scanned channel is in the first column, followed by the input channels, and followed by the other output channels. The file name for the data file has three parts: the name, the date, and the counter. The name is defined by the user in the *File Name* field, the date is inserted automatically in the "mmdd" format, and the counter is automatically incremented after each run. The incrementing option can be turned of, if desired. Pushing the *Save* button, saves the data and clears the buffer; pushing the *Clear* button, clears the buffer.

Megascan

The megascan panel is opened by pushing the *Megasweep* button on the data controls panel. This panel consists of three subpanels: the scan controls, the data controls, and the plot. These subpanels are very similar in their functions to the

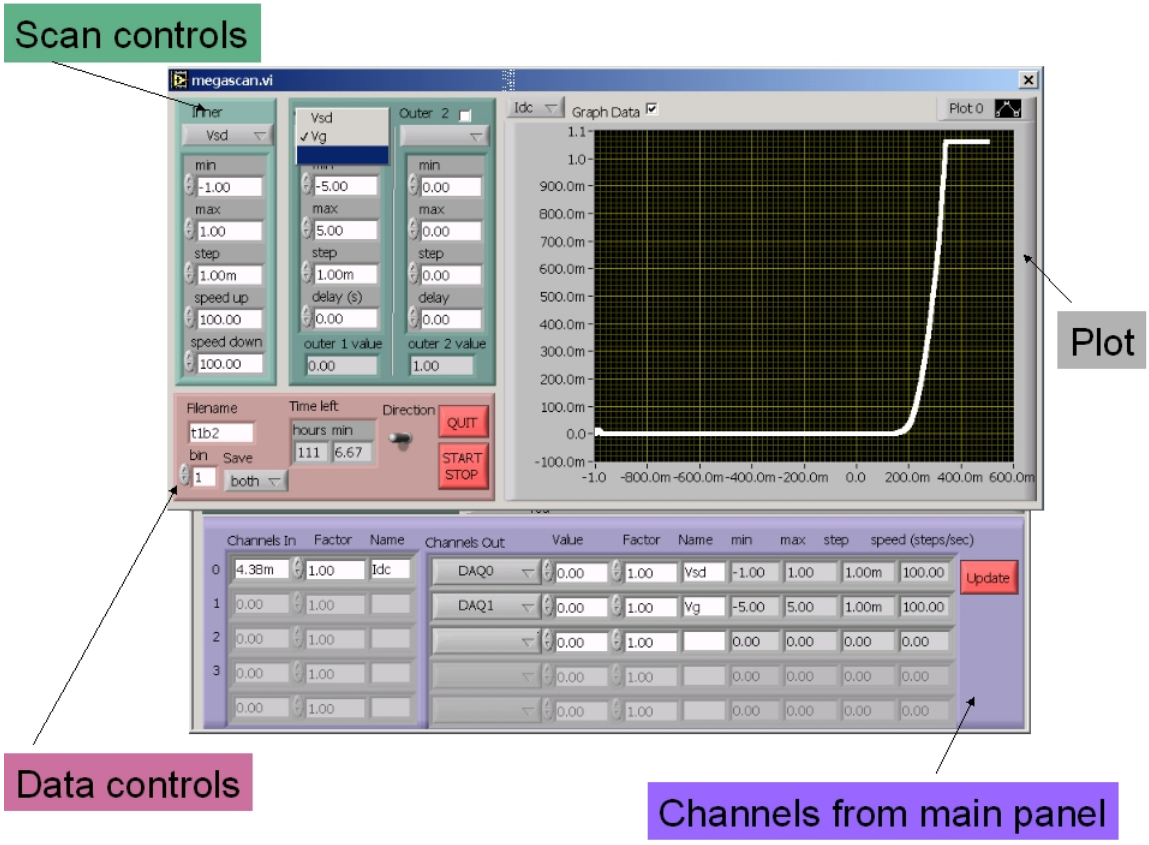

Figure C.2: Megasweep panel

panels described above.

The scan controls subpanel defines the megascan to be performed. The scan consists of one channel (the *inner* channel) being scanned up and down, while another channel (the *outer 1* channel) is incremented after each scan. Optionally, a third channel (*outer 2* channel) can be incremented at the end of each 2D megascan. The user selects, by name, the channels for the inner and outer loops, and modifies the scan parameters: limits, increment, and speed. For the inner channel the user must specify separately the up and down scan speeds, and for the outer channels the user may set a delay field, which defined the time the program waits (in seconds) after the increment of that channel. The scan parameters can not be changed during the scan. The current value for the outer 1 and outer 2 channels are displayed in the bottom of the subpannel.

The plot control displays graphically one of the input channels as a function of the inner channel value. The data is displayed only after the data was taken, i.e. when the outer channel is incremented. Optionally, the user may select not to graph the data.

The data controls subpanel defines how the data is saved and contains program controls buttons. The *Quit* button return to the main window, and the *Start/Stop* button starts or stops the scan. The bin field allows the user to define the binning the data, and the drop menu next to it allows the user to select whether the values from the up-scan, or both, up- and down-scans, are saved. At the beginning of the scan, the user is prompted for a filename. Again, as in the previous section, the filename consists of three parts: the name, the date, and the counter. The name is copied from the *File Name* field on the front window, the date is inserted automatically in the "mmdd" format, and the counter in this case is by default

"M1u", for the scan up, and "M1d" for the scan down, and is not automatically incremented. As the program overwrites any existing files with the same name, the filename must be edited or changed by the user at the filename prompt. Pressing the *Start/Stop* button when the scan is running stops the scan, as soon as the inner channel reaches the limit, not instantly. The data is saved to the file after each scan of the inner channel. Consequent scans are appended. The direction and the time left to completion are updated after each scan of the inner channel.

C.3 Internal coding

The following description of the code is very general and assumes knowledge of Labview.

Variables

The three most important variables in the program are: *Channels In* and *Channels Out* (arrays of clusters that contain information about the channels) and *Data* (a number array that contains the measured data).

VIs

The program's library contains 24 VIs; the top-level VI is "measureit.vi". A list of all other VIs is presented in table C.2, and the hierarchy of the VIs is shown in Fig. C.3. In this section we discuss three most important VIs.

`setChannel`

The `setChannel` VI takes the channel number, and value as inputs and outputs the error string. In the core of this VI is a case structure that, depending on

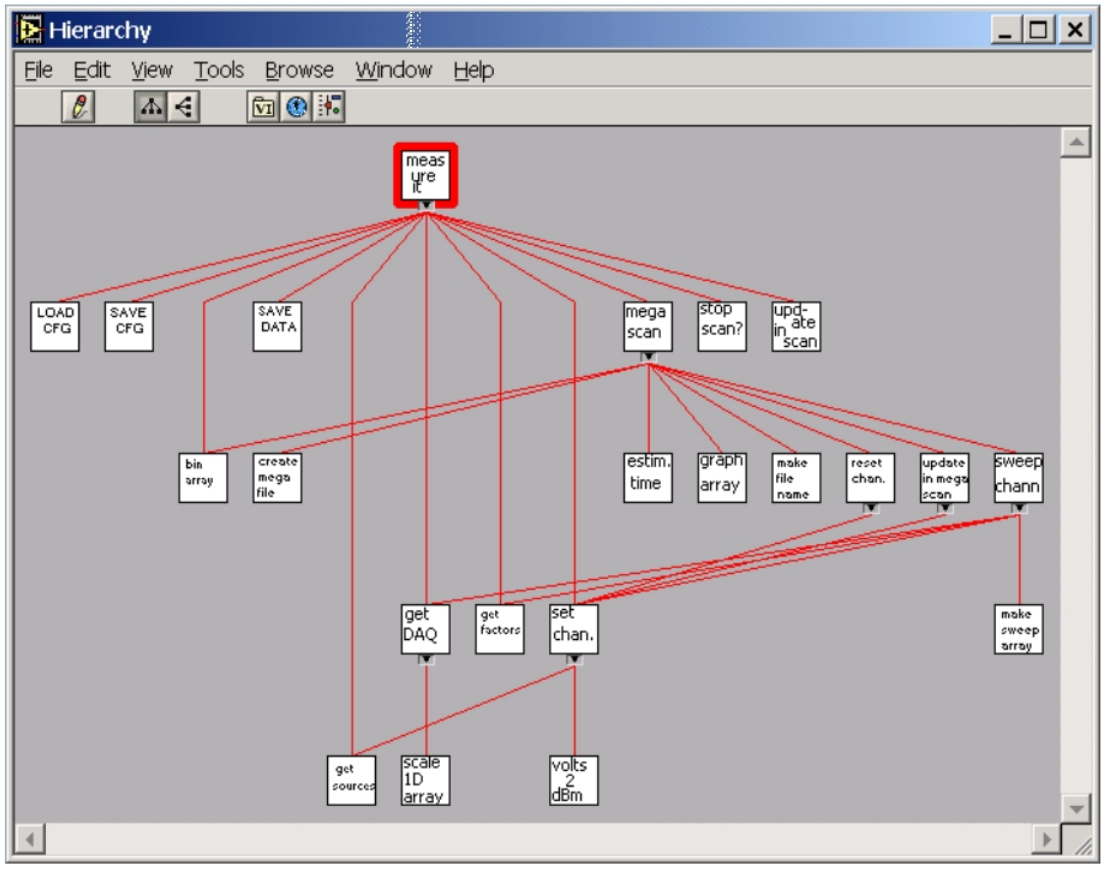

Figure C.3: Hierarchy of the VIs used in measureit

Table C.2: Measureit VIs listed in order of the appearance in the hierarchy. A brief description and input and output parameters are given.

Name	Function	Inputs	Outputs
measureit	Top-level program		
saveCFG	Saves the program configuration	*in-channels, out-channels*	
readCFG	Loads the program configuration	*CFG_filename* (optional)	*in-channels, out-channels*
saveData	Saves the data buffer to a file	*data, filename, date, counter, channel_number, in-channels_names, out-channels_names*	
megascan	Performs a 2D or 3D scan	*inner_number, in-channels, out-channels, filename, input-task*	*in-channels, out-channels*
stop_scan	Checks whether the single channel scan is over	*limits?, stop-at-the-end?*	*to_stop?*
update_in_scan	Updates where the scan has hit the limits	*at-the-end?, direction, out-channels*	
bin_array	Selects every n^{th} point out of an array	*array, bin (n), transpose?*	*array, array_size*
createMegaFile	Creates a file for a megascan and writes the header	*filename_up, filename_down, channel_number, in-channels_names, out_channels_names, down_file?*	*up_file, down_file*
estimate_time	Estimates the time left for a megascan	*inner_parameters, outer-1_parameters, outer-2_parameters, outer-1_value, outer-2_value*	*time-left*
graph_array	Produces a cluster of x and y values out of the data array	*array, x_position, y_position*	*graph-cluster*
makeFileName	Makes a filename for a megascan, given the user input part	*name*	*up_name, down_name*
reset_channel	Sets a desired channel to its limit depending on the sign of the step	*out-channels, channel_number*	*out_channels*
update_in_megascan	Updates the value a channels and checks for the limits	*out-channels, channel_number*	*scan_done?, out-channels, value*
sweepChannel	Sweeps a channel and read in the input values	*scan_parameters, read_input?, input_task*	*in-channels, data, error*
DAQ_getChannels	Reads the values from the DAC	*input_task, factors*	*data*
getFactors	Extracts the multiplying factors from the channels	*in-channels*	*factors*
setChannel	Sets an instrument to a certain output value	*channel_number, value*	*error*
makeSweepArray	Makes an array of values to assign a channel for a sweep	*scan_parameters*	*values*
getSources	Reads in the names of the available instruments from a file	*sources-file*	*sources-list*
scale_array1D	Multiplies a 1D array by factors in another 1D array ($a_i \times b_i$)	*array, factors*	*array*
voltsTodBm	Converts volts to dBm	*volts*	*dBm*

the *channel_number* (the sequence number of the instrument in the *sources.dat* file), either sets a particular DAC channel to the supplied *value*, or sends a GPIB request to set the instrument to that *value*. Some instrument dependent limits are hard-coded in the VI, and an error message is displayed if those limits are reached. Detailed description of the controlling DAC and GPIB channels is given later.

`measureit`

This is top-level program. On the most outer layer it consists of a two frame sequence. The first frame is initialization (Fig. C.4). During initialization, the DAC card input channels are started and and *input task* is created. The the channels are loaded from the default configuration file, using `readCFG`. The data buffer is initialized.

The second frame is the main program. It contains an infinite loop wired to the *Quit* button. The loop contains case structures for each of the buttons on the front panel (Fig. C.5) and the code for normal operation (Fig. C.6). The loop is executed every 150 ms, set by a timer. Every button is checked for being pressed, and if so, the corresponding case structure is executed. Also, as indicated in Fig. C.6, the input values are read-in, using `DAQ_getChannels`, and the scan parameters for the selected channel to scan are updated.

Figure C.5 shows some VIs wired to the their respective buttons. The *Load CFG*, *Save CFG*, *Megasweep* and *Save* buttons are wired to the `readCFG`, `saveCFG`, `megascan` and `saveData`, respectively. The *Clear* button is wired to the structure where the data buffer, *Data*, is set to zero. The *Update* button is wired to `setChannel`.

Finally, the *Start* button is wired to the case structure that executes a single

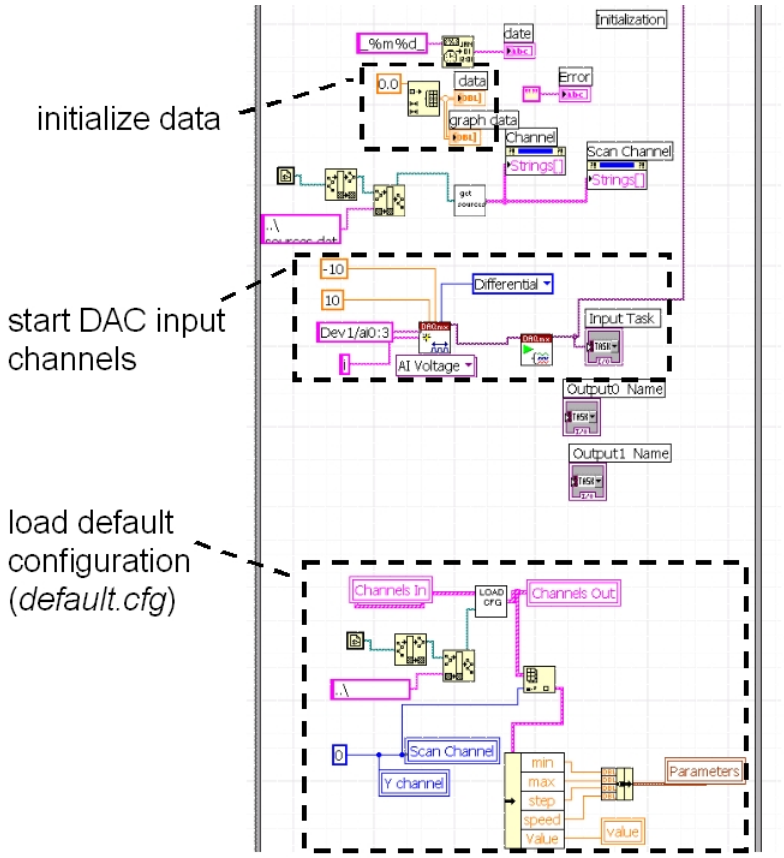

Figure C.4: Initialization part of measureit.

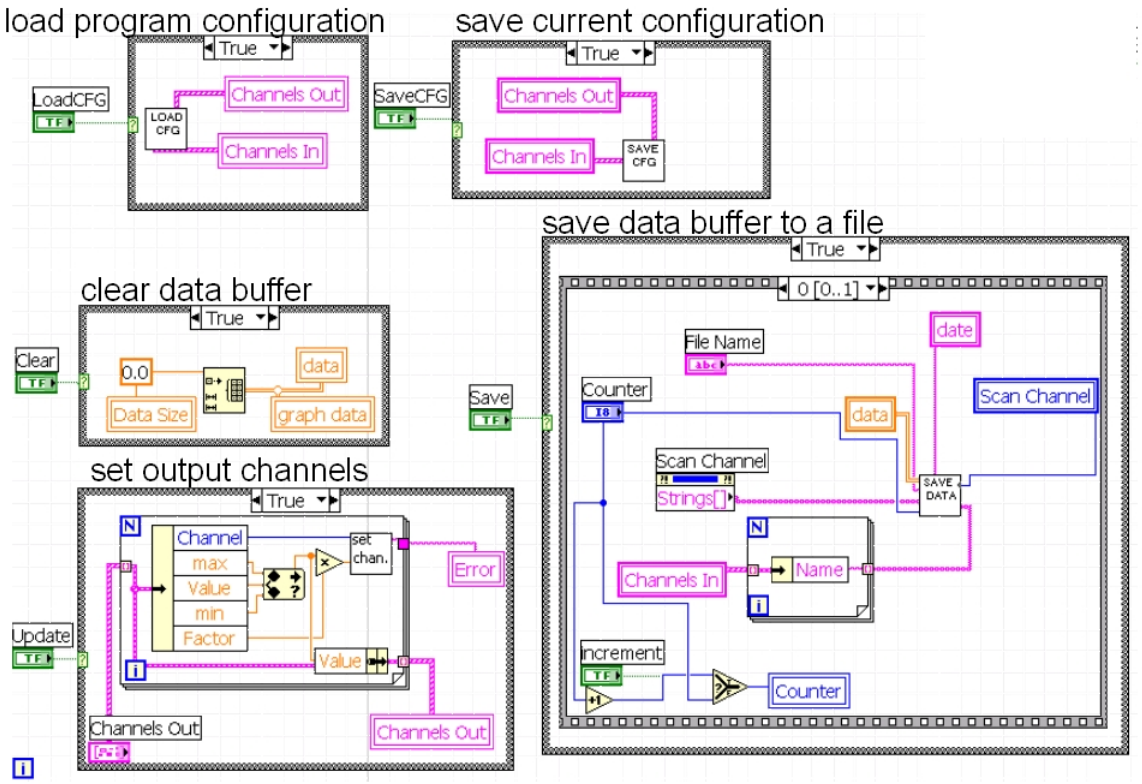

Figure C.5: An example of VIs wired to their respective buttons

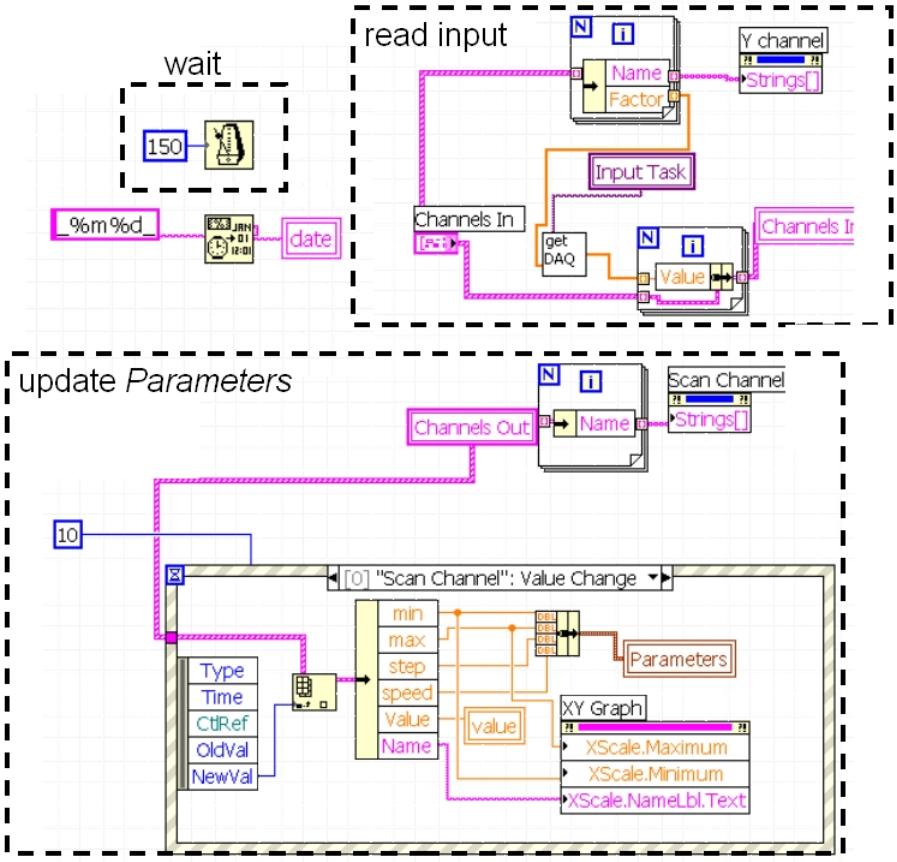

Figure C.6: Normal operation of measureit

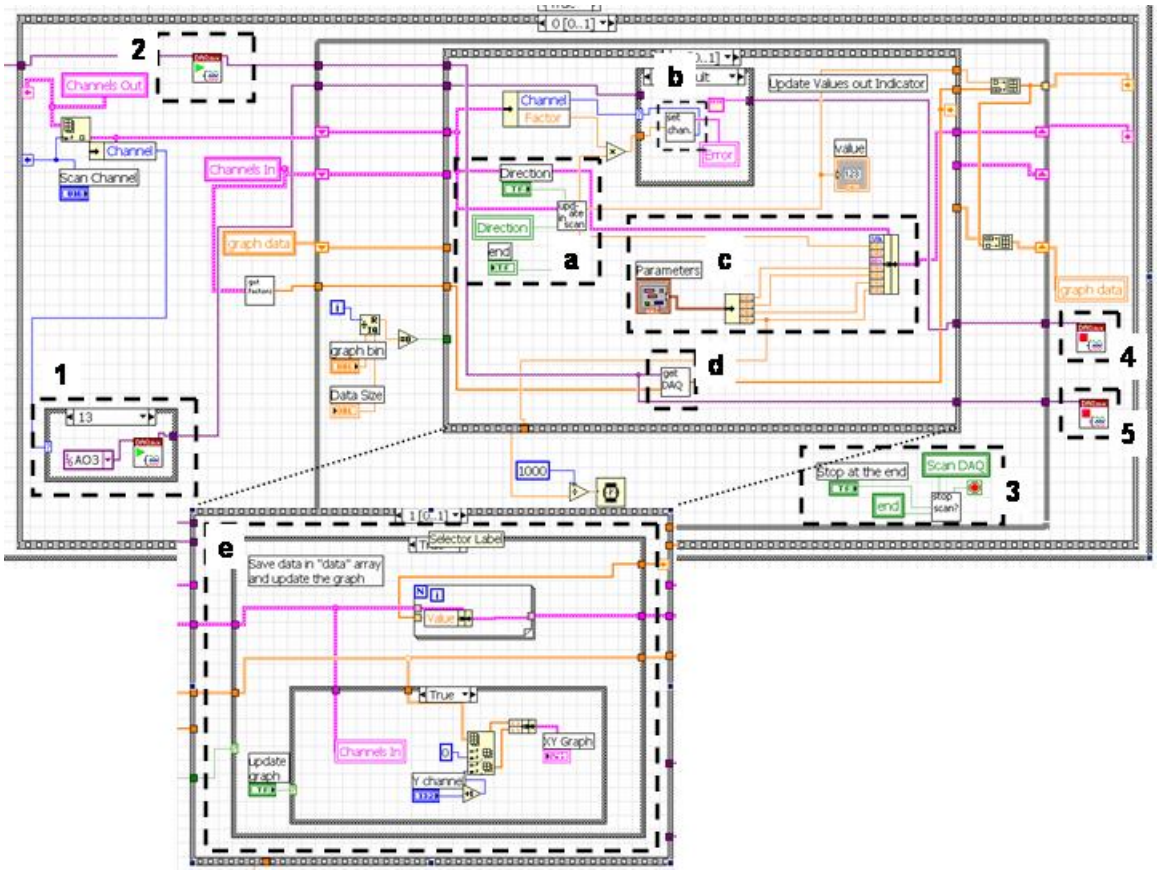

Figure C.7: The execution of the single channel scan subroutine.

channel scan. The scan consists of four parts. The first three parts are in the first frame of the structure, shown in Fig. C.7; the last part is in the second frame of the structure. Below is the pseudo-code for the scan. Each line is indicated in Fig. C.7 by its respective number.

1. Start the DAC output channels
2. Start the DAC input channels
3. While the scan is within limits (checked by the `stop_scan`)
   (a) Calculate the new value for the inner channel and update the direction of the scan (`update_in_scan`)
   (b) Update the inner channel (`setChannel`)
   (c) Read in the scan parameters
   (d) Read in the input values (`DAQ_getChannels`)
   (e) Appended to the *data* array and are graph the data
4. Stop DAC output channels
5. Stop DAC input channels
6. Append the output values are appended to the data array (not shown in Fig. C.7)

`megascan`

This VI is very similar to the operation of the scan structure in the front panel. The two main parts are: channel initialization, and the megascan. The megascan can be described with the following pseudocode:

1. Sweep *inner* channel to initial conditions (`sweepChannel`). If the down speed is set to 0, then set the *inner* channel (`reset_channel`)

2. Create two files to save data (`make_filename` and `createMegaFile`).

3. While the *Start/Stop* button is not pushed

   (a) While the *outer 1* channel is within limits

      i. Scan the *inner* channel up (`sweepChannel`)

      ii. Graph the results (`graph_array`).

      iii. Scan the *inner* channel down (`sweepChannel`)

      iv. Save *Data* to the up-scan, and down-scan files

      v. Increment *outer 1* channel 1

      vi. Check if the scan is at limits (`update_in_megascan`)

      vii. Update the time left for the scan (`estimate_time`)

   (b) If the scan is 3D and the 2D scan is over, update the *outer 2* channel and check if the scan is limits (`update_in_megascan` and `reset_channel`)

4. Save the values of the in-channels and out-channels

DAC channels

The code for setting and reading the DAC channels is shown in Fig. C.8. For DAC channels both operations have three parts: start, read /write, stop. Explicitly executing this three parts ensures faster operational speed, as otherwise, the channel is started and stopped at during each access attempt. These three parts are typically separated in the execution of the program. The channel is started during initialization, read or written to during the main execution cycle, and stopped

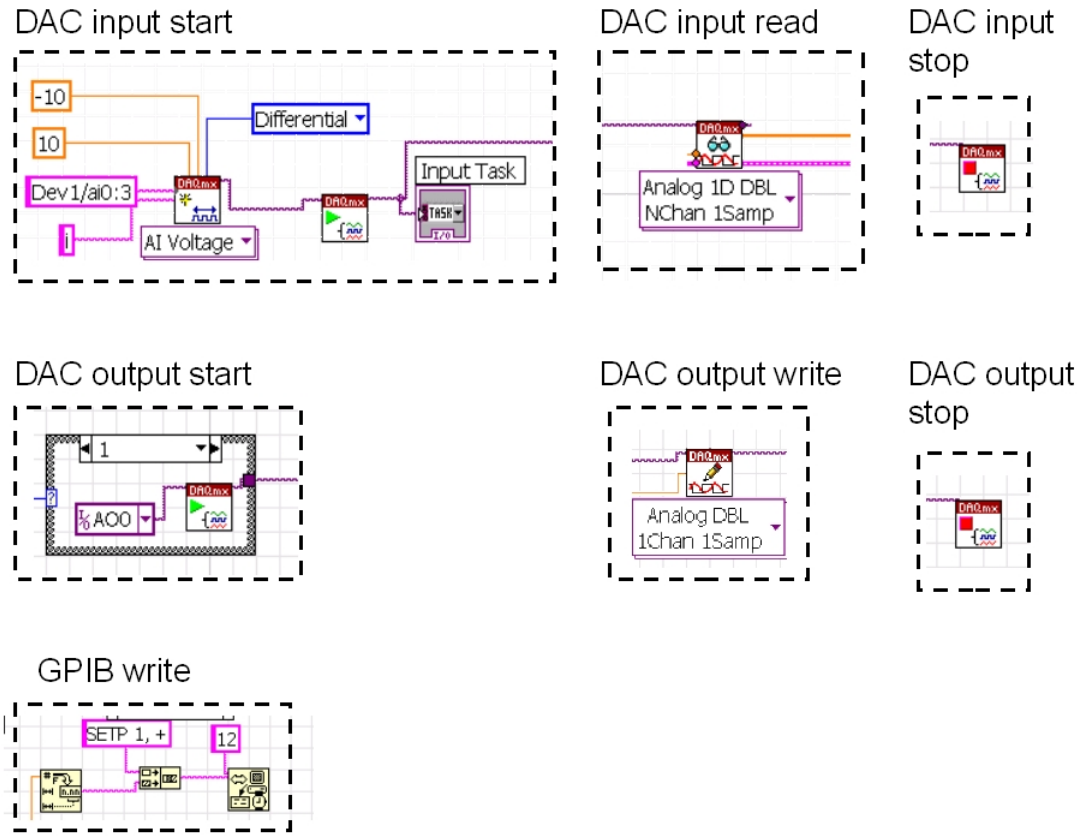

Figure C.8: Setting and reading DAC and GPIB channels

after all the data is collected. Channel starting can be done in two ways. The code for input channels in Fig. C.8 creates a new *input task* by accessing physical channels Dev1/ai0:3 with `DAQmx Create Channel`. Alternatively for output channels, the code references the already created global *output task AO0*. Both tasks are then started using `DAQmx Start Task`. The DAC channels are read with `DAQmx Read (Analog 1D DBL NChan 1Samp)` and set by `DAQmx Write (Analog DBL 1Chan 1Samp)`. The tasks are stopped using `DAQmx Stop Task`.

GPIB channels: Adding another instrument

The code for talking to the GPIB-interfaced instruments is sightly simpler. Sample code is shown in Fig. C.8. The value-to-set is transmitted using `GPIB Write`, which takes instrument specific command and GPIB address as inputs. The command is a string, whose format can by typically found in the instrument's manual. A typical command is: "FR 10MZ " (sets the frequency of HP8657B source to 10MHz).

New GPIB-controlled instruments can be added to measureit. Adding another instrument is done by modifying the *sources.dat* file and the `setChannel` VI. Below is the procedure:

1. Modify the sources.dat file
   (a) Open sources.dat in a text editor
   (b) Add a line with the instruments name and function at the end. For example: "HP8657B_Freq" for a HP 8657B high frequency source, frequency control channel. Do not delete the empty first line, and do not modify the existing instruments
   (c) Save the file as text

2. Modify the setChannel.vi file

   (a) Open `setChannel` VI in Labview

   (b) In the main case structure add a new case. The number of the case must match the sequential number of your instrument (the empty line counts as zero)

   (c) In the new empty case, make a comment with the name of your instrument

   (d) Copy the code from another case, for example case number 8 for the "HP8657B_Freq"

   (e) Modify the code. Keep in mind that the value is passed in absolute numbers, not scaled by a factor

      i. Change the bounds to appropriate values

      ii. Change the factor, if the instrument command takes scaled values

      iii. Change the GPIB command string according to the instrument's manual. For example for "HP8657B_Freq" the command string is "FR " + value [MHz] + "MZ "

      iv. Change the GPIB address

   (f) Save the VI

3. Run setChannel.vi and try to set some value

REFERENCES

Babic, B., Furer, J., Sahoo, S., Farhangfar, S., and Schonenberger, C. (2003). Intrinsic thermal vibrations of suspended doubly clamped single-wall carbon nanotubes. *Nano Letters*, 3(11):1577–1580.

Bargatin, I., Myers, E., Arlett, J., Gudlewski, B., and Roukes, M. (2005). Sensitive detection of nanomechanical motion using piezoresistive signal downmixing. *Applied Physics Letters*, 86:133109.

Beck, R., Eriksson, M. A., and Westervelt, R. (1998). *Applied Physics Letters*, 73:1149.

Bhiladvala, R. and Wang, Z. (2004). Effect of fluids on the q-factors and resonance frequency of oscillating beams. *Physical Review E*, 69:036307.

Bifano, T. G., Perreault, J., Mali, R. K., and Horenstein, M. N. (1999). *IEEE Journal of Selected Topics in Quantum Electronics*, 5:83.

Blom, F., Bouswtra, S., Elwenspoek, M., and Fluitman, J. (1992). *Journal of Vacuum Science and Technology B*, 10:19.

Braginsky, V., Mitrofanov, V., and Panov, V. (1985). *Systems with Small Dissipation*. The University of Chicago Press.

Broughton, J. Q., Meli, C. A., Vashishta, P., and Kalia, R. K. (1997). *Physical Review B*, 56:611.

Cao, J., Wang, D., and Dai, H. (2005). Suspended carbon nanotube quantum wires with two gates. *Nano Letters*, 1(1):138–141.

Carr, D. and Craighead, H. (1997). Fabrication of nanoelectromechanical systems in single crystal silicon using silicon on insulator substrates and electron beam lithography. *Journal of Vacuum Science and Technology B*, 15:2760.

Carr, D., Evoy, S., Sekaric, L., Craighead, H., and Papria, J. (1999). Measurement of mechanical resonance and losses in nanometer scale silicon wires. *Applied Physics Letters*, 75:920.

Carr, D., Evoy, S., Sekaric, L., Craighead, H., and Parpia, J. (2000). *Applied Physics Letters*, 77:1545.

Cho, A. (2003). Physics - researchers race to put the quantum into mechanics. *Science*, 299(5603):36–37.

Cleland, A., Aldridge, J., Driscoll, D., and Gossard, A. (2002). Nanomechanical displacement sensing using a quantum point contact. *Applied Physics Letters*, 81(9):1699–1701.

Cleland, A. and Roukes, M. (1996). *Applied Physics Letters*, 69:2653.

Cleland, A. and Roukes, M. (1999). *Sensors and Actuators*, 72:256–261.

Cleland, A. N., Pophristic, M., and Ferguson, I. (2001). Single-crystal aluminum nitride nanomechanical resonators. *Applied Physics Letters*, 79(13):2070–2072.

Cleland, A. N. and Roukes, M. L. (2002). Noise processes in nanomechanical resonators. *Journal of Applied Physics*, 92(5):2758–2769.

Craighead, H. G. (2000). Nanoelectromechanical systems. *Science*, 290:1532.

Cross, M. and Lifshitz, R. (2001). Elastic wave transmission at an abrupt junction in a thin plate with application to heat transport and vibrations in mesoscopic systems. *Physical Review B*, 64:085324.

Datta, S. (1995). *Electron Transport in Mesoscopic Systems*. Cambridge University Press.

Dresselhaus, M. S., Dresselhaus, G., and Avouris, P. (2001). *Carbon Nanotubes*. Springer.

Ekinci, K., Huang, X. M. H., and Roukes, M. (2004). Ultrasensitive nanoelectromechanical mass detection. *Applied Physics Letters*, 84:4469–4471.

Ekinci, K. and Roukes, M. (2005). Nanoelectromechanical systems. *Review of Scientific Instruments*, 76:061101–1, 061101–12.

Erbe, A., Krömmer, H., Kraus, A., and Blick, R. (2000). Mechanical mixing in noninear nanomechanical resonators. *Applied Physics Letters*, 77:3102.

Gao, R. P., Wang, Z. L., Bai, Z. G., de Heer, W. A., Dai, L. M., and Gao, M. (2000). Nanomechanics of individual carbon nanotubes from pyrolytically grown arrays. *Physical Review Letters*, 85(3):622–625.

Greywall, D. S., Yurke, B., Busch, P. A., Pargellis, A. N., and Willett, R. L. (1994). Evading amplifier noise in nonlinear oscillators. *Physical Review Letters*, 72(19):2992–2995.

Guo, T., Nikolaev, P., Rinzler, A., Tomanek, D., Colbert, D., and Smalley, R. (1995). *Journal of Physical Chemestry*, 99:694.

Hagen, J. B. (1996). *Radio-Frequency Electronics : Circuits and Applications*. Cambridge University Press.

Hernandez, E., Goze, C., Bernier, P., and Rubio, A. (1999). Elastic properties of c and bxcynz composite nanotubes. *Physical Review Letters*, 80:45024505.

Hertel, T., Walkup, R. E., and Avouris, P. (1998). Deformation of carbon nanotubes by surface van der waals forces. *Physical Review B*, 58(20):13870–13873.

Heyd, R., Charlier, A., and McRae, E. (1997). Uniaxial-stress effects on the electronic properties of carbon nanotubes. *Physical Review B*, 55(11):6820–6824.

Hone, J., Llaguno, M., Biercuk, M., Johnson, A., Batlogg, B., Benes, Z., and Fischer, J. (2002). Thermal properties of carbon nanotubes and nanotube-based materials. *Applied Physics A*, 74:339343.

Huang, S., Cai, X., and Liu, J. (2003a). Growth of millimeter-long and horizontally aligned single-walled carbon. *Journal of American Chemical Society*, 125:5636–5637.

Huang, X., Prakash, M., Zorman, C., Mehregany, M., and Roukes, M. L. (2003b). In *Tranducers '03 Proceedings 12th International conference on Solid State Sensors, Actuatos and Microsystems*, Boston, MA.

Huang, X. and Roukes, M. (2003). *Nature*, 421:6922.

Hutchinson, A. B., Truitt, P. A., Schwab, K. C., Sekaric, L., Parpia, J. M., Craighead, H. G., and Butler, J. E. (2004). Dissipation in nanocrystalline-diamond nanomechanical resonators. *Applied Physics Letters*, 84(6):972–974.

Ijima, S. (1991). Helical microtubules of graphitic carbon. *Nature*, 354:56.

Ilic, B., Krylov, S., Aubin, K., Reichenbach, R., and Craighead, H. G. (2005). Optical excitation of nanoelectromechanical oscillators. *Applied Physics Letters*, 86(19).

Ilic, B., Krylov, S., Senaratne, W., Ober, C., Neuzil, P., and Craighead, H. G. (2004). Attogram detection using nanoelectromechanical oscillators. *Journal Of Applied Physics*, 95:3694–3703.

Javey, A., Guo, J., Wang, Q., Lundstrom, M., and Dai, H. J. (2003). Ballistic carbon nanotube field-effect transistors. *Nature*, 424(6949):654–657.

Jenkins, N. E., DeFlores, L. P., Allen, J., Ng, T. N., Garner, S. R., Kuehn, S., Dawlaty, J. M., and Marohn, J. A. (2004). Batch fabrication and characterization of ultrasensitive cantilevers with submicron magnetic tips. *Journal of Vacuum Science and Technology B*, 22:909–915.

Jimbo, Y. and Itao, K. (1968). *Journal Horological Institute Japan*, 47:1.

Kane, C. L., Mele, E. J., Lee, R. S., Fischer, J. E., Petit, P., Dai, H., Thess, A., Smalley, R. E., Verschueren, A. R. M., J., T. S., and Dekker, C. (1998). Temperature-dependent resistivity of single-wall carbon nanotubes. *Europhysics Letters*, 41:683–688.

Kim, G. T., Gu, G., Waizmann, U., and Roth, S. (2002). Simple method to prepare individual suspended nanofibers. *Applied Physics Letters*, 80(10):1815–1817.

Kim, P., Shi, L., Majumdar, A., and McEuen, P. L. (2001). Thermal transport measurements of individual multiwalled nanotubes. *Physical Review Letters*, 8721(21).

Knobel, R. G. and Cleland, A. N. (2003). Nanometre-scale displacement sensing using a single electron transistor. *Nature*, 424(6946):291–293.

Kong, J., Soh, H. T., Cassell, A. M., Quate, C. F., and Dai, H. J. (1998). Synthesis of individual single-walled carbon nanotubes on patterned silicon wafers. *Nature*, 395(6705):878–881.

Kong, J., Yenilmez, E., Tombler, T. W., Kim, W., Dai, H. J., Laughlin, R. B., Liu, L., Jayanthi, C. S., and Wu, S. Y. (2001). Quantum interference and ballistic transmission in nanotube electron waveguides. *Physical Review Letters*, 8710(10):art. no.–106801.

Krishnan, A., Dujardin, E., Ebbesen, T. W., Yianilos, P. N., and Treacy, M. M. J. (1998). Young's modulus of single-walled nanotubes. *Physical Review B*, 58(20):14013–14019.

Kwon, Y., Berber, S., , and Tomanek, D. (2004). Thermal contraction of carbon fullerenes and nanotubes. *Physical Review Letters*, 92(1):015901.

LaHaye, M. D., Buu, O., Camarota, B., and Schwab, K. C. (2004). Approaching the quantum limit of a nanomechanical resonator. *Science*, 304:74–77.

Landau, L. (1982). *Fluid Mechanics*. Nauka.

Landau, L. and Lifschitz, E. (1987). *Theory of Elasticity*. Nauka.

Li, J. and Evoy, S. (2005). Study of laser-induced self-oscillations in silicon nanomechanical resonators. *Journal of Applied Physics*, 98:084316.

Liang, W. J., Bockrath, M., Bozovic, D., Hafner, J. H., Tinkham, M., and Park,

H. (2001). Fabry-perot interference in a nanotube electron waveguide. *Nature*, 411(6838):665–669.

Lifshitz, R. (2002). Phonon-mediated dissipation in micro- and nano-mechanical systems. *Physica B - Condensed Matter*, 316:397–399.

Lifshitz, R. and Roukes, M. L. (2000). Thermoelastic damping in micro- and nanomechanical systems. *Physical Review B*, 61(8):5600–5609.

Lu, J. (1997). Elastic properties of carbon nanotubes and nanoropes. *Physical Review Letters*, 79:12971300.

Marion, J. and Thornton, S. (1995). *Classical dynamics of particles and systems*. Harcourt Brace College.

Minot, E. (2004). *Tuning the band structure of carbon nanotubes*. Doctoral thesis, Cornell University.

Minot, E. D., Yaish, Y., Sazonova, V., and McEuen, P. L. (2004). Determination of electron orbital magnetic moments in carbon nanotubes. *Nature*, 428(6982):536–539.

Minot, E. D., Yaish, Y., Sazonova, V., Park, J. Y., Brink, M., and McEuen, P. L. (2003). Tuning carbon nanotube band gaps with strain. *Physical Review Letters*, 90(15):156401.

Mohanty, P., Harrington, D., Ekinci, K., Yang, Y., Murphy, M., and Roukes, M. (2002). Intrinsic dissipation in high-frequency micromechanical resonators. *Physical Review B*, 66:085416.

Mohanty, P., Harrington, D. A., and Roukes, M. L. (2000). Measurement of small forces in micron-sized resonators. *Physica B*, 284:2143–2144.

Nayfeh, A. H. and Mook, T. R. (1979). *Nonlinear Oscillations*. Wiley Interscience.

Nguyen, C. T. (1998). In *Proceedings of the 1998 IEEE Aerospace Conference*, volume 1, pages 445–460.

Nguyen, C. T. (1999). Micromechanical components for miniaturized low-power communications (invited pelnary). In *1999 IEEE MTT-S international Microwave Symposium FR MEMS Workshop*, pages 48–77, Anaheim, California.

Nguyen, C. T., Wong, A.-C., and Hao, D. (1999). Tunable, switchable, high-q vhf microelectromechanical bandpass filters. In *IEEE International Solid-State Circuits Conference*, volume 448, page 78, San Francisco, CA.

Nowick, A. and Berry, B. (1972). *Anelastic Relaxation in Crystalline Solids*. Academic Press.

Nygard, J. and Cobden, D. H. (2001). Quantum dots in suspended single-wall carbon nanotubes. *Applied Physics Letters*, 79(25):4216–4218.

Olkhovets, A., Evoy, S., Carr, D. W., Parpia, J. M., and Craighead, H. G. (2000). Actuation and internal friction of torsional nanomechanical silicon resonators. *Journal of Vacuum Science and Technology B*, 18(6):3549–3551.

Overney, G., Zhong, W., and Tomanek, D. (1993). Structural rigidity and low-frequency vibrational-modes of long carbon tubules. *Zeitschrift Physik D*, 27:9396.

Phillips, R. (2001). *Crystals, Defects and Microstructures*. Cambridge University.

Photiadis, D. and Judge, J. (2005). Attachment losses of high q oscillators. *Applied Physics Letters*, 85:482.

Poncharal, P., Wang, Z. L., Ugarte, D., and de Heer, W. A. (1999). Electrostatic deflections and electromechanical resonances of carbon nanotubes. *Science*, 283(5407):1513–1516.

Pop, E., Mann, D., Wang, Q., Goodson, K., and Dai, H. (2005). Thermal conductance of an individual single-wall carbon nanotube above room temperature. *Nano Letters*, 6(1):96–100.

Postma, H., Kozinsky, I., Husain, A., and Roukes, M. (2005). Dynamic range of nanotube- and nanowire-based electromechanical systems. *Applied Physics Letters*, 86:223105–1 – 223105–3.

Postma, H., Teepen, T., and Dekker, C. (2001). 1/f noise in carbon nanotubes. In *Electronic Correlations: from Meso- to Nanophysics*. DPSciences.

Purcell, S. T., Vincent, P., Journet, C., and Binh, V. T. (2002). Tuning of nanotube mechanical resonances by electric field pulling. *Physical Review Letters*, 89(27):276103.

Reulet, B., Kasumov, A. Y., Kociak, M., Deblock, R., Khodos, I. I., Gorbatov, Y. B., Volkov, V. T., Journet, C., and Bouchiat, H. (2000). Acoustoelectric effects in carbon nanotubes. *Physical Review Letters*, 85(13):2829–2832.

Rosenblatt, S. (2005). *Pushing the Limists of Carbon Nanotube Transistors*. Doctoral thesis, Cornell University.

Rosenblatt, S., Lin, H., Sazonova, V., Tiwari, S., and McEuen, P. (2005). Mixing

at 50 ghz using a single-walled carbon nanotube transistor. *Applied Physics Letters*, 87:153111.

Rosenblatt, S., Yaish, Y., Park, J., Gore, J., Sazonova, V., and McEuen, P. L. (2002). High performance electrolyte gated carbon nanotube transistors. *Nano Letters*, 2(8):869–872.

Roszhart, T. (1990). In *Proceedings of the Solid-State Sensor and Actuator Workshop*, page 13, Hilton Head Island, SC.

Roukes, M. (2000). Nanoelectromechanical systems. *Technical Digest of the 2000 Solid-State Sensor and Actuator Workshop*.

Roukes, M. (2001). Plenty of room indeed. *Scientific American*, 285(3):48–57.

Rugar, D., Budakian, R., Mamin, H. J., and Chui, B. W. (2004). Single spin detection by magnetic resonance force microscopy. *Nature*, 430(6997):329–332.

Salvetat, J. P., Briggs, G. A. D., Bonard, J. M., Bacsa, R. R., Kulik, A. J., Stockli, T., Burnham, N. A., and Forro, L. (1999). Elastic and shear moduli of single-walled carbon nanotube ropes. *Physical Review Letters*, 82(5):944–947.

Sapmaz, S., Blanter, Y. M., Gurevich, L., and van der Zant, H. S. J. (2003). Carbon nanotubes as nanoelectromechanical systems. *Physical Review B*, 67(23):235414.

Sazonova, V., Yaish, Y., Üstünel, H., Roundy, D., Thomás, A., and McEuen, P. L. (2004). A tunable carbon nanotube electromechanical oscillator. *Nature*, 431:284–287.

Schoelkopf, R., Wahlgren, P., Kozhevnikov, A., Delsing, P., and Prober, D. (1998).

The radio-frequency single-electron transistor (rf-set):a fast and ultrasensitive electrometer. *Science*, 280:1238.

Schwab, K. (2002). Spring constant and damping constant tuning of nanomechanical resonators using a single-electron transistor. *Applied Physics Letters*, 80:1276.

Sekaric, L., Carr, D. W., Evoy, S., Parpia, J. M., and Craighead, H. G. (2002). Nanomechanical resonant structures in silicon nitride: fabrication, operation and dissipation issues. *Sensors and Actuators A - Physical*, 101(1-2):215–219.

Shabana, A. A. (1997). *Vibration of Discrete and Continuous Systems*. Springer.

Sidles, J. A., Garbini, J. L., Bruland, K. J., Rugar, D., Zuger, O., Hoen, S., and Yannoni, C. S. (1995). Magnetic-resonance force microscopy. *Reviews of Modern Physics*, 67(1):249–265.

Stipe, B. C., Mamin, H. J., Stowe, T. D., Kenny, T. W., and Rugar, D. (2001). Magnetic dissipation and fluctuations in individual nanomagnets measured by ultrasensitive cantilever magnetometry. *Physical Review Letters*, 86(13):2874–2877.

Stowe, T. D., Yasumura, K., Kenny, T. W., Botkin, D., Wago, K., and Rugar, D. (1997). Attonewton force detection using ultrathin silicon cantilevers. *Applied Physics Letters*, 71(2):288–290.

Tans, S. J., Verschueren, A. R. M., and Dekker, C. (1998). Room-temperature transistor based on a single carbon nanotube. *Nature*, 393(6680):49–52.

Treacy, M. M. J., Ebbesen, T. W., and Gibson, J. M. (1996). Exceptionally high young's modulus observed for individual carbon nanotubes. *Nature*, 381(6584):678–680.

Turner, K. L., Miller, S. A., Hartwell, P. G., MacDonald, N. C., Strogatz, S. H., and Adams, S. G. (1998). Five parametric resonances in a microelectromechanical system. *Nature*, 396(6707):149–152.

Üstünel, H., Roundy, D., and Arias, T. A. (2005). Modeling a suspended nanotube oscillator. *Nano Letters*, 5(3):523–526.

Wagner, J. W. (1990). *Physical Acoust.*, 19:201.

Walters, D. A., Ericson, L. M., Casavant, M. J., Liu, J., Colbert, D. T., Smith, K. A., and Smalley, R. E. (1999). Elastic strain of freely suspended single-wall carbon nanotube ropes. *Applied Physics Letters*, 74(25):3803–3805.

Wang, Y., Henry, J. A., Sengupta, D., and Hines, M. A. (2004). *Applied Physics Letters*, 85:5736.

White, J. B. E. and Pohl, R. O. (1995). In *Materials Research Society Symposium Proceedings*, volume 356, page 567.

Williams, P., Patel, A. M., Falvo, M. R., Washburn, S., Superfine, R., and Papadakis, S. J. (2003). Fabrication of nanometer-scale mechanical devices incorporating individual multiwalled carbon nanotubes as torsional springs. *Applied Physics Letters*, 82:805.

Wong, E. W., Sheehan, P. E., and Lieber, C. M. (1997). Nanobeam mechanics: Elasticity, strength, and toughness of nanorods and nanotubes. *Science*, 277(5334):1971–1975.

Woodside, M. (2001). *Scanned Probe Microscopy of the Electronic Properties of Low-Dimensional Systems*. Doctoral thesis, University of California at Berkeley.

Yaish, Y., Park, J. Y., Rosenblatt, S., Sazonova, V., Brink, M., and McEuen, P. L. (2004). Electrical nanoprobing of semiconducting carbon nanotubes using an atomic force microscope. *Physical Review Letters*, 92(4):046401.

Yakobson, B., Brabec, C., and Bernholc, J. (1996). Nanomechanics of carbon tubes: Instabilities beyond linear response. *Physical Review Letters*, 76:25112514.

Yakobson, B. I. (1997). In *Fullerenes – Recent Advances in the Chemistry and Physics of Fullerenes and Related Materials*, volume 5, pages 549–560. Electrochemical Society.

Yang, J., Ono, T., and Esashi, M. (2000). Surface effects and high quality factors in ultrathin single-crystal silicon cantilevers. *Applied Physics Letters*, 77(23):3860–3862.

Yang, J., Ono, T., and Esashi, M. (2001). *Journal of Vacuum Science and Technology B*, 19:551.

Yang, L., Anantram, M. P., Han, J., and Lu, J. P. (1999). Band-gap change of carbon nanotubes: Effect of small uniaxial and torsional strain. *Physical Review B*, 60(19):13874–13878.

Yao, N. and Lordi, V. (1999). Youngs modulus of single-walled carbon nanotubes. *Journal of Applied Physics*, 84:19391943.

Yasumura, K. Y., Stowe, T. D., Chow, E. M., Pfafman, T., Kenny, T. W., Stipe,

B. C., and Rugar, D. (2000). Quality factors in micron- and submicron-thick cantilevers. *Journal of Microelectromechanical Systems*, 9(1):117–125.

Yu, M. F., Files, B. S., Arepalli, S., and Ruoff, R. S. (2000). Tensile loading of ropes of single wall carbon nanotubes and their mechanical properties. *Physical Review Letters*, 84(24):5552–5555.

Yurke, B., Greywall, D. S., Pargellis, A. N., and Busch, P. A. (1995). Theory of amplifier-noise evasion in an oscillator employing a nonlinear resonator. *Physical Review A*, 51(5):4211–4229.

Zalalutdinov, M., Aubin, K. L., Reichenbach, R. B., Zehnder, A. T., Houston, B., Parpia, J. M., and Craighead, H. G. (2003). Shell-type micromechanical actuator and resonator. *Applied Physics Letters*, 83(18):3815–3817.

Zener, C. (1948). *Elasticity and Anelasticity of Metals*. The University of Chicago Press.

Zhou, C. W., Kong, J., and Dai, H. J. (2000). Intrinsic electrical properties of individual single-walled carbon nanotubes with small band gaps. *Physical Review Letters*, 84(24):5604–5607.

Zhou, X., Park, J., Huang, S., Liu, J., and McEuen, P. (2005). Band structure, phonon scattering, and the performance limit of single-walled carbon nanotube transistors. *Physics Review Letters*, 95:146805.